STRUCTURAL IDENTIFICATION, DAMAGE DETECTION BY NON-DESTRUCTIVE TESTS AND DETERMINING AXIAL LOADS IN CABLES

A THESIS SUBMITTED TO
THE GRADUATE SCHOOL OF NATURAL AND APPLIED SCIENCES
OF
MIDDLE EAST TECHNICAL UNIVERSITY

BY

MUSTAFA CAN YÜCEL

IN PARTIAL FULFILLMENT OF THE REQUIREMENTS
FOR
THE DEGREE OF MASTER OF SCIENCE
IN
CIVIL ENGINEERING

DECEMBER 2009

Approval of the thesis:

STRUCTURAL IDENTIFICATION, DAMAGE DETECTION BY NON-DESTRUCTIVE TESTS AND DETERMINING AXIAL LOADS IN CABLES

submitted by **MUSTAFA CAN YÜCEL** in partial fulfillment of the requirements for the degree of **Master of Science in Civil Engineering Department, Middle East Technical University** by,

Prof. Dr. Canan Özgen
Dean, Graduate School of **Natural and Applied Sciences** _____

Prof. Dr. Güney Özcebe
Head of Department, **Civil Engineering** _____

Assoc. Prof. Dr Ahmet Türer
Supervisor, **Civil Engineering Department** _____

Examining Committee Members:

Prof. Dr. Çetin Yılmaz
Civil Engineering Dept., METU _____

Prof.Dr.Murat Dicleli
Engineering Sciences Dept., METU _____

Assoc. Prof. Dr. Oğuzhan Hasançebi
Civil Engineering Dept., METU _____

Asst. Prof. Dr. Alp Caner
Civil Engineering Dept., METU _____

Assoc. Prof. Dr. Ahmet Türer
Civil Engineering Dept., METU _____

Date: _____

I hereby declare that all information in this document has been obtained and presented in accordance with academic rules and ethical conduct. I also declare that, as required by these rules and conduct, I have fully cited and referenced all material and results that are not original to this work.

Name, Last Name: MUSTAFA CAN YÜCEL

Signature :

ABSTRACT

STRUCTURAL IDENTIFICATION, DAMAGE DETECTION BY NON-DESTRUCTIVE TESTS AND DETERMINING AXIAL LOADS IN CABLES

Yücel, Mustafa Can
M.S., Department of Civil Engineering
Supervisor : Assoc. Prof. Dr Ahmet Türer

December 2009, 94 pages

Damage and condition identification of existing structures using non-destructive tests is a common challenge that has been worked on for a long time. In this study, two different methods were developed to find existing force on cables as well as determine bending characteristics (EI coefficients) of beam like structures (such as bridges). Comparing forces in symmetrically placed cables or against values obtained from design drawings would indicate structural imbalance as well as finding EI coefficients at a number of segments on a bridge girder might indicate weak regions that might possibly have undergone structural damage, having weak connections, lost composite action etc. With the help of the proposed algorithm, the stiffness parameters of bridges can be assessed and the location of any damage that is in the magnitude which can affect displacement behavior of system can be located. The developed methods are demonstrated using the values analytically obtained from the created models and the effectiveness of the algorithm is criticized. Furthermore, several damage scenarios on a scaled lab beam was used to test the application using real experimental data; including tests on undamaged beam (for identification) and tests on the damaged beam. Additional experiments were conducted on a cable stretched in the laboratory instrumented using a load cell to measure instantaneous axial load on the cable and compare these values against the values obtained

from the developed tension measurement device. The results are compared and conclusions are derived.

Keywords: Structural identification, non-destructive damage identification, cable axial force, static load test, structural damage localization

ÖZ

TAHRİBATSIZ TESTLERLE YAPI TANIMLAMASI, HASAR TESPİTİ VE KABLO GERGİ KUVVETİNİN ÖLÇÜLMESİ

Yücel, Mustafa Can
Yüksek Lisans, İnşaat Mühendisliği Bölümü
Tez Yöneticisi : Doç. Dr. Ahmet Türer

Aralık 2009, 94 sayfa

İnşa edilmiş yapıların hasarsız testlerle durum ve hasar tespiti üzerinde uzun süreler çalışılmış yaygın bir konudur. Bu çalışmada, kabloların taşıdığı kuvveti bulmak ve kiriş tipi yapıların (örneğin köprüler) bükülme karakteristiklerini (EI katsayısı) belirlemek için iki farklı metod geliştirilmiştir. Kabloda bulunan yükün simetrik kablolardaki yüklerle ya da tasarım hesabıyla karşılaştırılmasının yapısal dengesizlikleri orta çıkarabileceği gibi, bir köprüde çeşitli sayıda parça için EI hesaplanması da yapısal hasar, zayıf bağlantı, kompozit etki kaybı gibi nedenlerle oluşan zayıflıkları ortaya çıkarabilir. Önerilen algoritmanın yardımı ile, köprülerin rijitlik parametreleri bulunabilir ve sistemin deplasman davranışını etkileyen düzeydeki hasarların yeri tespit edilebilir. Geliştirilen metodlar yapılan modellerden analitik olarak elde edilen değerlerle gösterilmiş ve algoritmanın etkililiği ölçülmüştür. Ek olarak, ölçekli bir laboratuar kirişinde çeşitli hasar planları kullanılarak metod hasarsız (yapısal tespit için) ve hasarlı kirişten elde edilen gerçek deneysel veri ile test edilmiştir. Ayrıca laboratuarda gerilen yük hücresine sahip bir kablo üzerinde anlık eksenel yük ölçümleri yapılmış ve elde edilen değerler geliştirilen gergi ölçme aletinden elde edilen sonuçlar ile karşılaştırılmıştır. Sonuçlar birbirleri ile karşılaştırılmış ve neticeler belirtilmiştir.

Anahtar Kelimeler: Yapısal tespit, yapısal hasar tespiti, kablo eksenel kuvveti, durağan yük testi, yapısal hasar yer tespiti

To my family

ACKNOWLEDGMENTS

This study was conducted under the control of the Assoc. Prof. Ahmet Türer. I would like to express my sincere thanks and appreciations for his support, guidance, encouragement and criticisms during this study. It was a great honor and pleasure to work with him.

I also would like to extend my thanks to my parents and my friends for their encouragement and assistance throughout this study.

A part of this study is done under “Determining Axial Loads in Cables of Cable-Stayed Bridges” project, financed by Scientific Researches Project Council; with project number 200-03-03-03.

The scholarship provided by The Scientific & Technological Research Council of Turkey (TÜBİTAK) during my graduate study is highly acknowledged.

TABLE OF CONTENTS

LIST OF TABLES

TABLES

LIST OF FIGURES

FIGURES

Nomenclature

$\bar{y}$	centroidal distance
$\sum A$	total area
$\sum M$	summation of moment
E	bridge input voltage
e_0	bridge output voltage
f_c	compressive strength of concrete
f_y	yield strength of steel
g	gravitational acceleration
h	cable displacement amount
I_{total}	total moment of inertia
k	support bearing width extensions (45 degrees)
K_s	gage factor
L	Length of instrument
L	total unrestrained length of cable
M_x	moment at point x
N	support bearing width
n	mode number involved
P	Force in the instrument
Q	moment of area
q	shear flow in cross-section
r	beam web-flange connection radius
T	Axial force in cable
t_f	beam flange width
t_w	beam web width
V	shear force
w	weight of cable per length

f_n frequency of mode number n

Greek Symbols

α Cable deformation angle

ϵ_0 strain to be measured

ϵ_c strain in concrete

ϵ_s strain in steel

Ψ_{cqr} modal vector of associated mode

σ_a steel allowable stress

σ_c stress in concrete

σ_s stress in steel

τ shear stress

CHAPTER 1

INTRODUCTION

1.1 Introduction

In today's world, the trend of identifying and monitoring structures (buildings, bridges, dams, infrastructural facilities...etc) receive an increasing attention, especially from the developed countries where the investments turn their tide from building new structures to preserving them. Particularly in the commercial and military (dominantly aviation branch) community, structural health monitoring (SHM) is used to reduce pre-determined manual inspections with condition based maintenance for more effective designs and more precise component restoring and replacement decisions. This shift in the methodology results in noteworthy savings in the overall cost of ownership as well as in operational safety. As all civil engineering structures age with time and usage, their components become more susceptible to damage and failure. Extreme events may also cause damage and can lead to collapse. Since these types of damage cannot be predicted from design parameters, special techniques are required to quantify and localize them. Among all evaluation methods, non-destructive practices are one of the most common and advantageous techniques due to the fact that they are reliable, robust and leave almost no trace behind when the identification is completed. There are a number of procedures on this field each having strong and weak points, several of which will be discussed in later sections of this context. One of the aims of this study is to propose a stable, non-destructive technique which will be affected minimally from environmental effects and noise for quantifying and localizing the damage successfully by using easily measurable structural parameters.

The cable stayed bridges are commonly built for pedestrian and vehicle uses and it is necessary to make the tension forces in the cables equal to the analysis results obtained during the design stage to control the alignment. There are few methods to measure the internal force of an assembled cable; temporary use of load cells is not possible because it is impossible to unload the cable and attach a load cell. This study also focused on another structural identification case; determining the axial load in an existing bridge cable. One alternative is using the relationship between the tension in a string and the dynamic vibration frequency, which can be demonstrated by using a guitar string. If a wire is stretched, its vibration frequency increases. However, this technique necessitates the use of advanced technological equipment (like sensitive accelerometers) and a rather complex post-processing of the data obtained using Fourier transform, in addition to the accurate information on cable weight and length. In order to overcome these difficulties, it is planned to devise an instrument that is both easy to use and requires minimum calculations; in other words, a quick way to determine the tension with minimal use of resources available at the site.

1.2 Previous Studies

1.2.1 Previous Studies on Non-Destructive Damage Identification

Many different methods and procedures are proposed so far, and these methods evolved thanks to the advancements in the computational and measurement technologies. The increase in measurement resolution and speed combined with the tremendous jump in the capacity of number of calculations per unit time allowed engineers to utilize more sophisticated schemes, therefore to obtain more effective results, in terms of both accuracy and time consumption.

The flexibility matrix, a matrix that relates deflections of a system to the resistance of that system to deformation, is one of the key parameters that can be traced for proving the existence of damage and localizing it [1]. However, constructing full static flexibility matrix is problematical and not feasible; therefore it is suggested to create a 'proportional flexibility matrix' (PFM) that can be generated from only output data. This matrix is constructed as multiplication of a scalar with the real flexibility matrix, and this scalar is proved to be the first modal mass. Then this PFM is integrated to an existing method known as damage locating vectors (DLVs), to increase its robustness and accuracy. The proposed method is tested

with two examples, 7 degrees of freedom spring-mass system and a planar truss of 14 bays. It is found out that unless there is a significant mass change; damages are successfully identified and pinpointed by the DLV method integrated with PFM by using only output data.

The flexibility matrix of a system is also used by other researches for the aim of determining and locating damage [2]. In this study, it is claimed that damage can be identified by minimizing the Frobenius norm of the difference between the experimental and analytical flexibility matrix (from a finite element model) only related to the measured degrees of freedom of the system in concern. This approach results in a non-linear optimization problem with constraints that is numerically solved through a Newton-like method. The continuum damage model and partial experimental modal parameters are bases for the damage detection and the process is performed on a number of different examples. The real life problems like digital sampling shortcomings, truncation of modal spectrum, noise corruption are also considered during the study. It is claimed that the method is very effective for the presented situations, yet it can be seen that the accuracy of the proposed technique highly depends on the finite element model from which the flexibility is obtained. The authors argue that they coped with this problem by implementing a two stage model updating, where first stage deals with updating of the undamaged structure and second stage is composed of damage identification contemplating only noise measurements as uncertainties.

Though a powerful tool, the use of flexibility matrix can be enhanced by combining it with the stiffness matrix [3]. The authors point out that using solely flexibility for damage localization is heuristic, limited in application and may necessitate post-processing. It is proposed that the most obvious advantage of combining flexibility with stiffness is; first one is easy to construct from outputs and the second one is far better in locating the damage thanks to the correlation between degrees of freedom and diagonal stiffness elements. One drawback is, when the input data is unknown (i.e. output only measurement is used), it is impossible to obtain the mode shape vectors as mass-normalized. The authors suggest forming an approximate mass matrix as a correction procedure, or alternatively corrections on changes in the mentioned stiffness and flexibility matrix presuming the subsistence of undamaged sections. Yet the most important downside is, as authors stated, stipulation of well-distributed sensors, in addition to the probability of the damage masked by the numerical errors, if the damage is diminutive.

The neural networks, mathematical formulations that simulate the formation of human nerve cells, are also used in detecting the damage [4]. The change of variance (or covariance) is selected as damage index for damage identification of beams using artificial neural networks based on statistical dynamic properties. For SDOF systems, the variances of displacement, velocity and acceleration are considered. From these three, displacement is more sensitive and it is selected as damage index for SDOF systems. For MDOF systems, it can be found that the selected damage index, the variance of displacement, is not only a function of the stiffness, but also the modal shapes, which means the index is sensitive to both the change of stiffness and the location of the change. For the ANN part, back propagation (BP) is used. For verification, a three span continuous bridge is used. After verification, it has been found out that the ratio of correct predictions in each scenario is in the range of 80% - 88%, which is not very satisfactory as the author agreed. In real life applications, it suggested to use the proposed method as gross technique, and then apply to methods with more finesse.

It is also an alternative approach to create new parameters as damage indices [5]. In this paper, a technique based on frequencies and modal shapes, which are expected to change after structural damage, are applied to sense damage in reinforced concrete beams. In the identification, first few frequencies and modal shapes, which are obtained by experimental modal analysis, are used. Also, a new detection method is proposed based on the 'local modal stiffness', a parameter related with the strain energy of the mode shapes under unit excitation. This can be determined from frequency response functions and is a function of both frequency and modal shape. Comparison of point local modal stiffness from two data sets implies a direct comparison between two response levels since the value of this parameter does not depend on the normalization of the modes. Furthermore, the point local modal stiffness is dependent not only on the mode shapes but also on the frequencies, and, therefore, it appears to be more sensitive for detecting changes than when only mode shapes are used. A numerical verification is accomplished for the proposed method. After the numerical verification, an experimental study is performed. It is claimed that the method successfully determines and locates the damage both in numerical simulations and experiments.

There are also methods suggested involving more physical approaches [6]. The proposed methods in the study are based on the dynamic response of flawed or cracked reinforced concrete structures subjected to impact loading and on analyzing the ability of the resistivity measurement to detect and to locate cracks and spalling with in situ measurements on a

damaged concrete slab. According to the proposed method, an impact loading generating small stress levels is applied on the free surface. The normal-to-surface displacement or velocity time history is monitored by transducers located on the free surface itself at different locations. Typically, the dynamic response of flawed or cracked concrete structures subjected to impact loading is governed by stress wave propagation. The second method describes prospective works on the resistivity measurement for on-site concrete damage characterization, in the frame of the non-destructive evaluation methods. Electrical resistivity resents an interesting ability to characterize concrete damage and more particularly its cracks. For the validation through experiments and FEM, when shallow defects are considered, a fairly good agreement between experimental and numerical results, as well as theoretical predictions in terms of natural frequencies of flexural vibration is obtained.

The theoretical energy parameters that can be calculated via dynamic input data are also valuable assets in damage identification [7]. In this paper, a damage detection strategy based on acceleration responses' energy is proposed based on the relationship between the frequency response function (FRF) of acceleration responses and mode shapes. In order to erect a damage detection technique for real-world application with wide use of accelerometers and avoid a complex mode shape solution, a damage detection strategy based on acceleration responses' energy is suggested in this paper, based on the relationship between the frequency response function (FRF) of acceleration responses and mode shapes. However, the excitation force is never measured in detail in applications; therefore this term is replaced by the power spectral density (PSD) function of acceleration. From the results point of view, authors state that this strategy can assess the damage comparatively as degree, like 'slight', 'moderate', or 'severe', with excellent anti-noise pollution ability.

Statistics also offer several powerful tools for damage identification [8]. The authors state that it is possible to detect damage with location only by statistical analysis on output-only measurements of structures. It is stated that the method requires neither identifying modal parameters nor constructing a finite element model. The basic assumption of this approach is that there is a significant increase in the residual errors when a Kalman model identified from the undamaged system. In the method suggested, collected data from monitored structure is used to construct the Hankel matrices. If there is no structural damage existing, the orthonormality assumption between these subspaces of the Hankel matrices obtained from different data sets remains approximately valid according to small residues, which may be

used as damage indicators. The orthonormality change between subspaces if responses due to noise effects and/or structural damages, if any. The suggested damage indicators are the complementary angle between subspaces in question, norm of the matrix that expresses the loss of orthonormality, and a transformed matrix calculated from the residue matrix. The authors concluded that due to its simplicity, this method is appropriate for on-line applications.

Similar to the developments in computation techniques, the advancements in sensor technology lead to different methods [9]. One of the recent measuring devices, the Fiber Bragg grating sensors are used to reveal the presence of damage in a structure. The important point is the system mentioned is able to interrogate a wide range of frequencies to detect changes in modal properties (frequencies in this case) which is predicted as the existence of damage. One advantage of Fiber Bragg grating sensors is, since they are long and extend in longitudinal direction, accurate calculations of modal shapes are possible. As the verification example shows, these sensors can retrieve modal shapes well up to the frequency of 1.5 kHz. Yet one important point worth mentioning is, the presence of a second damage, localized further from sensor position was not able to be observed as frequency shift. Even if this is the case, the study illustrates the possibility of employing these optical devices for structural damage identification purposes.

Another powerful tool given to the command of engineers is the technological advancements in computers and thus ability to perform too complex calculations in an acceptable duration. It is suggested that the traditional method of identifying changes in natural frequencies and mode shapes of systems with respect to their original conditions is susceptible to external effects and noise pollution, therefore analyzing the damaged mode shapes via wavelet transform imparts enhanced and more robust tactic [10].The mathematical background and the theory behind this suggestion are verified by a set of experiments, whose results indicate that a wavelet analysis technique on the mode or static deflected shape of a system is able to pinpoint the damage, both for existence and location. In addition, the weak point of wavelet analysis is mentioned as noise; as moderate amounts of noise can render this technique useless. However, a complementary method is proposed to overcome this vulnerability; the kurtosis-based damage calibration. The use of the latter one in conjunction with the wavelet analysis is said to form a practical and effective method considering the measurement noise.

1.2.2 Previous Studies on Determining Axial Force in an Existing Bridge Cable

It is usually not feasible (and meaningful) to disassemble installed cables, therefore there is a continuing research for determining the tension in a cable from the parameters that can be measured by simple tests without disturbing the structure. The identified natural frequencies, the bending stiffness and the boundary conditions can be used as inputs for this purpose [11]. . In this study, the real boundary conditions of a cable is assumed to vary between a hinge supported string and a beam with clamped boundary conditions, in addition to the bending stiffness of the cable (denoted as EI). The authors correlate the idealized frequency and the dimensionless bending coefficient of the cable to the measurements by Gauss-Newton minimization algorithm. Then, it is possible to determine the cable force from the idealized frequency. From analytical simulations, it can be concluded that the accuracy of the method is high, calculated values are in the 1% neighborhood of the exact values obtained from measurements. As a field study, this technique is applied to the Danube Channel Bridge which was built in 1972. As the results, authors claim that the boundary conditions and cable stiffness though play a role in the cable force; it can indeed be neglected without causing too much errors. It is also added that the dynamic measurements and computational technologies have a very high potential in the solution of structural identification necessities.

There are other suggested ways of including the cable sag and bending stiffness in calculations, such as using the frequency differences at high vibration frequencies [12]. In the study mentioned, the effect of cable sag on the fundamental and higher frequencies is studied in detail and it is concluded that effect of the sag becomes ineffective quickly in the modes higher than mode number three. And then effect of the bending stiffness is considered. In order to accomplish this, the cable is treated as a beam with initial axial tension T and flexural stiffness EI. The boundaries are accepted to lie in between fully pin and clamped, and the effect of the bending stiffness is assumed to depend on the ratio of existing tension to the EI. If this ratio is small (i.e. EI value is high compared to the tension in the chord), the bending stiffness has considerable influence on cable's higher order frequencies. Moreover, the effect of bending stiffness increases quadratically as the mode number n increases, if the cable is simply supported at both ends. With the increase in the ratio, however, the influence of flexural rigidity wanes quickly. In addition to these studies, authors suggested a relation between the frequencies of the pre-tensioned cable and the tension in it. In essence, it is similar to

the chord equation that relates frequency of the cable (in a mode) to the force, but there is a significant difference. In the paper referred, defining the frequency difference of the adjacent frequencies is based on the solution of the non-linear (or transcendental) cable equations that account for the effects of cable sag and bending stiffness. The proposed technique is tested first in laboratory tests on pre-tensioned stay cables and the results reported have errors in the range of 1.4% to 3.3%. After these successful experiments in a controlled environment, ambient vibration measurements on stay cables of Qingzhou Bridge are processed and the forces in all 168 cables are calculated. Yet one drawback in the method, which is also confirmed by the authors, is that any error in estimation of the frequency will result in approximately twice as much error in calculation of forces.

There are other researches in the literature that tried to uncover the effect of sag and bending stiffness of the cable by analytical means [13]. From the comparisons, however, in the paper it is stated that the effect of the sag in the out-of-plane frequencies is negligible in both short and long cables for the sag over diameter ratios commonly used in the market. For adjusting the axial force and the bending stiffness simultaneously, the authors used a least squares minimization of an error function they created. Also, the rotational stiffness of the cable ends is discussed and two separate cases are treated; cables without intermediate supports and cables with intermediate supports. Then sensitivity analysis are performed for the influence of different assumptions introduced in the process of determining the axial force. These analysis are on the effects of rotational stiffness at the ends, shear flexibility and rotational inertia, and the transverse stiffness of the intermediate supports. Yet, the results are not discussed openly in the paper mentioned.

In spite of the researches on the effects of sag and stiffness, the vibrating chord theory is still used in processing bridge test results [14]. In this study, the dynamic tests performed on the Vasco da Gama Bridge are explained. The noteworthy part is the non-conventional testing system used, comprehending several independent accelerographs conveniently synchronized by a central computer, as well as a laser interferometric system for non-contact dynamic measurements in stay cables. The bridge is monitored intensely due to the high proneness of the long span bridge to aerodynamic instability problems and the high seismic risk of the southern part of Portugal. The cable forces are computed by applying vibrating chord theory to the data taken, stating that this method is “relatively simpler” and “less expensive”.

CHAPTER 2

DETERMINING AXIAL FORCE IN EXISTING BRIDGE CABLES

2.1 Introduction

During the design stage, the axial loads in the cables of a short-span cable stayed bridge are calculated from the analytical models and the overall design checks are carried according to this calculated force. However, once the bridge is built, the tension in the cables should be adjusted to the analysis results. In addition, the forces in existing cables change due to the time-dependent material properties and variations in environment conditions. In order to calibrate the existing structure cables, a method that is both fast and easy to practice is required.

In this chapter, two methods of different types for determining the axial force in existing bridge cables are discussed; first a dynamic method based on the relationship between the free vibration frequency of a string and axial force in it, and second a static method based on the relation between the force existing in a cable and the force required to pull it perpendicular to its longitudinal axis. In the first part of this chapter, the theory behind the principle, and the necessary equipment are introduced, then an example study conducted is explained. In the second part, the instrument devised for the static method is detailed, its sensor calibration experiments are described and a laboratory case study is given.

2.2 Dynamic Method

The method is called dynamic due to the fact that the vibration properties of a cable is used in determination of the force it carries. The method has solid mathematical foundation and gives accurate results short of installing a load cell on the cable; but the load cell solution is most of the times impossible due to the fact that it necessitates dismantling the system before instrumentation and after completing all the works. However, the dynamic method has several shortcomings; first of all, it requires special electronic devices (accelerometers, data acquisition systems and computers). Secondly, processing the test data requires mathematical knowledge and time.

2.2.1 Theory

It is a known fact that more tense (i.e. having more tensile load inside) strings produce higher sound than loose strings. This effect is the result of the fact that frequency of a string is related with the axial load in it. The other parameters involved are mass of the wire per length and total unrestrained length (i.e. the length of the wire segment that vibrates freely). For an idealized system where the effect of bending is neglected, axial load in a cable is related to the n^{th} vibrating frequency of it with Equation 2.1:

$$T = \frac{4w\,(f_n L)^2}{n^2 g} \tag{2.1}$$

The assumptions of this approach are, first of all, the system behaves linear in both material and geometric-wise. Secondly, the flexural stiffness of the cable is totally neglected; bending of the cable is left out of scope. In order to make compatible measurements with this assumption, however, the modes excited during testing should be lower modes, where bending of the string is limited than higher modes. As the mode considered gets higher, mode shape includes more bending, which causes the results to deviate from true value, because of the second assumption.

2.2.2 Application

The vibrating frequency of a wire can be determined via an accelerometer; by recording the acceleration response of the string to an impulsive load (and allowing free vibration).

Special attention should be paid that the accelerometer should not move relative to the tendon (it should be fixed well) and an impulse exciting the first mode should be applied; in the shape of a bow in horizontal plane (Figure 2.1). The latter is because vertical movement will be affected by the own weight of the cable. Exciting the first mode is crucial because higher modes involve bending of the wire along the length that causes the flexibility (or stiffness) of the tendon to affect the result, which is not anticipated. Then applying Fourier Transform to

Figure 2.1: Accelerometer Attached to Cable (in Field Study)

this acceleration data will yield a set from which the vibrating frequencies of the cable can be predicted. This is done by determining the peaks in the FFT (Fast Fourier Transform – an efficient algorithm to compute the discrete Fourier Transform and its inverse) data. Calculations can be done in MATLAB environment which initializes Cooley – Tukey FFT algorithm in which a discrete Fourier Transform of any composite size is broken into smaller sized pieces and then processed. The resultant peak values are modal frequencies. With these parameters and Equation 2.1, the axial load in the cable is measured.

As a field study, several of the pedestrian bridges built on the road to the Esenboğa Airport (the Protocol Road) are tested. The bridges are cable stayed type with a tall angled pylon at one side; 10 cables that carry deck are connected to the pylon at one face (5 each at two sides), and 16 cables that balance it are connected to the other face (8 each at two sides). All the cable forces are determined; though there was no way to verify the results.

2.3 Static Methods

2.3.1 Theory

In order to measure the axial load in an existing bridge cable without the need of dynamic data, an instrument is designed. The working principles of the instrument are based on the fact that the force required to pull the cable perpendicular to its axis is related with the axial force in it (Figure 2.2). In Figure 2.2 the the bold lines show the first shape of the cable and the upper dashed lines are the shape of cable in further pulled condition. The movement amount

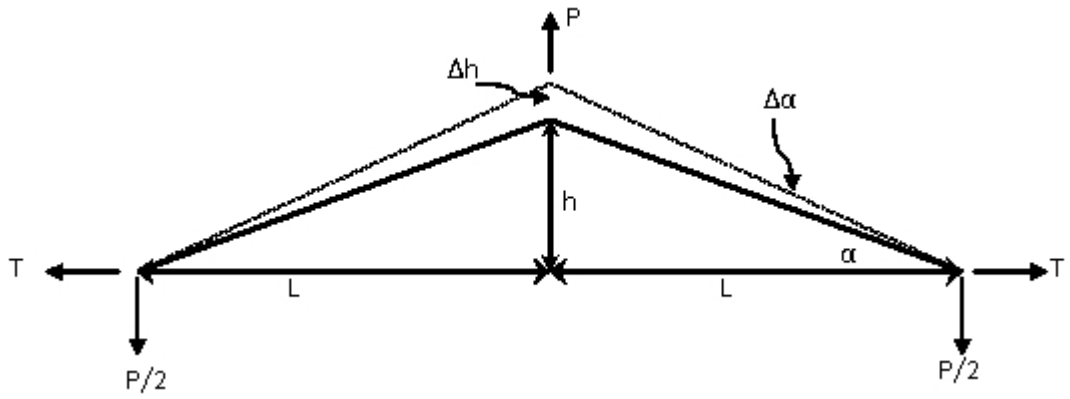

Figure 2.2: Free Body Diagram of Instrument

(Δh) and the force required (ΔP) is a function of the axial force in the cable (ΔT). In order to make calculations, however, some assumptions should be made about the geometry and the materials. These assumptions are as follows:

- Behavior of the cable and all the equipment is assumed to be linear. No yielding or geometric non-linearities are considered.
- The axial force in the cable is assumed to be constant during testing (In the experiment phase, it is found that this assumption does not exactly hold, however the changes are still very low and negligible).
- The flexural stiffness of the cable is assumed to be zero.
- Cable deformation angle (α) is small ($\alpha < 10°$) and $\alpha = \sin(\alpha) = \tan(\alpha)$ ($h \ll L$).

Considering a statically determinate system and small deformations (Figure 2.2);

$$\alpha = \frac{h}{L} \tag{2.2}$$

Assuming the length does not change (i.e. L is constant);

$$\frac{d\alpha}{dh} = \frac{1}{L} \tag{2.3}$$

$$\Delta\alpha = \frac{\Delta h}{L} \tag{2.4}$$

Taking moment of BC with respect to point B (Figure 2.6),

$$t \cdot h = \frac{P}{2} \cdot L \tag{2.5}$$

$$\frac{h}{L} = \frac{P}{2T} = \tan(\alpha) \approx \alpha \tag{2.6}$$

$$T = \frac{L \cdot P}{2 \cdot h} = \frac{P}{2 \cdot \alpha} \tag{2.7}$$

Assuming that T value is constant (L is also constant, as assumed before),

$$\frac{dP}{dh} \approx \frac{2 \cdot T}{h} \rightarrow T \approx \frac{\Delta P}{\Delta h} \cdot \frac{L}{2} \tag{2.8}$$

If T is a function of h;

$$\frac{dP}{dh} = \frac{2T}{L} + \frac{2h}{L} \cdot \frac{dT}{dh} \tag{2.9}$$

2.3.2 Instrument

In order to be able to use Equation 2.8, the parameters Δh and ΔP should be measured. The solution of this problem is derived from the geometry and the nature of the constructed

Figure 2.3: General view of instrument

instrument (Figure 2.3). Dimensions of the instrument can be seen in Figure 2.4 and Figure 2.5.

Considering the dimensions given, if a load of P is applied from the central screw to the system (Figure 2.6) , at the central point A:

$$\sum M = 0 \Rightarrow M_D = \frac{P}{2} \cdot 33.75 = 16.375P\,(kN.cm) \tag{2.10}$$

At the point of gages B;

$$\sum M = 0 \Rightarrow M_B = \frac{P}{2} \cdot 27.5 = 13.75P\,(kN.cm) \tag{2.11}$$

From the sectional dimensions given in Figure 2.7;

$$\bar{y} = 33.5\,mm\,from\,bottom\,(from\,symmetry) \tag{2.12}$$

$$\sum A = [(35 \cdot 8.5) \cdot 2 + (50 + 2 \cdot 8.5)] \cdot 2 = 2329\,cm^2 \tag{2.13}$$

$$I_{total} = (\frac{8.5 \cdot (50 + 2 \cdot 8.5)^3}{12} + \left[\frac{35 \cdot 8.5^3}{12} + (8.5 \cdot 35) \cdot \left(33.5 - \frac{8.5}{2}\right)^2\right] + \left[\frac{35 \cdot 8.5^3}{12} + (8.5 \cdot 35) \cdot \left(58.5 + \frac{8.5}{2} - 33.5\right)^2\right]) \cdot 2 = 1.451e6\,mm^4 \tag{2.14}$$

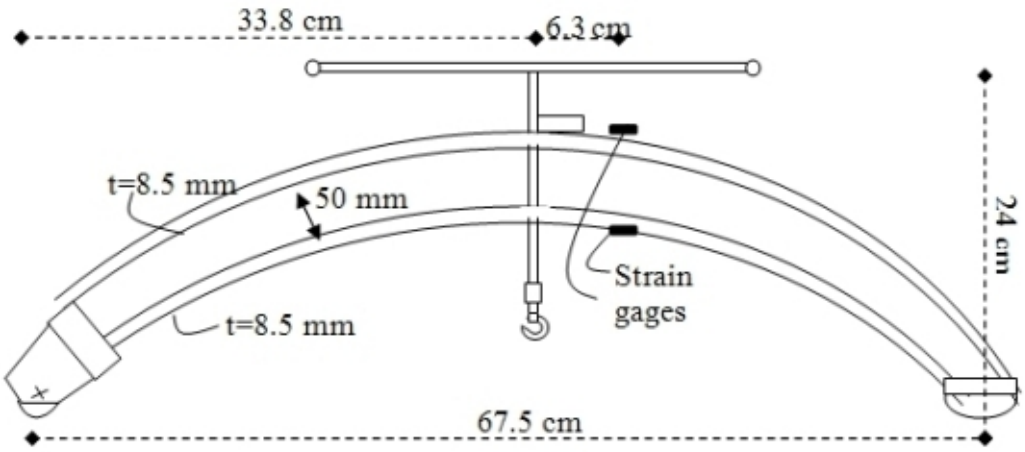

Figure 2.4: Side view of the instrument with dimensions

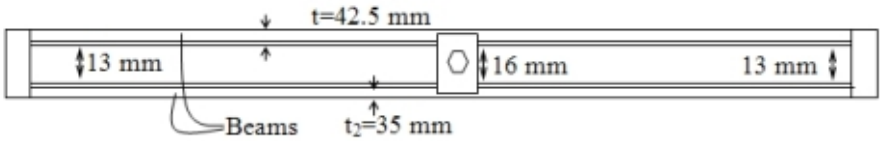

Figure 2.5: Top view of the instrument with dimensions

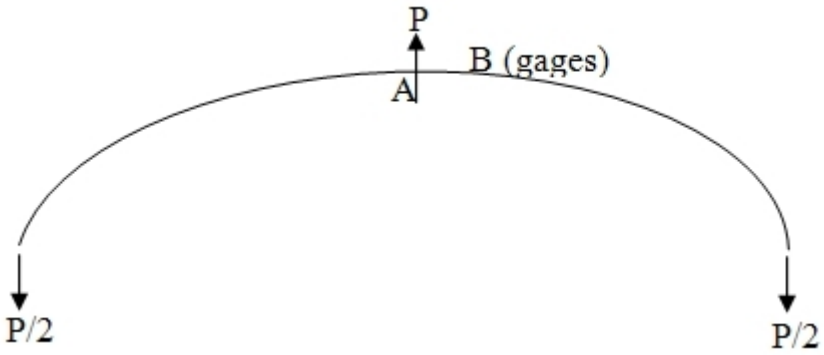

Figure 2.6: Free body diagram under load P

Considering the moment at section A (Figure 2.6) of the arch, assuming modulus of elasticity of steel as 210 GPa, the strains at the top of upper flange (1), bottom of upper flange (2), top of lower flange (3) and bottom of lower flange (4) of the section can be calculated in Equation (2.16) and Equation (2.17).

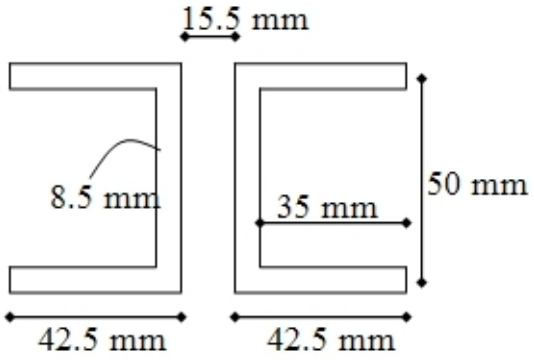

Figure 2.7: Sectional dimensions

$$\sigma_1 = \frac{(16.375P) \cdot 3.35}{145.14} = 37.8P\ MPa \tag{2.15}$$

$$\Rightarrow \epsilon_1 = \frac{3.78P}{20000} = (1.89 \cdot 10^{-4}) \cdot P\ (P\ in\ kN) \tag{2.16}$$

$$\epsilon_2 = (1.41 \cdot 10^{-4}) \cdot P,\ \epsilon_3 = (1.41 \cdot 10^{-4}) \cdot P,\ \epsilon_4 = (1.89 \cdot 10^{-4}) \cdot P \tag{2.17}$$

There are four 120.2 ± 0.2 Ω strain gages on the instrument, connected as a full Wheatstone bridge (Figure 2.8). In this type of bridge connection, the output voltage can be calculated as in Equation (2.18).

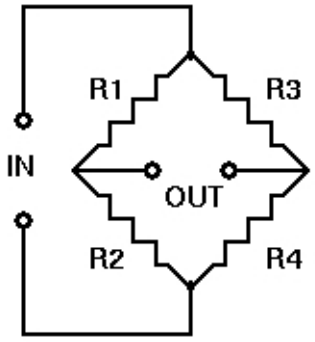

Figure 2.8: Full Wheatstone bridge

$$e_0 = E \cdot K_s \cdot \epsilon_0 \tag{2.18}$$

For maximizing the voltage output, discarding temperature effects and other strains than bending, the strain gages 1 and 3 are put to the top of the beam of instrument and resistances 2 and

4 are put to the bottom. Since the temperature effect will cause equal amounts of change on the output voltage of individual gages, their effects will cancel each other. On the contrary, bending moments in the beam due to load effect will cause negative change (compression) at top fibers and positive change (tension) at bottom fibers. Inserting these values to the bridge equation, they are combined, leading to the maximum output available. In addition, thermal effects of the lead-wires are canceled.

The Δh value can be measured from the central screw using the thread distance which was measured as 2 mm; therefore, every full turn of the top rod increases Δh 2 mm. For measuring the ΔP, the stress – strain relations are considered. As the force P changes, the strains on the points of the strain gages change, too. This change can be measured and correlated with the change in force, ΔP.

For a unit load of 1 kg as ΔP, the voltage values to be read as output can be calculated as in Equation (2.20).

$$\epsilon = (1.89 \cdot 10^{-4}) \cdot \frac{1 \cdot 9.81}{1000} = 1.854 \cdot 10^{-5} \tag{2.19}$$

$$e_0 = (2500\,mV) \cdot (2.10) \cdot (1.854 \cdot 10^{-5}) = 0.097\,mV \tag{2.20}$$

2.3.3 Experiments

2.3.3.1 Calibration Experiments with Static Weights

Before the instrument can be used in the field, several experiments in a controlled environment should be conducted in order to:

- Perform a calibration process,
- Identify weak points and problems,
- Make necessary improvements.

The experiments are conducted in the structural mechanics laboratory of the Middle East Technical University Civil Engineering Department.

First of all, before making measurements on an assembled cable, loads varying from 0 kg to 110 kg were hung to the hook of the instrument and the results were recorded in order determine whether it is operational or not (i.e. checking whether the gages are appropriately bonded, the connections are working... etc), and additionally the data was processed to find a conversion constant that will be used to convert the measured voltage to the load applied (Figure 2.9).

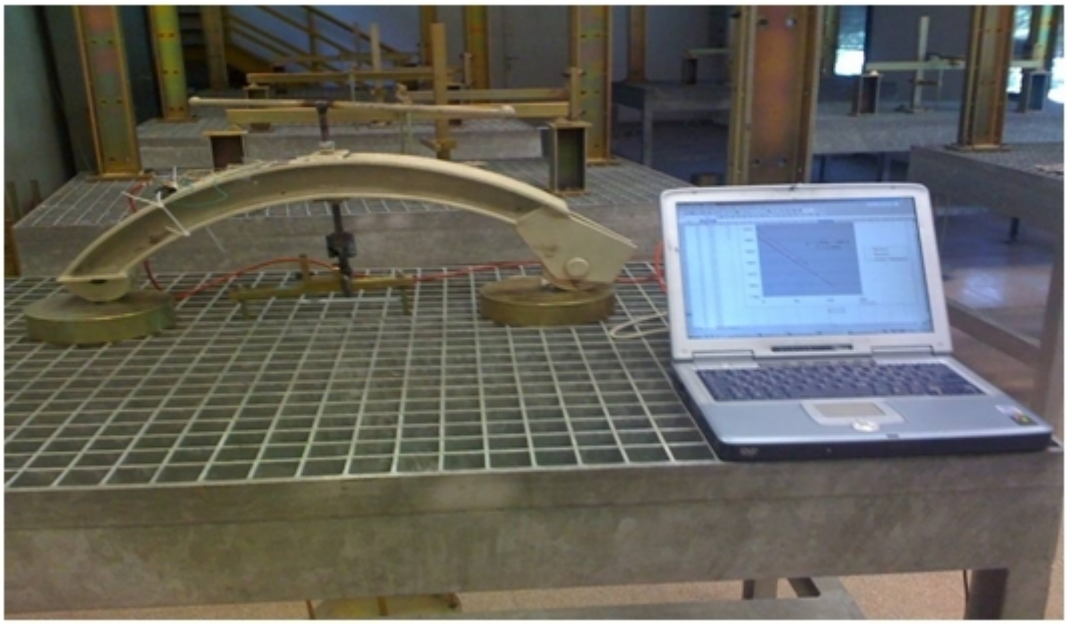

Figure 2.9: Static loading test overview

The loading cycle from 0 to 110 kg and then back to 0 kg was repeated five times and the data was recorded for further investigation of the correlation between the voltages read from the Wheatstone bridge and the load applied to the system. After a through processing, the output is found to be;

$$y = 0.8466 \cdot x + 1836.4 \tag{2.21}$$

where x is the voltage read and y is the load applied, with an average correlation coefficient of 0.9917 in five experiment sets, consisting of 22 loading/unloading each.

In the five graphs in Figure A.1 to Figure A.5, the outputs and processing results are shown, and the blue series (series1) consists of the actual load applied to the system (in kilograms) as x-axis and the calculated load from the given equation as y-axis. Considering they should be same, the points should coincide. The line (named Linear (Series1)) is the result of the linear

regression applied to the actual load – calculated load pair. The slope of this line should be 45°, which means unity in the x-coefficient of the regression equation.

2.3.3.2 Cable Capacity Experiments (Material and Connector Strength)

Before connecting the cable to the experiment setup, however, some additional tests were performed in order to determine the axial force capacity of the cable and the connector locks. For achieving this, three specimens were used. The length of each specimen was around 40 cm, because too long specimens do not fit into the universal testing machine available. In the first experiment, as it can be seen from Figure 2.10, only one lock at each side was used and the orientation was not considered. The result was the failure of the cable from one of the connections, which may indicate problems with the locks. The ultimate force recorded in the experiment was 2.4 tons, which can be considered low with respect to commercially used cables in the market.

Figure 2.10: First specimen before and after test

Figure 2.11: Second specimen before and after test

Figure 2.12: Third specimen before test and its end locks

For further study, another specimen was prepared (Figure 2.11). In the second setup, two locks were used, each oriented opposite to the adjacent one. However, the alignment of them with respect to the cable was again not a concern. The locks were screwed very tight in order to prevent any slippage that may occur during the pulling process. However, this powerful clipping resulted in deforming the geometry of the cable and it is suspected that this configuration may lead to stress concentrations, causing premature failures. As suspected, the specimen failed at 2 tons of tension force from the connection, as before. The failure pattern, however, was like a cut that can be resulted from over-screwing (Figure 2.11). In addition, the circular part of the lock might cut the cable if it was on the test part of the specimen.

Considering all these concerns, a third setup was made (Figure 2.12). In this final specimen, the cable beds of the two locks were put into the testing side of the cable. In addition, the screws were tightened a little more loosely than the previous setups (Figure 2.12). In testing of this final setup, the failure was not rupture of the cable, but the slipping of the cable from the locks at the tension value of 2.2 tons.

The three experiments explained state that for loading values up to 1.7 tons (considering a safety factor on the average 2.2 tons), the scaled testing can be done without the risk of cable failure or connection slipping.

2.3.3.3 Scaled Cable Tests

During the scaled test, in order to determine the load in the cable for calibrating the instrument, a 5 tons capacity load cell was utilized. The load cell was calibrated beforehand by putting

known weights on top of it, and result is;

$$Load\,(in\,kg) = 502.71 \cdot voltage\,read - 26.9 \tag{2.22}$$

The load cell was connected to the CR1000 data acquisition system, which operates under the continuous feeding of 5V. The readings were differential and in the range of 7.5 mV. The load cell and the turnbuckle used to change the axial force in the cable could be seen in Figure 2.13. After all installation and equipment calibration , the experiments started (Figure 2.14). The parts of the experiment are given in Figure A.6 to Figure A.8.

Figure 2.13: Load cell and turnbuckle with base plate

Figure 2.14: Scaled test setup

As several cycles of experiments were made, some problems arose. First of all, the cable used to transmit the voltage output of the strain gages was shielded; however its connections with the gage edges were not. This caused noise and pollution in the recorded data . Secondly, the cable – gage connections were susceptible to physical contact; displacing the cables (which were not fixed to the beams at first) caused fluctuations in the measured data. Third, there were some construction defects in the instrument; the piece connecting the hook to the central screw was too long and it was preventing pulling the cable enough for making good measurement. In order to solve the last problem, the over-long piece is cut and then the rest was welded to the central shaft. After that, the cables were fixed to the beams of the instrument with duct tape in order to prevent unwanted movements and interventions. Finally, the gages and connections were wrapped with aluminum sheet to prevent receiving noise from the environment. The aluminum layer was put on top of a plastic coating, because direct contact with aluminum would lead to short-circuit problems. The procedure followed in the experiment was, first of all, the instrument was attached to the cable and necessary data acquisition connections were established. The initial values, read from the load cell and instrument, were recorded. Later, the rod of the instrument was rotated one full circle (360°) and the values (voltage read from instrument and load cell) in addition to the number of cycles performed up to that point were recorded. By this way, the rod was turned up to 10 full cycles (or 6 – 7 full cycles for cables having high axial force). After that, the cycles were reversed (i.e. the instrument is released) step by step again, with data recording at each stage. This procedure was repeated for a cable load of 500 kg, 750 kg and 1250 kg.

2.3.3.4 Experiment Results

After processing the data and making necessary calculations, the values obtained are tabulated in Table 2.1.

[1]The measured load is obtained by averaging the values read from the load cell attached to the cable at each successful cycle. Therefore, if 10 cycles are performed in an experiment, the measured load is the average of 10 load measurements.

[2]# of cycles denotes how many times the top rod of the instrument is turned. It has effect on the axial load of the cable and it is required in the calculation of the axial load since cycling amount determines how much the cable is pulled.

Table 2.1: Experiment sets and results

Experiment #	Measured Load[1](kg)	# of Cycles[2]	Estimated Load[3]	Difference (%)
Experiment 1	569	10	608	6.5
Experiment 2	738	10	675	8.6
Experiment 3	774	10	825	6.1
Experiment 4	761	10	750	1.5
Experiment 5	800	10	783	2.2
Experiment 6	794	10	808	1.8
Experiment 7	787	10	791	0.5
Experiment 8	1236	9	1129	9.4
Experiment 9	1018	6	916	11.0

As the load in the cable increases, it becomes harder to pull it; therefore # of cycles performed gets lower with increasing measured load.

[3]The estimated load is calculated from the equations of static equilibrium given before (Equation (2.8)), combined with the calibration parameters calculated in the loading experiments.

The high differences in the last two experiments are possibly because of the extreme distortion in the pitch of the central screw due to high axial load in the cable (Figure 2.15).

Figure 2.15: Distorted central screw

CHAPTER 3

NON-DESTRUCTIVE ST-ID AND DAMAGE DETECTION OF BEAM STRUCTURES

3.1 Introduction

Structural properties of existing structures can be different from the time it was constructed due to aging process. The constructed structure at its earliest form may also be different than those in the plans due to variations in geometric or material properties. The gathered information from structures may be used to assess the current condition, load carrying capacity, safety evaluation...etc. Therefore, it is important to identify the current structural properties of a structure.

In this chapter, a method for structural identification (St-Id) and determining structural parameters, checking existence of structural damage together with localization and quantification is proposed. First of all, the preparation studies of the test specimen that is used for the verification experiments are explained. Then the theory behind the suggested method is detailed and reference tests are introduced. Moreover, damage scenarios and the tests conducted under these scenarios are given in detail, with the processing mechanics and interpretation of the results for increasing overall quality and stability of experiments and processing method. Finally, the results are presented using comparisons and comments on the results in terms of accuracy and stability.

The damage detection and St-Id studies reported in this thesis can be briefly categorized as follows:

1. Check critical load carrying mechanisms of the test beam in order to determine the

maximum test load that will be used for the experimental studies.

2. Compare the static and dynamic properties of different FE models developed in SAP2000, in an attempt to investigate the effect of modeling technique on the structural properties of the FE models.

3. Obtain shear transfer force and section EI relationship.

4. Develop an MS Excel based analytical FE beam model based optimization (calibration) tool to fit analytical deformed shape to the experimentally obtained values of a beam by modifying the EI coefficients of each segment. The summation of error between the analytical and experimental deformed shapes is minimized while the EI coefficients are modified. The number of segments can be selected differently to investigate the effect of number of segments on the EI value distribution.

5. Generate a set of FE models with different levels of complexity using SAP2000 and simulate damage scenarios on the analytical models. Obtain deformed shapes from the analytical models and feed those values to the developed Excel based EI calculator and optimization program. In this way, obtain EI values from the SAP2000 based analytical model.

6. Induce a) half-flange cut, b) full-flange cut, c) full-flange cut at two locations, and d) induce 2/3 web cut at the second full-flange cut location.

7. Compare EI coefficients that are experimentally obtained for different damage scenarios using different number of segments.

8. Compare EI changes obtained from experimentally obtained data and analytical simulations.

The details of the work summarized above are discussed in further detail in the following sections.

3.2 Test Specimen Preparation Studies

In this part, the investigation and calculation of the structural parameters of the test beam are explained. In addition, several checks are made for determining the safety limits that are to

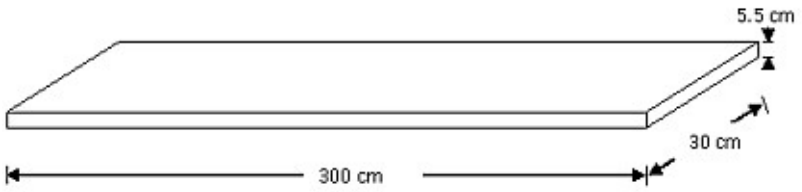

Figure 3.1: Dimensions of the concrete deck

be considered during experiments.

3.2.1 Structural Properties of Test Beam

3.2.1.1 Materials and Dimensions

The 3 m long composite beam used for the verification of the proposed damage identification methods is composed of a reinforced concrete deck and two steel I100 girders. The deck has the dimensions indicated in Figure 3.1, and made of C16 concrete. The two I-beams and the cross-bars have the dimensions shown in Figure 3.2. The girders are of St-37 steel and the cross-bars are welded to the web of the beam. Top flanges of both beams are embedded into concrete for better shear transfer and stability in the concrete – steel connection. No shear studs were used relaying only on the chemical bound between the top flange and concrete deck, which is normally ignored in the design practice. The beam was simply supported and elevated about 30cm from the ground for ease of vertical displacement measurements. Before initializing any tests on the beam, several analysis were done in order to calculate the capacity and failure mechanism of the beam, and to determine loading capacity and pattern.

3.2.1.2 Moment - Curvature Analysis of the Beam

In order to determine the bending capacity of the composite section, a moment curvature analysis was performed with the following assumptions and data:

- For concrete, the strain at which maximum stress in concrete is attained is accepted as 0.002 and the ascending portion of stress - strain curve is assumed as parabolic, whereas the descending part is assumed linear (the general method suggested for unconfined

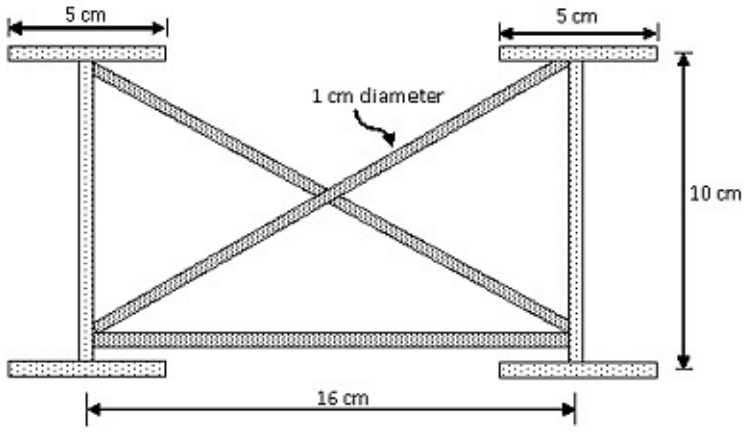

Figure 3.2: Cross-sectional dimensions of the beams and girders

concrete) (Equation 3.1). The given set of equations results in the stress – strain plot given in Figure 3.3. It should be noted that the contribution of concrete to tension is totally neglected.

$$\sigma_c = \begin{cases} f_c \left[\frac{2\varepsilon_c}{0.002} - \left(\frac{\varepsilon_c}{0.002} \right)^2 \right] & if\ \varepsilon_c < 0.002 \\ -185 \cdot f_c \cdot \varepsilon_c & else \end{cases} \tag{3.1}$$

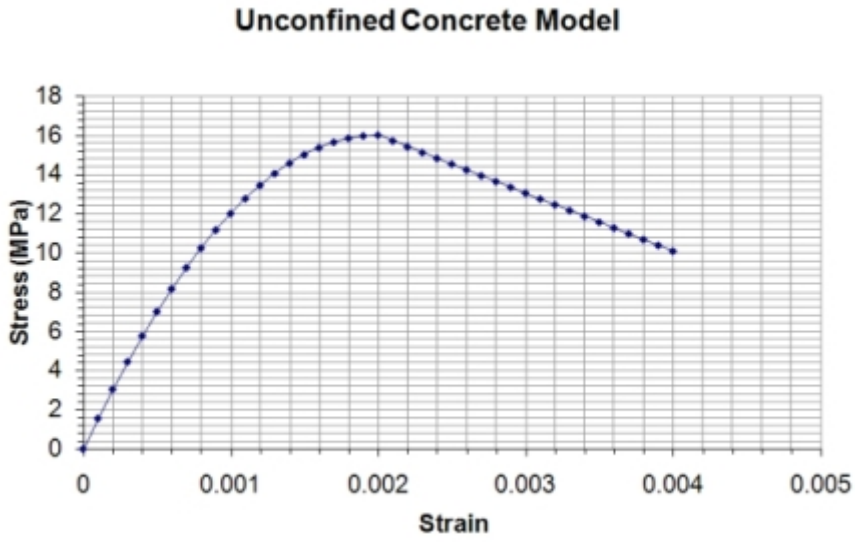

Figure 3.3: Stress - strain model of unconfined concrete

- For steel of the girders, the steel model is assumed to be bi-linear with no strain hardening, with a yield stress of $2.4\,t/cm^2$(Equation (3.2)).

$$\sigma_s = \begin{cases} 2.4 & if\ \varepsilon_s < 0.002\ or\ \varepsilon_s > -0.002 \\ f_y \cdot \frac{\varepsilon_s}{0.002} & else \end{cases} \tag{3.2}$$

The given set of equations results in the stress – strain plot given in Figure 3.4.

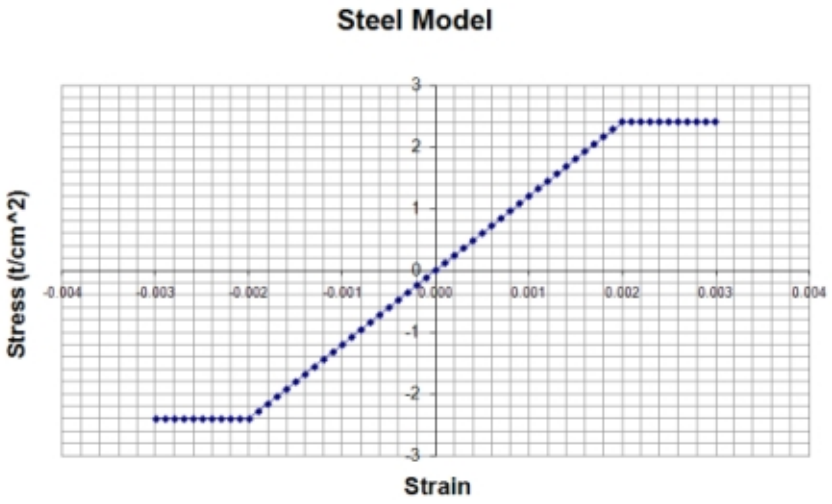

Figure 3.4: Stress - strain model of steel

For calculating the moment – curvature relationship, the cross-section of the beam was divided into segments with finite length. The concrete deck was subdivided into 5 mm slices, with a total of 11 slices. The flanges of the I girders were left unsliced since their thickness is small enough (~6.8 mm). The flange of the beams was divided into 16 strips, each having a thickness of 5.4 mm. All section was converted to steel (using Modulus of Elasticity ratios) and the strain distribution was assumed linear on the converted section. Constraining the net axial force on the section to zero, the moment values for a series of curvature data were calculated via MS Excel (Figure 3.5). From the figure, the point where the moment - curvature relationship loses its linearity can be observed as 1.6e7 N.mm. Assuming a point load over the beam (which will be the case in the testing procedure), the maximum moment over the span will be (P x L) / 4. Since the length of the beam (L) is 3 meters, the limiting value of point load for preserving linearity from the flexural point of view is 21333 N or ~2.1 tons.

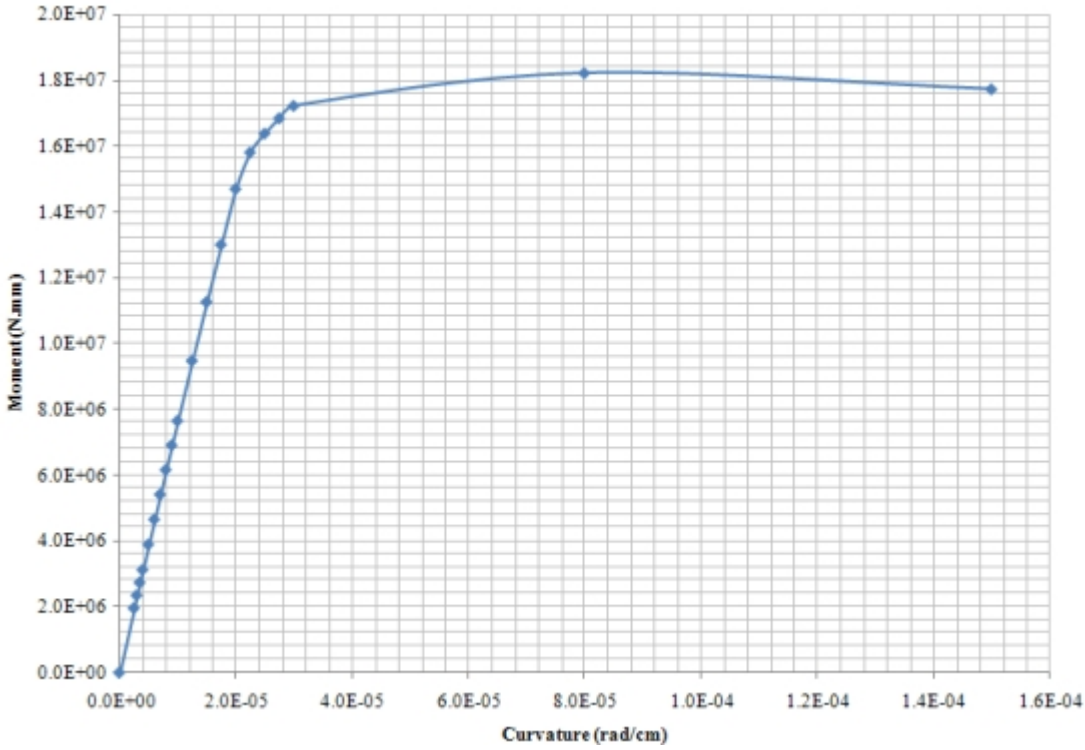

Figure 3.5: Moment - curvature diagram obtained

3.2.1.3 Web Crippling Check

As the steel beams rest on supports, the phenomenon of web crippling should be checked in order to ensure that no damage occurs at the support locations during the testing procedure. The method proposed by Yilmaz, Ç., and Akkas, N. is used [15]. For the given parameters in Figure 3.6, if P is the reaction at a support, inequality in Equation 3.3 should be valid in order to prevent the necessity of stiffeners or spreading the reaction over a greater length.

$$\frac{P}{t_w(N+k)} \leq 0.75\sigma_a \tag{3.3}$$

In the calculations, the support is assumed to rest at the end of the beam, which leads to more conservative results since decrease in the (N+ k) term will result in a lower allowable P. For an I100 section, flange thickness is 0.68 cm, web thickness is 0.45 cm, radius of web - flange connection is 0.45 cm and for the steel used, allowable stress is 2.4 t/cm^2. If the maximum load allowable is P (in kg), Equation 3.3 will yield:

$$(N + t_f + r) \cdot t_w \cdot 0.75\sigma_a \geq P \Rightarrow 1.13 + N \geq 1.235 \cdot 10^{-3} \cdot P \tag{3.4}$$

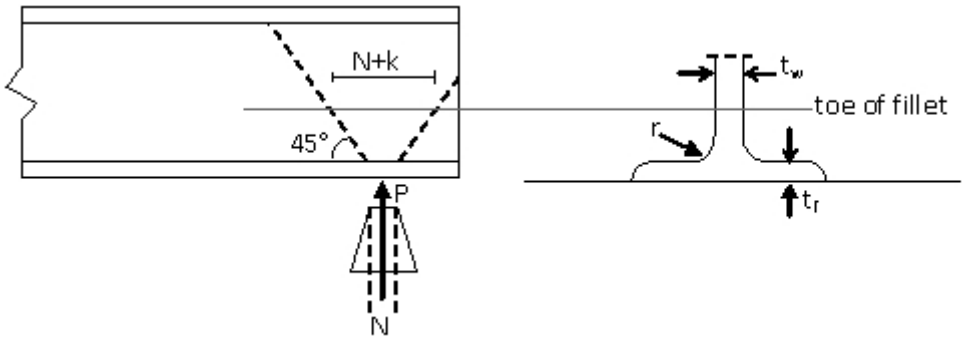

Figure 3.6: Web crippling check parameters

In order to prevent the obligation to take measures against web crippling, N is assumed to be zero, thus the maximum value of P could be 1009 kg.

3.2.1.4 Shear Checks

The total shear flow q on the cross-section for an estimated load of 700 kg is;

$$q = \frac{V \cdot Q}{I_{total}} = 54\,kgf/cm \Rightarrow \tau = 5.4\,kgf/cm^2 = 0.54\,MPa \tag{3.5}$$

As the total shear acting on the section (Equation 3.5) is within acceptable limits (it is less than 1% of the compressional strength of the concrete used), 600 kg load is safe in terms of shear failure.

3.2.1.5 Section Stiffness Calculations

As the beam is composed of different materials (steel and concrete), in calculating EI value of the section a reference material is selected and section is transformed according to the ratios of the modulus of elasticity of materials. As it will be easier to calculate new dimensions of a rectangular shape, reference material is selected as steel.

The I100 sections in the beam have 10.8 cm^2 area and 171 cm^4 moment of inertia. The Young's modulus of St37 steel is taken as 2 100 000 kgf/cm^2[16] and C16 concrete is taken as 27 000 MPa [17]. Therefore the ratio of the moduli is:

$$n_s = \frac{E_s}{E_c} = \frac{2100000\,kgf/cm^2}{275300\,kgf/cm^2} = 7.63 \tag{3.6}$$

For calculating the total moment of inertia of the composite cross-section, the shear transfer between concrete deck and steel girders should be estimated. The limiting values are full shear transfer (total bonding of steel and concrete with shear locks) and no shear transfer (loss of adhesion with no shear locks). In the first case, the composite section acts as a whole against bending and the location of the new centroid should be calculated:

$$\bar{y} = \frac{(5 \cdot 10.8) \cdot 2 + (5.5 \cdot 3.93) \cdot 12.75}{10.8 \cdot 2 + (5.5 \cdot 3.93)} = 8.88\,cm \tag{3.7}$$

The moment of inertia of the cross section can be calculated by parallel axis theorem:

$$\left[171 + \left(10.8 \cdot (8.88 - 5)^2\right)\right] \cdot 2 + \left[\frac{1}{12} \cdot 3.93 \cdot 5.5^3 + \left(3.93 \cdot 5.5 \cdot (12.75 - 8.88)^2\right)\right] = 1045.39\,cm^4 \tag{3.8}$$

Thus, the EI of the steel-transformed section can be calculated as:

$$2100000 \cdot 1045.39 = 2.19 \cdot 10^{11}\,kg \cdot mm^2 \tag{3.9}$$

In the second case, the steel-transformed deck and the girders each behave independently, bending around their own centroid.

$$I_{total} = 2 \cdot 171 + \frac{1}{12} \cdot \left(3.93 \cdot 5.5^3\right) = 396.488\,cm^4 \tag{3.10}$$

$$EI_{total} = 0.832 \cdot 10^{11} kgf \cdot mm^2 \tag{3.11}$$

3.2.1.6 Determination of Moving Test Load

From the capacity calculations concerning the failure modes of flexure, shear, and web crippling, test specimen is found to be able to sustain loads of 2.1 t, 1.0 t, and 0.7 t, respectively. Therefore, for the validation experiments, the loading value is set as 0.6 t.

3.2.2 Finite Element Modeling

In order to determine realistic static and dynamic properties of the test beam, a proper analytical model of it needs to be constructed using the finite elements method. However, there are many alternative ways to do this, and in order to investigate effects of different modeling methods, several different FE models are built. When the analytical models having different modeling techniques are compared against each other, the important differences between models are found and the reasons lying beneath these discrepancies are investigated. Even though the test beam is a simply supported and simple beam, a finite element modeling program was not developed and a commercially available analysis software, SAP2000 program by Computers and Structures Inc., was used. The material characteristics and loading on the beam models were kept the same for all models. The deck of the composite beam is reinforced concrete, but the reinforcement is neglected in the calculations. The concrete is modeled as C16 concrete with a modulus of elasticity of 27000 kN/m^2. This value is the result of the equation given in TS-500 [17]. The mass of the concrete per unit volume is $2450kg/m^3$ and the Poisson's ratio is 0.2. For the steel of the girders, the Young Modulus is 210 000 MPa, the mass per volume is 7850 kg/m^3 and the Poisson's ratio is 0.3.

3.2.2.1 Element Types Used in Constructed Models

In construction of the models that are going to be used in analysis, the predefined element formulations are used rather than defining custom ones due to the fact that there are no special conditions that necessitate tampering the properties of the common elements used. There are three types used in models; frame element, thin shell element, and solid element.

As the most commonly used elements of all, the frame element can be used to model beams, columns, braces, links and trusses in planar and three dimensional structures. It is based on the general three dimensional beam–column formulation that can handle the effects of bi-axial bending, torsion, axial deformations, and bi-axial shear deformations. The element uses all six degrees of freedom defined by Cartesian coordinate space at both of its connected and free joints as seen on the right. This element is defined by two nodes on the space and is connected through these nodes where the six degrees of freedom resides (Figure 3.7)[18, 19].

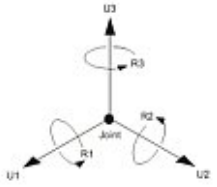

Figure 3.7: Degrees of freedom for frame elements

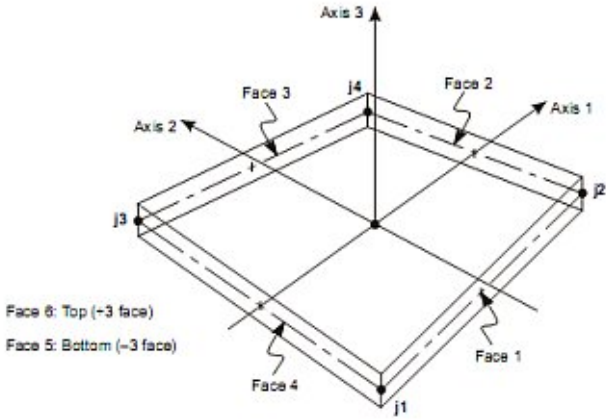

Figure 3.8: Axis and nodes of the thin shell element

The shell element has a formulation based on three or four nodes and behaves as a combination of plate, which acts under bending, and membrane, which acts under axial loads (Figure 3.8). In the creation of models, due to the simplicity of the system, there was no need for triangular (three node) elements or four node elements with out of plane nodes or layered composition. Therefore the plate and membrane behavior are uncoupled. The program considers an isoparametric formulation that includes translational in-plane stiffness components in the direction normal to the plane of the element, and quadratic in-plane displacements. In the plate behavior, two-way, out of plane, plane rotational stiffness components and a translational stiffness component is said to be considered (Kirchhoff element). Due to the nature of Kirchhoff formulation, the transverse shearing deformations are disregarded. It is possible to consider them using a Reissner – Mindlin element, but it will sophisticate the calculations and adversely affect the analysis performance; and the improvements on the results will not be a match for the negative effects, due to the small thickness of the elements. During the calculations, the program uses four-to eight-point numerical integration in stiffness calculations and the required outputs (internal forces, stresses... etc) are evaluated at the 2-by-2 Gaussian

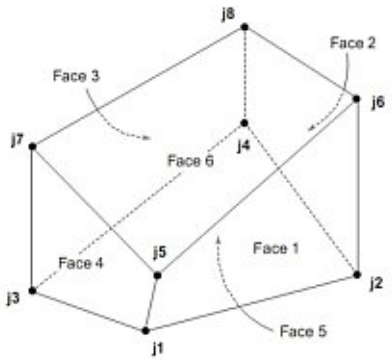

Figure 3.9: Faces and nodes of the solid element

integration points, then extrapolated to the corner joints of the elements. There are some important points that should be considered in modeling with the shell elements; first of all, the inside angle of each corner in a quadrilateral must be less than 180°. The formulations yield the best results when these angles are around 90°, but a range of 45° to 135° will suffice. Secondly, the aspect ratio of an element should not be too large; extremely distorted elements mostly cause erroneous results [18, 19].

The solid element is an eight node element for modeling three dimensional structures (Figure 3.9). It is built on isoparametric formulation that includes nine optional incompatible bending modes. Each element has its own local coordinate system for defining local material properties, local loads and interpreting analysis results. In analysis, 2 x 2 x 2 numerical integration pattern is used to evaluate stresses at integration points and the results are extrapolated to the required joints. The element consists of all three translational degrees of freedom at each node. The rotational degrees of freedom, however, are not activated. Though the element is claimed to perform under rectangular and distorted meshing conditions, several precautions similar to previous model limitations should be kept in mind [18, 19]:

- The inside angle at each corner of the faces must be less than 180°. Optimum angles are near 90°, or at least within 45° to 135° range.
- The aspect ration of an element should not be too large. For the three dimensional element, the aspect ratio is defined as the ratio of the longest dimension of the element to the shortest dimension. Optimum ratio is unity, but values less than four are acceptable.

Figure 3.10: Finite element model 1

Aspect ratios greater than ten should be avoided.

3.2.2.2 Model with Frame Girders and Shell Deck

The first, also the least complex model is composed of frame elements with thin shells. The girders are pre-defined I100 sections (Figure 3.10). The default parameters for the beam are as follows:

- Outside height = 100 mm
- Top flange width = 50 mm
- Top flange thickness = 6.8 mm
- Web thickness = 4.5 mm
- Bottom flange width= 50 mm
- Bottom flange thickness = 6.8 mm

The cross bars between the girders are of circular cross-section with outside diameter of 10 mm and thickness of 4.5 mm (the hole has a diameter of 1 mm). The link members that are used to transmit shear, axial force and moment from the deck to the girders (i.e. the force transfer members) are defined as square, but their structural parameters are modified such that they are fully rigid; in other words they do not absorb any energy by deformation. The material of the link is special; it has no mass or weight; therefore it cannot intervene to the static and dynamic properties of the whole system due to its physical quantities. One of the reasons for using link elements is the definition of the shell element used; the formulations are developed in the center line of the element. There are no mathematical nodes at the physical

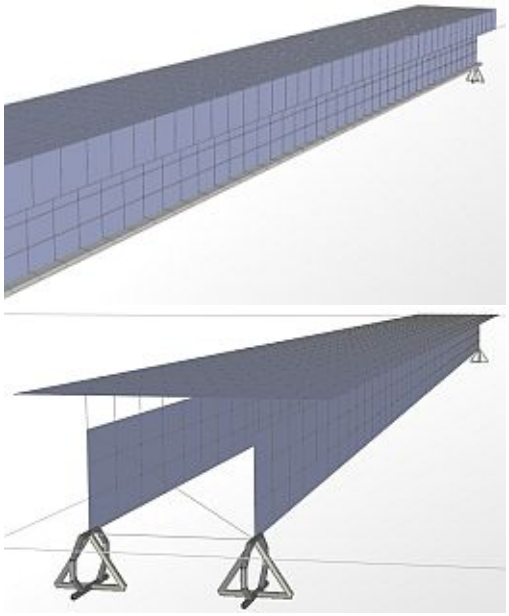

Figure 3.11: Finite element model 2

corners, and because of this, link elements are drawn. Another advantage of these elements is the ability to determine the quantity of force (shear, for example) transferred from deck to the beams. This is especially useful when inspecting the composite action between deck and girders.

3.2.2.3 Model with Frame Flanges, Shell Web and Shell Deck

The second model, though very similar to the first, has one crucial difference; instead of using a pre-defined beam element, the flanges are modeled as line frame elements and the web is considered as a thin shell alongside with the deck (Figure 3.11). The major advantage of this approach is the force and displacement variations throughout the web can be taken as an output of the analysis performed. There is still the need of links since deck and beam top flange elements do not directly touch each other. This type of modeling is slightly more complicated than the previous one and offers more outputs, yet still not able to determine the fluctuations of stresses and strains along the length and width of the top and bottom flanges.

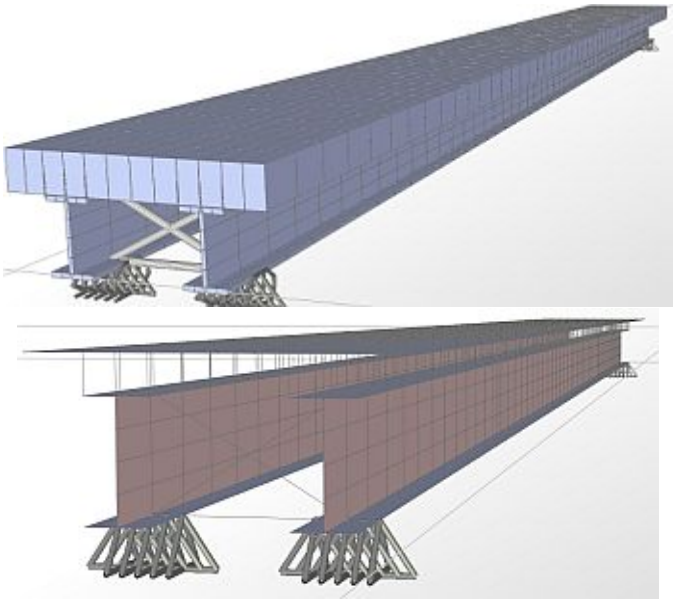

Figure 3.12: Finite element model 3

3.2.2.4 Model with Shell Beams and Shell Deck

The third model is constructed using thin shell elements for beam webs, beam flanges and the deck. The flanges are subdivided so that along the width, internal structural parameters like stress and strain can be traced (Figure 3.12). Similar to the previous models, cross-bars are round line elements and the links are infinitely rigid for correct force transfer.

3.2.2.5 Model with Shell Beams and Solid Deck

The final, which is the most complex model, is created by using thin shell elements for beam webs and beam flanges, and solid elements for the deck. In this final model, the deck part (made of three dimensional solid elements) directly touches the top flanges of girders. Because of this direct contact, defining infinitely rigid links that serve as shear connectors are not necessary (Figure 3.13).

3.2.2.6 Comparison of Four Different Finite Element Models

The four analytical models are first compared according to their behavior under the action of the identical loading conditions. The displacement profiles for all the analytical models

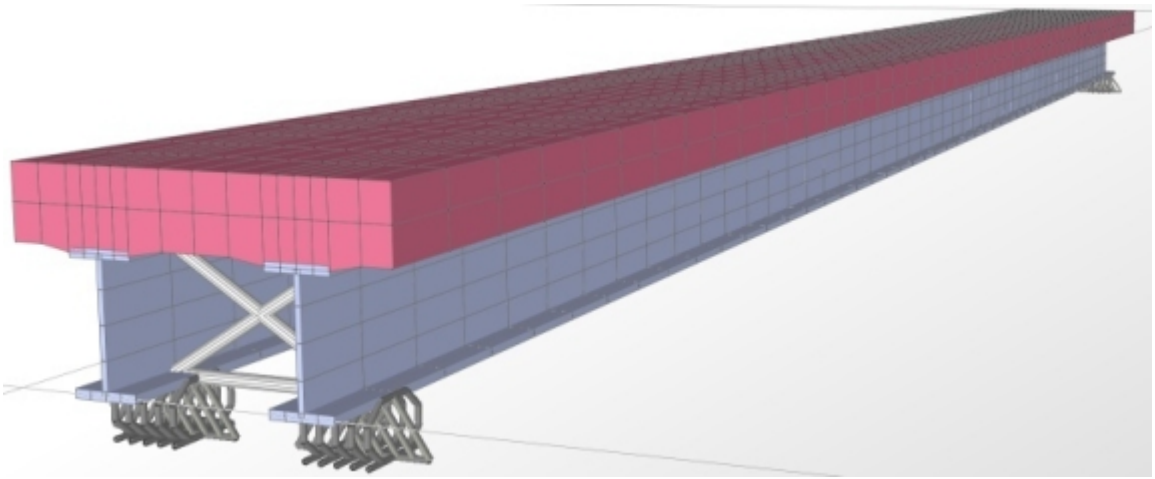

Figure 3.13: Finite element model 4

for the same point load acting on the center of the models are given in Figure 3.14. The displacements obtained from the four different models under the same point load at center shows that the displacements are less sensitive to the element type and pattern, considering all the three models except the first model displays almost the same displacements. Therefore, as the main comparison criterion, dynamic properties of the models are considered.

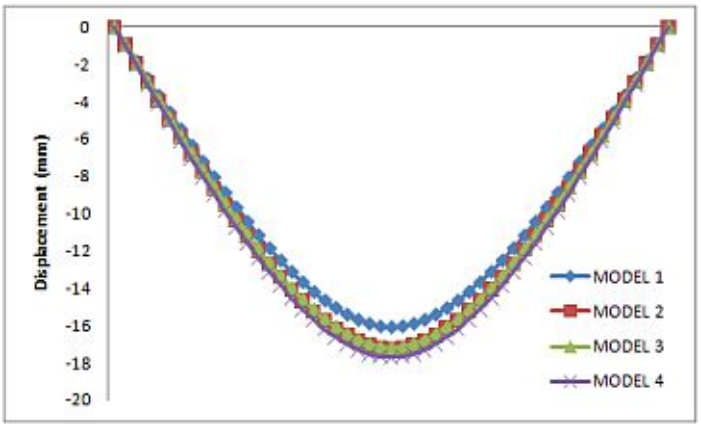

Figure 3.14: Displacements of Four Different Models under the Same Point Load

Another comparison basis for the four models is the results of the modal analysis, because it involves all the parameters that need to be compared like mass, stiffness, and boundary conditions of the structure (Table 3.1). However, it should be noted that direct comparison of the outputs listed is not the most suitable method. In essence, it will lead to wrong conclusions

because the mode numbers in all three models are not unique. In other words, mode 4 may resemble different results; one could be the first longitudinal and other could be the first torsional mode.

In order to make this distinction and converge to correct determination, a parameter that is calculated by using both the frequencies and the mode shapes is required. Modal Assurance Criterion (MAC) is defined as a scalar constant relating the degree of linearity (consistency) between one modal and another reference modal vector [20].

$$MAC_{cdr} = \frac{\left| \sum_{q=1}^{N_O} \Psi_{cqr} \Psi_{dqr}^{*} \right|^2}{\sum_{q=1}^{N_O} \Psi_{cqr} \Psi_{cqr}^{*} \sum_{q=1}^{N_O} \Psi_{dqr} \Psi_{dqr}^{*}} \tag{3.12}$$

or using vector operators:

$$MAC_{cdr} = \frac{\left| \left\{ \Psi_{cqr} \right\}^T \left\{ \Psi_{dqr}^{*} \right\} \right|^2}{\left\{ \Psi_{cqr} \right\}^T \left\{ \Psi_{cqr}^{*} \right\} \left\{ \Psi_{dqr} \right\}^T \left\{ \Psi_{dqr}^{*} \right\}} \tag{3.13}$$

The MAC can take values in the range of zero, which means no correspondence, to unity, which means full correspondence. Therefore, if modal vectors of the same mode obtained from different models are put into MAC calculations, their relevance can be assessed. The criterion should approach to unity if the modal vectors exhibit consistent and linear relationship. One important note here is that MAC cannot be a sign of validity . If the MAC value calculated is close to zero, it is an indication that the modal vectors used are not consistent. There can be several reasons of it, like the system can be non-stationary, there is too much noise in the reference modal vector, the modal parameter estimation is invalid or the modal vectors are from linearly unrelated mode shape vectors. In the case of this study, all these exceptions are irrelevant when comparing dynamic results of analytical models except the last one; therefore if the MAC is nearly zero, the only conclusion is the modal vectors are of the different modes (which at the same time checks the orthogonality of the two modes). On the contrary, if the MAC is close to unity, it is an indication of consistent modal vectors. Though there are different causes of this like incompletely measured modal vectors, modal vectors that are the result of forced excitation other than the required input, modal vectors that are primarily coherent noise, or the modal vectors representing the same modal vector with different arbitrary scaling. Considering that the data used is solely analytical model output, the only possible explanation for a MAC value near unity is the two vectors representing the same modal vector.

Table 3.1: Dynamic properties of four distinct models

	MODEL 1			MODEL 2		
	Period	Frequency	CircFreq	Period	Frequency	CircFreq
Mode Number	Sec	Cyc/sec	rad/sec	Sec	Cyc/sec	rad/sec
1	0,047107	21,228	133,38	0,046141	21,673	136,17
2	0,028111	35,573	223,51	0,036947	27,066	170,06
3	0,014184	70,503	442,98	0,01626	61,502	386,43
4	0,012947	77,239	485,31	0,01509	66,271	416,39
5	0,009874	101,28	636,33	0,013153	76,029	477,7
6	0,0066	151,52	952,06	0,009203	108,66	682,72
7	0,006448	155,08	974,41	0,007765	128,78	809,13
8	0,005483	182,38	1145,9	0,007189	139,1	874,02
9	0,005385	185,71	1166,9	0,005984	167,12	1050
10	0,004176	239,48	1504,7	0,00567	176,38	1108,2
11	0,003939	253,88	1595,2	0,005642	177,23	1113,6
12	0,003631	275,42	1730,5	0,005474	182,7	1147,9
	MODEL 3			MODEL 4		
	Period	Frequency	CircFreq	Period	Frequency	CircFreq
Mode Number	Sec	Cyc/sec	rad/sec	Sec	Cyc/sec	rad/sec
1	0,04602	21,73	136,53	0,045915	21,779	136,84
2	0,029082	34,386	216,05	0,027198	36,767	231,02
3	0,013995	71,456	448,97	0,01298	77,039	484,05
4	0,01267	78,926	495,91	0,012171	82,162	516,24
5	0,00993	100,71	632,77	0,009335	107,13	673,1
6	0,006928	144,33	906,88	0,006625	150,94	948,39
7	0,006628	150,87	947,96	0,006133	163,05	1024,5
8	0,005519	181,21	1138,6	0,005242	190,78	1198,7
9	0,005465	182,99	1149,8	0,005072	197,17	1238,9
10	0,004413	226,62	1423,9	0,004267	234,35	1472,5
11	0,004278	233,76	1468,7	0,004212	237,41	1491,7
12	0,004105	243,61	1530,7	0,004095	244,19	1534,3

For each four of the finite element models constructed, a total of 12 modes and mode shapes are calculated with Eigenvector analysis. In addition, the MAC coefficients for different modes are calculated. Therefore, instead of a scalar value, a 48-by-48 matrix is created as MAC matrix. Considering the inefficiency and impracticality of working on a matrix of that magnitude, results are graphed by using surface plots (Figure 3.15). If Figure 3.15 is detailed for the first five modes (the most dominant ones), the results obtained are given on Figure 3.16.This figure shows the numerical values of the frequencies for the four models (whose colors are identified in the legend at the right). The square surface plots on top of each bar chart group show the MAC values for that mode. Contrary to the plot before, blue color represents MAC close to unity and as the correlation weakens, the colors darken. As it is seen, the MAC values for the first mode is very high, almost close to unity and the frequencies are very close to each other. However, even in the second mode, the correlation between the first and the fourth model drops drastically. Therefore, it will be better to compare the first two and last two models with each other.

3.2.2.7 Calculating Relation between Shear Transfer Ratio, Link Stiffness, and Section EI

The level of existing shear force transfer between the concrete deck and the steel girders strongly affects section stiffness parameter EI, and the numerical value of EI is calculated for both scenarios; fully existing and no composite action. In this stage, further studies are done on the finite element models to find out how changing the shear link stiffness affects overall section stiffness and the shear force distribution in the links along the length of the beam. If a valid relation is to be found, it can be stated that for a given EI, the level of existing composite action can be deduced without the need of further computations.

In the work flow, the third analytical model, which is all made of shell elements is used due to the fact that in the fourth analytical model (having solid elements) there are no shear links and force transfer is between the deck and girders directly, without the involvement of third element type whose structural properties can be modified. For calculating the shear force distribution, a point load at center is used, and for determining section EI, the same approach with the experiments is utilized; beam is loaded from three locations, displacements at 11 stations are taken as output and mathematical model calibration is performed with only one

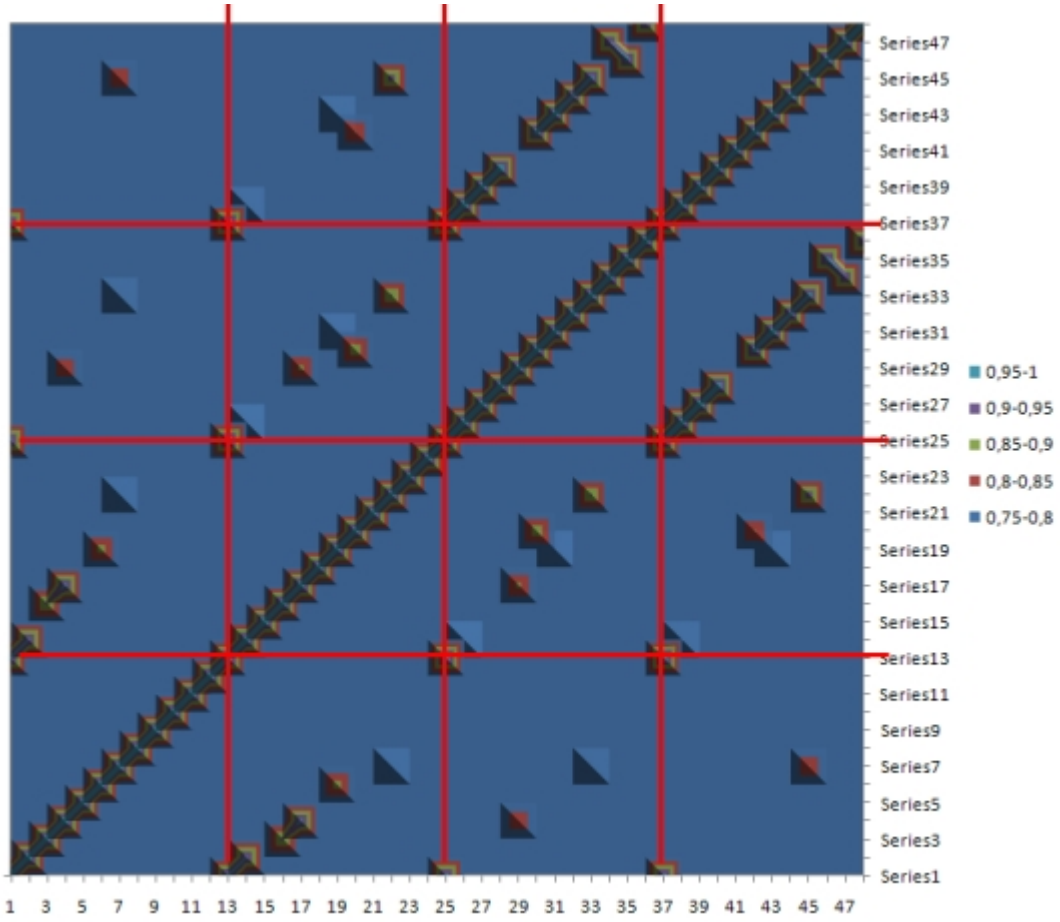

Figure 3.15: MAC values for all modes of all models

segment. Then stiffness of the links is dropped to one tenth of its value, and this pattern is repeated.

From the principles of strength of materials, the results can be estimated qualitatively; as the stiffness of the links increases, the bending stiffness of the system have to increases too, up to a limit where shear transfer ratio reaches unity (100%). After that point, upsurging link EI will have no effect. Similarly, beyond a lower limit of link stiffness, shear transfer ratio becomes zero and lower limit of the system EI is reached; further diminishing link properties will not deter the system.

The calculation is done in nine steps, link EI multiplier is dropped from 10^6 to 0.1 by steps of 10 (except between 10 and 1, where 5 is also considered as a intermediate step, considering the high rate of change in parameters in that range). The relation between link stiffness and

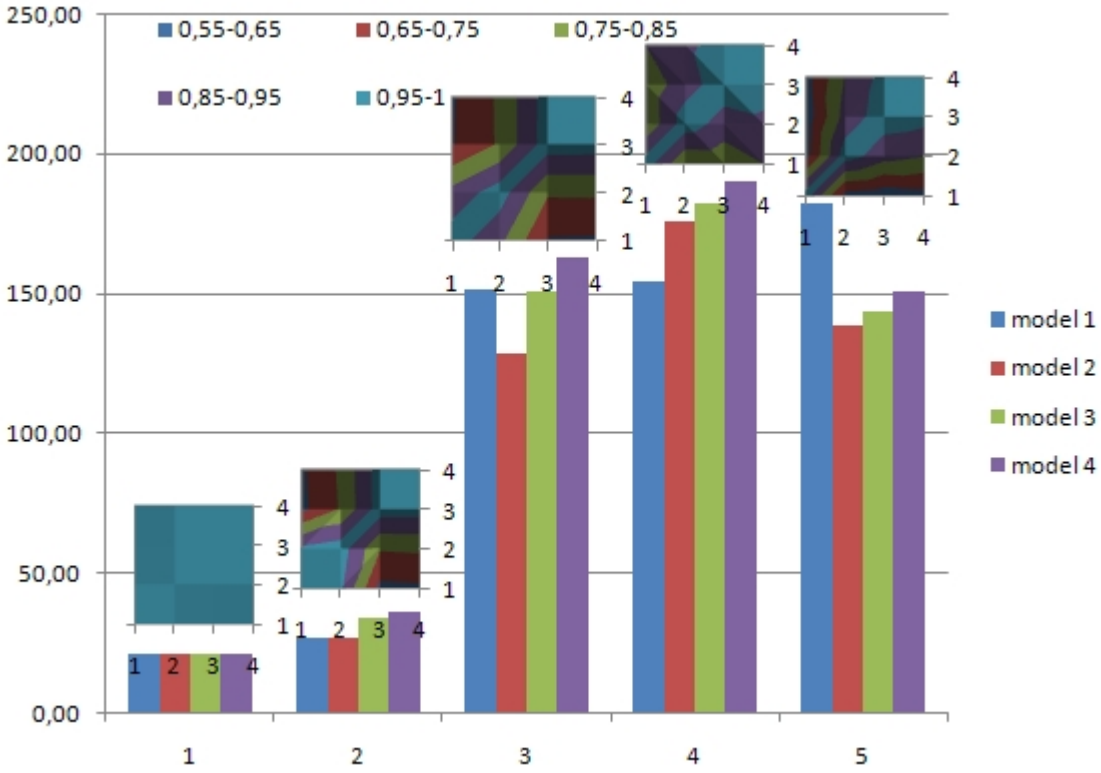

Figure 3.16: First five modes of four distinct models

section stiffness is exactly as proposed (Figure 3.17). As expected, results of the finite element model converges to hand calculations (Section 3.2.1.5) in the full and zero percentage of composite action.

The relation between link stiffness and shear force distribution in the links along the length of the beam is also similar to the previous one; increasing the stiffness of a link will increase the load in them (Figure 3.18).

Most importantly, section stiffness is shown to be correlated with the link stiffness linearly (Figure 3.19). The linearity show that for a calculated EI, the shear force distribution (thus the level of the composite action) can be predicted.

One point is, there are many links existing in the model, and by stating “link shear force” in the above graphs, the average of shear force in the half of the beam is considered. The whole distribution for all steps can be seen in Figure 3.20.

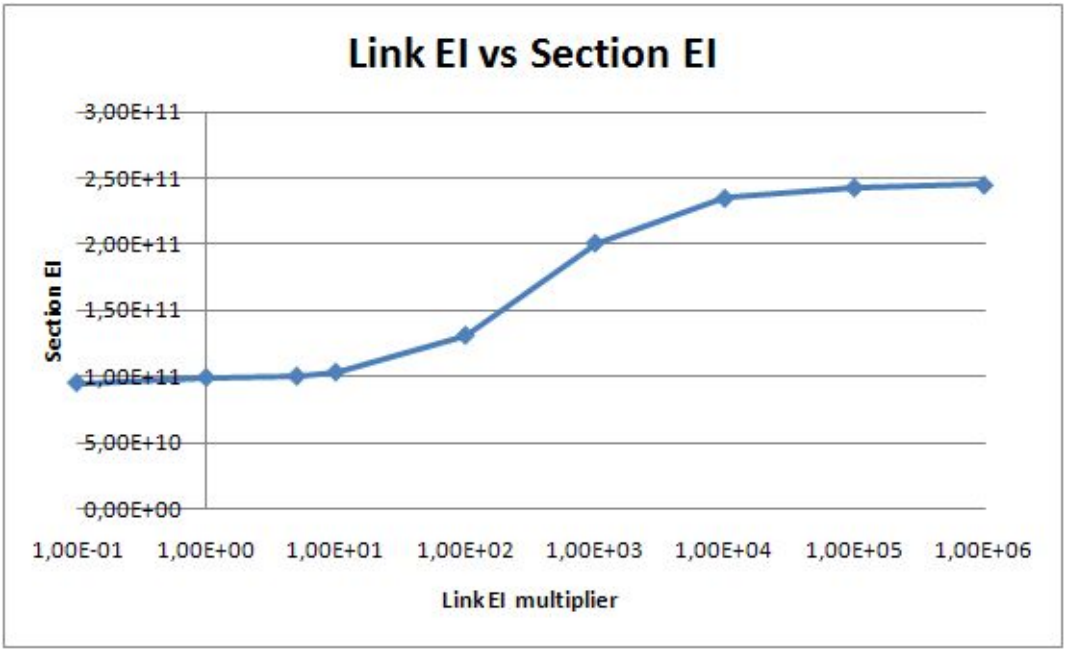

Figure 3.17: Relation Between Link Stiffness and Section Stiffness

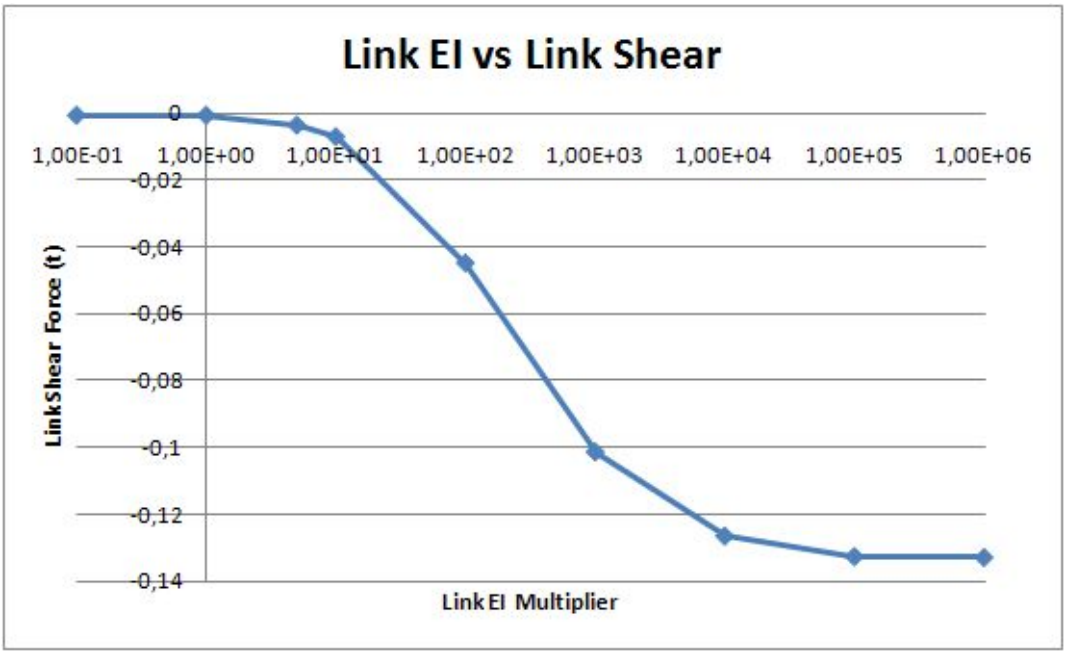

Figure 3.18: Relation between link stiffness and link shear force

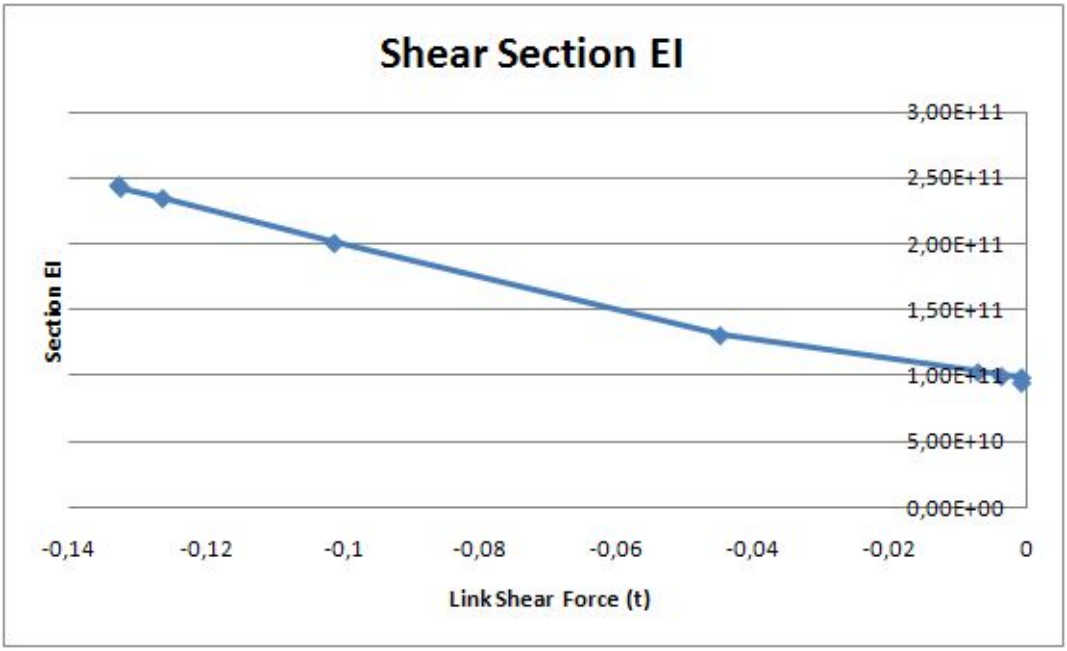

Figure 3.19: Relation Between Link Shear Force and Section EI

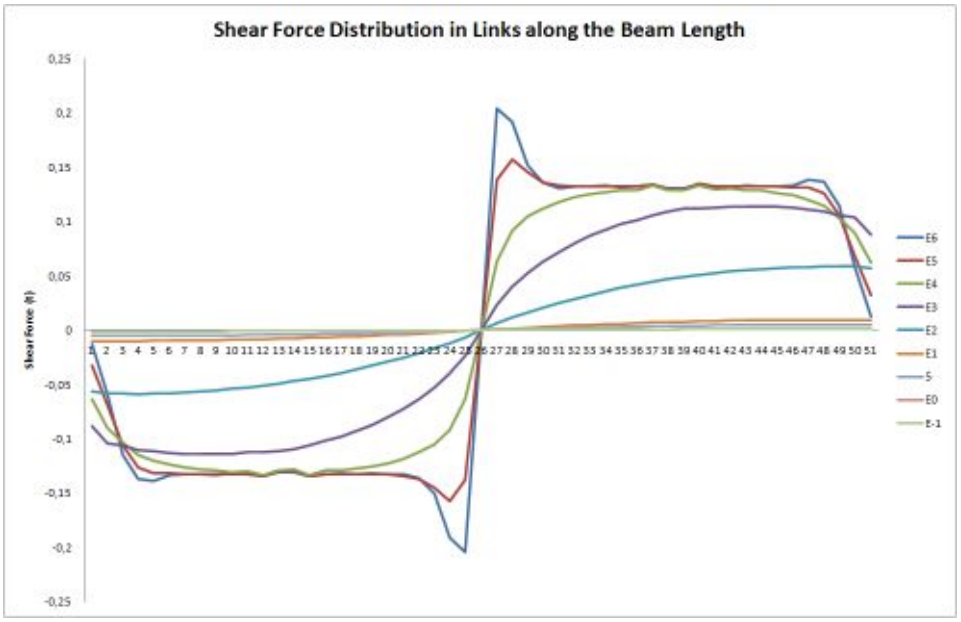

Figure 3.20: Shear Force Distribution along Beam Length

3.2.3 Theory and Reference Tests

In the context of this study, the phrase "structural identification" mostly refers to determining the EI parameters of the lab beam; this parameter (E, modulus of elasticity, multiplied by I, the section moment of inertia) compactly and effectively represents the condition of the material and the section at a location. This is simply because major structural responses of a system (deflection, modal frequencies, mode shapes, etc.) depend on the length, mass, and EI; therefore, identifying EI value is the primary concern in this structural identification study. In addition, it is assumed that unless there is a change in materials or cross-section, the EI of a system (for example a beam) is constant. However, if there is deterioration in material, loss of composite action, or crack/physical defect at a certain portion of the beam, the EI value at that particular location is expected to change. Detecting this difference and locating it would serve as a method of structural damage identification. The supports are assumed to be rigid and any minor flexibility was ignored.

Computing EI of the sample beam is primarily done by calibrating stiffness values of a mathematical model by matching the displacements calculated using principles of structural mechanics and measured by experiments. The mathematical model, which is based on the general stiffness principles, is constructed by considering only the vertical and rotational degrees of freedom at 25 cm intervals, and 22 by 22 stiffness matrix of the system is created (Figure 3.21). Each section has its own EI coefficient, therefore damaged sections (segments with

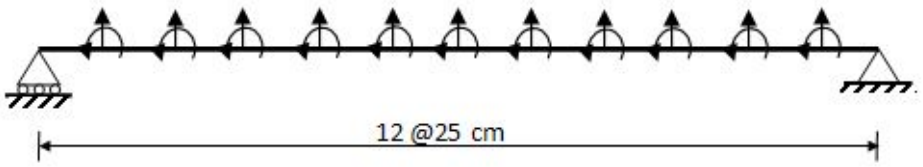

Figure 3.21: DOFs in Mathematical Model

different EI values) can be found out. Then using the load matrix and an assumed initial EI values, displacements are calculated. The load vector is determined by analyzing the loading pattern in the execution of the experiments; the magnitude of the load is 600 kg and the locations are the points where displacement measurements are done by LVDTs. The initial (assumed) EI values are the first trials. Then the objective function is defined as the square

of the differences between displacements calculated in this manner and displacements measured in experiment. The aim is to minimize the objective function by changing the individual EI values; thus obtaining the sectional stiffness for each and every segment. This sectional stiffness is the key point in structural identification, and also can be used as an indication of damage.

For the calculations based on the data gathered from experiments, the noise is a factor that needs to be eliminated. One basic assumption accepted throughout all the experiments and calculations is that the noise is random; it does not have a specific pattern. Based on this assumption, one strategy to get rid of it is to gather large amounts of data. As the deviations from the real value are equally distributed in positive and negative directions, adding sufficient data to the calculations will lower the noise to a tolerable threshold, and theoretically if infinite number of measurements are made, the limit of the noise goes to zero. It should be noted that it is not possible to increase recording frequency beyond a limit due to technical and processing limitations, therefore a frequency that will balance the work load and error minimization is used.

Before applying the technique to the results of the experiments conducted and the analysis results of the finite element models constructed, it is tested on a simple beam modeled with a line element only. In Figure 3.22, it is clearly seen that even for the case of a very simple beam, the 12 segment solution includes large variations in the calculated EI coefficient. The

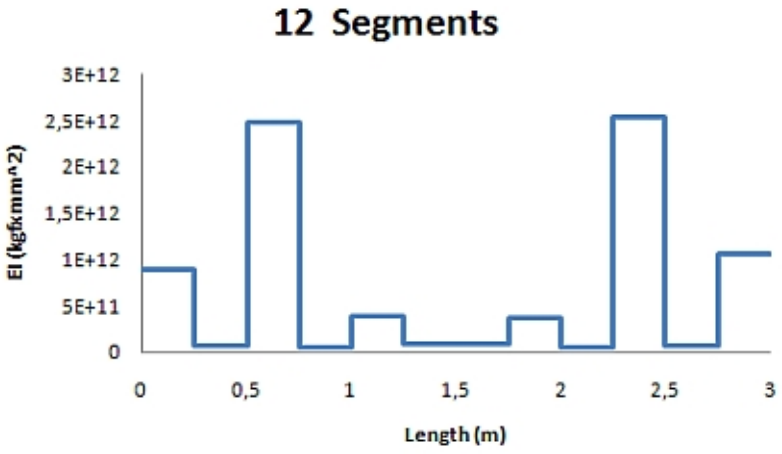

Figure 3.22: EI Coefficients Calculated from the Simple Beam (12 Segment)

solution obtained using 6 segments yields better results than 12 segments, however these results still show unwanted variations. If the total number of segments are further decreased, the accuracy and the stability of the method increases significantly (Figure 3.23). Thus, in processing the results, 4 or less segments are considered.

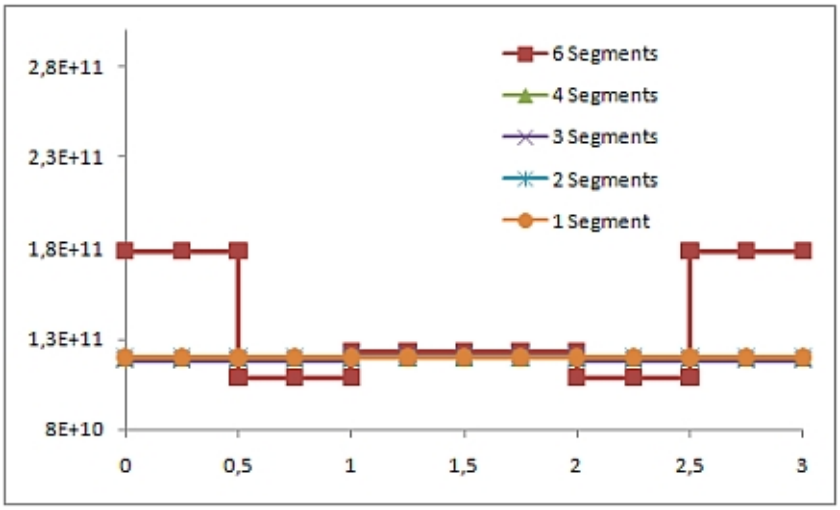

Figure 3.23: EI Coefficients Calculated from the Simple Beam

3.2.3.1 Test Setup

The sample beam was tested under static loads before and after it is damaged and these tests were conducted in the Structural Mechanics Laboratory of the Civil Engineering Department in METU. As the finite element models indicates that the beam is too rigid and maximum deflection under half a ton is around 3 mm, a load which is both heavy yet easy to move on the beam is required, and from capacity calculations the magnitude is determined as 600 kg. Since the unit weight of concrete is low, if the weight would be made of concrete, its dimensions would be unpractical. Therefore it was decided that the material should be either steel or cast iron. For the shape, at first rectangle was the idea, with wheels at three or four locations. However, this time load could not be applied from one point and it would not be uniform. Because of this, a cylindrical shape was selected since it is both easy to roll it on the beam and it applies force just from one line; its contact points. Knowing the density of steel/iron (which are close), and considering the maximum height of the cylinder (the width of the deck is 30 cm and there will be LVDTs around it, so the cylinder should not exceed 3-4 cm

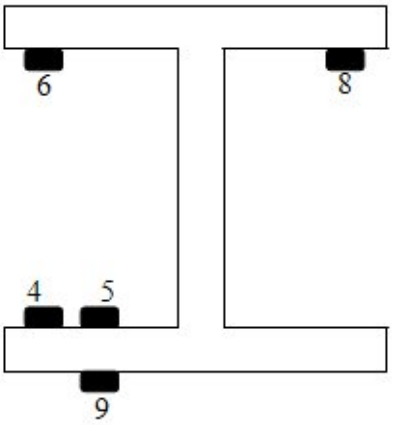

Figure 3.24: Strain Gage Distribution

from each side), the minimum required dimensions were computed. In all the calculations, the mathematical model of the beam is assumed to sit on simple supports. Therefore in the experiment setup one side of the beam was put on a rectangular rod (the pin side) and the other side was put on a cylindrical rod (the roller side).

For measuring the displacements and strains, linear variable displacement transducers, resistance type strain gages and vibrating wire strain gages were used. The vibrating wire and resistance strain gages were placed on the beam permanently during construction. There were seven resistance strain gages and three vibrating wire gages installed on the beam. Locations of the strain gages can be seen in Figure 3.24. The resistance gages were connected directly to the data acquisition system (DAS) available in the laboratory, which can read individual gages without a need for Wheatstone bridge. The vibrating wire gages (VW), however, cannot be connected directly to a DAS because there is the need of an additional hardware connected between the gage and DAS. This is simply because the VW gages return vibration frequency as measurement and this frequency should be determined by comparing it to a set of values, and this comparison is done in the extra component. In the very first test, however, two of the seven resistance gages and all of the three vibrating wire gages were identified to be faulty and they are completely excluded from further experiments. Because of this, only five gages of resistance type were operational in all the experiment sets.The LVDTs were also read by the aforementioned DAS. A total of six displacement transducers were utilized during all the experiments, coupled as pairs along the width of the beam in three locations; dividing the beam into four equal pieces longitudinally (i.e. at 75 cm, 150 cm, and 225 cm) (Figure 3.25).

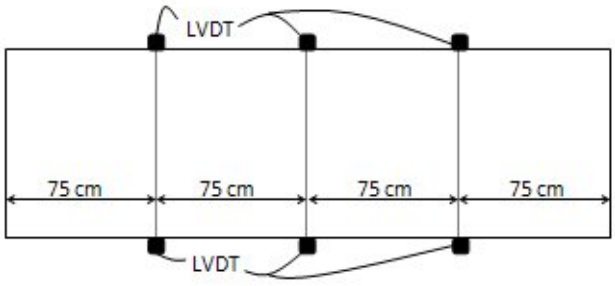

Figure 3.25: LVDT Distribution

Pairing the LVDTs into three groups as shown has a very fundamental reason; unsymmetrical loading possibility. The finish of the deck was not completely flat and quite rough. In addition, there were no leading central line for the movement of the load along the deck center. These two conditions might result in incomplete touch surface (due to ragged surface) or skew loading, which will cause unsymmetrical displacement profile along the width. If the displacement is measured from just one location, results may be defective or misleading. In order to overcome these problems, deflections were measured from the two ends of the concrete deck and numerically averaged. The roughened surface poses other concerns to be solved; such as disturbing the readings of LVDTs. Considering that the surface under the deck is far more rough than the upper surface, the possibility of an LVDT rod to rest on an aggregate crest and slip during an experiment is high. Such occurrences will surely cause high errors that cannot be reduced computationally, thus must be avoided during experimentation process. The proposed solution was to mount small glass rectangular pieces under measurement locations, hence form a completely flat and glazed surface. Some of the important points here is, first of all, the effect of the glue. Silicone based adhesives may deform itself axially under loading, thus reduce the measured displacements; therefore harder adhesives should be used. Secondly, if too long glass parts are glued, excessive strains may cause breaking of the glass, thus shorter rectangles are mounted.

3.2.3.2 Testing Procedure

The displacement pattern required for processing the data in the intended way is moving the load from one end to the other, stopping at the predefined intervals. The theory necessitates measuring displacements from the 11 stations while loading from three points, which is not

feasible to execute. Therefore, based on the reciprocity property of Betty's law, the load was applied from 11 points and displacements were recorded from three stations. The beam was divided into 12 equal segments, each having a length of 25 cm, and the segment borders were drawn on the lab beam's deck by chalk. Reading frequency was selected from values of 10 Hz and 20 Hz in each test such that around 600 data is accumulated per segment. Before beginning the loading part, a walking test was performed on the test beam where the target parameter was the strain. The walking test was performed unidirectional; movement is from the beginning to the end only. The person walking on the beam waited on the segment borders for a predefined duration, and the walking process was repeated for several times. In this way, the response could be compared directly, without rigorous post-processing.

The main static loading event was executed by moving the cylindrical load on the beam. All the gages were calibrated and scaled by the automated data acquisition system, and recording of the data was started before the load was put onto the first location with the help of a crane. After the load rested on the beam, the crane was detached to prevent it from interfering the sensitive displacement gages. Load was tried to be centered on the beam in both axes as accurately as possible, and two L50x5 wedges were used in front of and behind of the cylinder to prevent unwanted movements during measurements were taken. After gathering enough data at one position, the load was pushed manually to the next stop position. As the load came to the end of the beam in one direction, it was pushed backwards instead of lifting it up again by crane and transporting to the beginning spot, to save time and check linearity of the system. The reverse direction measurement values needed to be reversed before comparing them with the forward passes. Two to three pairs of loading cycles were done at each test. In processing, the displacements measured while the load stays stationary were used; however, the acquisition system cannot be paused during a recording session, thus the whole experiment was recorded as a single file having continuous data flow.

3.2.3.3 Performing Reference Tests

The initial test performed on undamaged beam differs from the other experiments done, because it was the first one; few were known on how the process would flow and how the results would be. Many of the items listed in the Section 3.2.3.2 were missing; DAS was adjusted to take 100 readings at each second (100 Hz reading frequency), there were no glass layers

on top of LVDT rods, only one forward pass is done, the load was put onto the start position with a crane then the measurements have begun. Because of this, all the other displacement measurements were taken with respect to this first loaded position. In order to overcome this mistake, the first displacement values are subtracted from the rest, which caused some problems mentioned below. Only one pass was done from one side to other. Only three LVDTs were used; one at the center of the beam and one at 75 cm away from both ends. These displacement transducers were connected to the sides of the concrete deck. All seven resistance strain gages were connected, in addition, the VW gages were on-line.

Considering the quite poor results of the first experiment, the second experiment was planned thoroughly, and all improvements in Section 3.2.3.2 are applied. The test was again done on the undamaged beam (Figure B.2) and the resultant displacement values can bee seen in Figure 3.26.

3.2.3.4 Processing Test Data, Extraction of Structural Parameters

The advantage of standardizing the experiment process manifests itself in the processing phase; the calculations can be systematized, too and the results of the different experiments will be more coherent. The raw data taken from an experiment is an MS Excel file consisting of the readings of the transducers as a time - value pair. Though the number of data taken while load is stationary is fixed, total number of data varies between experiments, due to the fact that recording is continuous. As a general average, however, data taken is usually in the range of 100 000 to 150 000 per experiment.

The strain data recorded after each damage level is plotted together to see whether any change occurs in the strain profile at that cross section. In addition, strain data is used to check the results obtained on the shear transfer level computations. The displacement data from the three LVDT pairs (averaged by two) is plotted as a whole at first to determine time windows where the load stays static, and the other portions are discarded. Then the values falling into the windows defined are extracted and the necessary 11 displacement values are computed by averaging; thus the reduction of the data is completed. If any outliers (i.e. a displacement profile considerably different than the rest), are observed, however, that series is excluded from future calculations due to the assumption that some kind of error is involved (experimental or any other source). Then the obtained load vector is used as the reference matrix

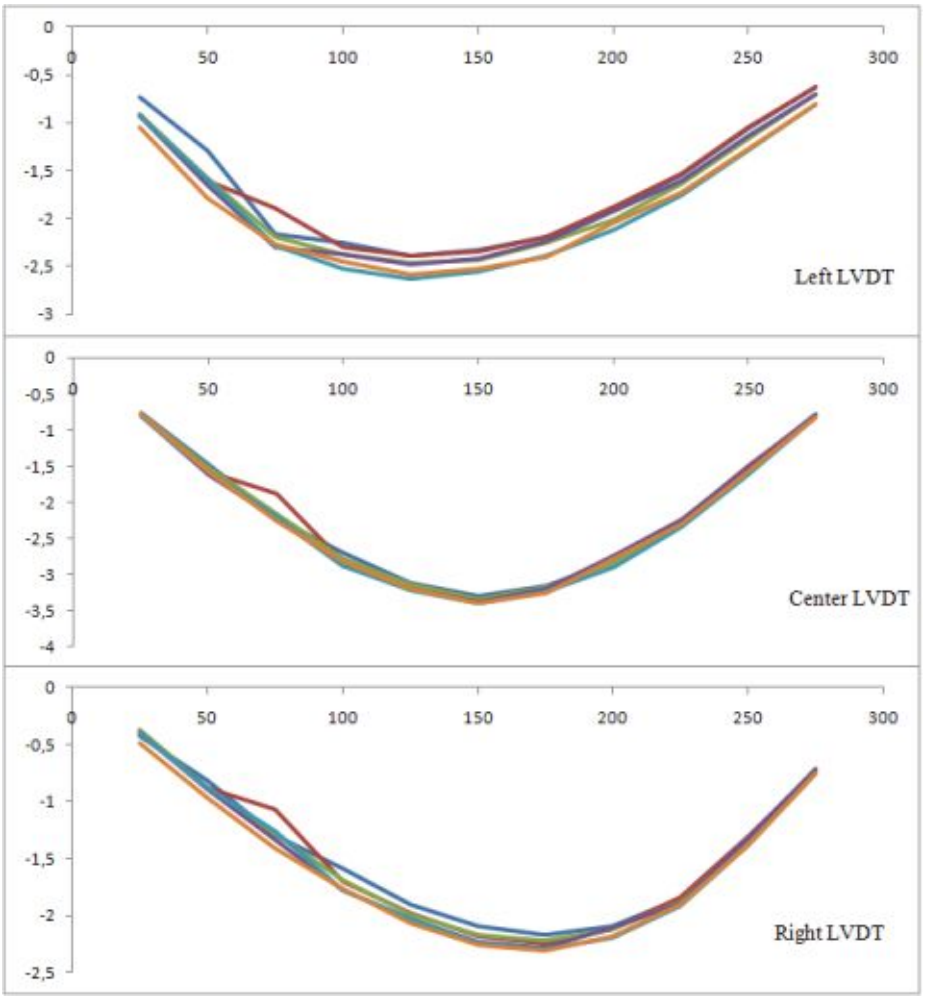

Figure 3.26: Displacements of Second Experiment

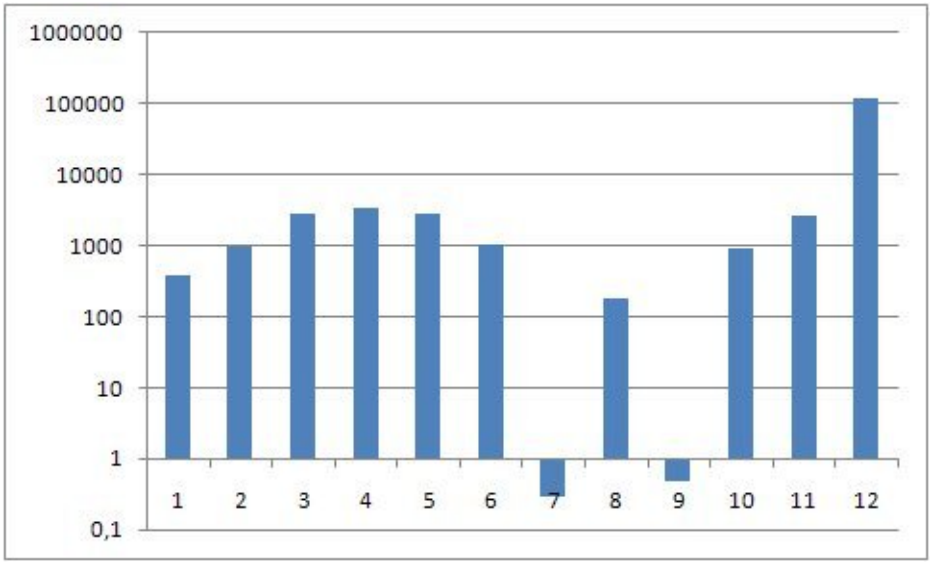

Figure 3.27: EI values obtained from the first experiment data

to find the displacements where EI of the mathematical model is tried to be found by calibration. The calibration process is done for each and every pass; forwards and corrected backwards. In calculating the EI values, different segment lengths were used to see how the degree of segmenting affects the results. First, 12 segments were used; in other words, the number of unknowns (EI of each portion) was equal to the number of equations (measured displacements), there was no redundancy. Then, the number of portions was reduced to six, four, three, two, and one; each having more and more extra data to remove the effects of uncertainties and measurement errors. Having more reference data points then the unknown EI coefficients is referred as "redundancy" in the context of this study.

The very first experiment was not very successful due to the lack of improvements suggested, thus the obtained EI values are not consistent (Figure 3.27). There are negative EI values, which are physically impossible, and the reason is the inconsistent displacement data; if there is negative curvature measured in the system, then the processing will clearly lead to inverse stiffness.

In the second experiment, however, the results are considerably better, which leads to stable and coherent EI values. The results of the 12 segment solution is given in 3.28 and clearly indicate that having no redundant input to reduce the effects of external disturbances will cause excessive deviations in the calculated sectional stiffness. In order to determine whether

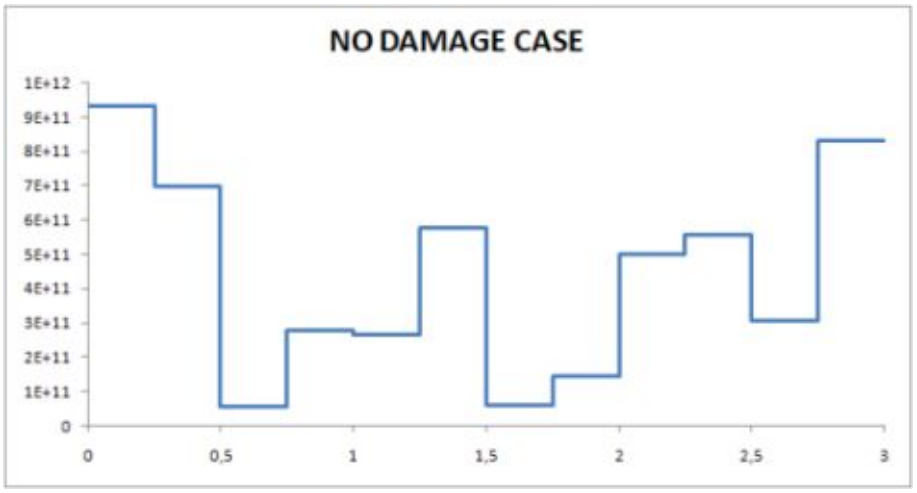

Figure 3.28: EI values for 12 segment solution

halving the number of segments, thus rendering half of the points as redundant data locations will help to improve the stability of the system, segment length is doubled (50 cm), and necessary values are re-calculated (Figure 3.29). The results seemed to be improved, but still not stable enough to make a robust system identification or damage detection. Realizing that increasing the level of redundancy (i.e. reducing the number of segments which EI is calculated while keeping the number of measurement nodes) will lead to more successive and reliable results, further reductions in segment count is done; the previously stated procedure is re-applied considering four divisions, three divisions, two divisions, and finally considering the whole beam having single EI. The values obtained can be seen through Figure 3.30 to Figure 3.33. One of the points that is reflected in the graphs given is that the start of the beam has lower stiffness than the rest, which is confirmed in all the cases where division count is less than six. This declination in the stiffness may be the manifesting result of a previous damage, extended loss of composite action in that zone, or attenuation in the thickness of the concrete.

If the computed EI value (from the test) is compared with the analytical calculations of the EI with full and no shear transfer (Equation 3.9 and Equation 3.11), it can be concluded that the composite action percentage of the beam is very low; but not completely absent. Considering the linear relation between the beam EI and link shear force, and realizing link shear force changes between 0.14 t and 0 t, the composite action percentage can be estimated as around 8%. Since the level of the shear transfer between the concrete deck and the steel girders is

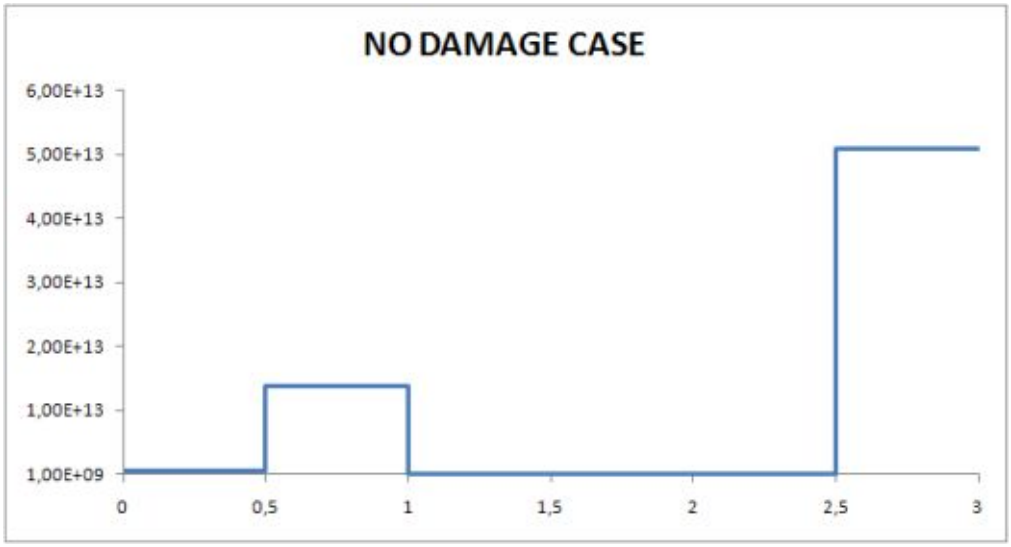

Figure 3.29: EI values for 6 segment solution

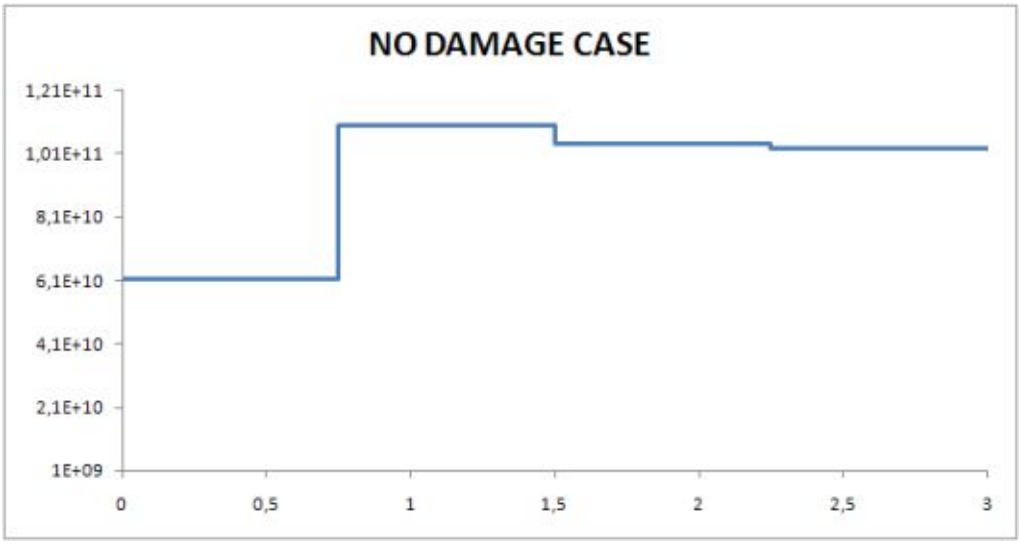

Figure 3.30: EI values for 4 segment solution

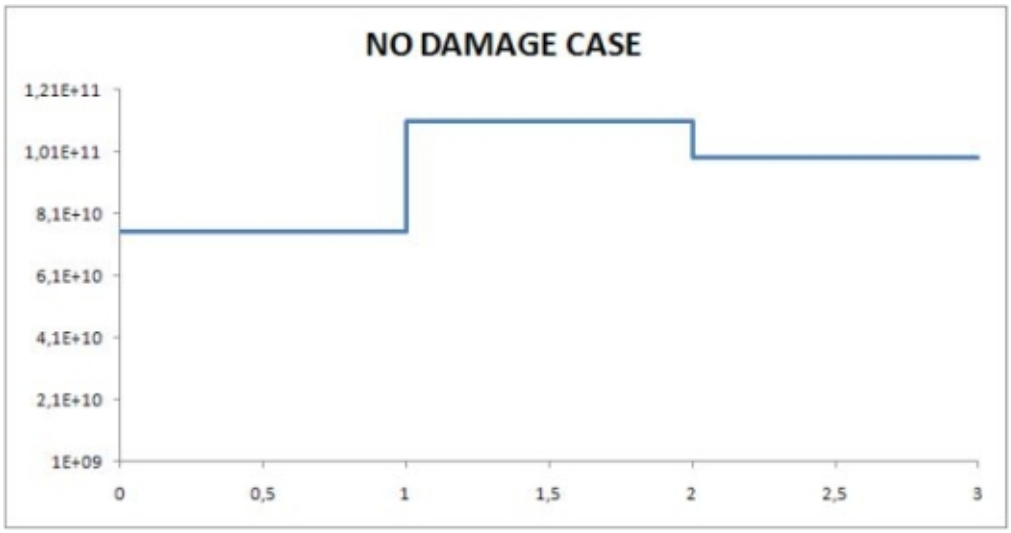

Figure 3.31: EI values for 3 segment solution

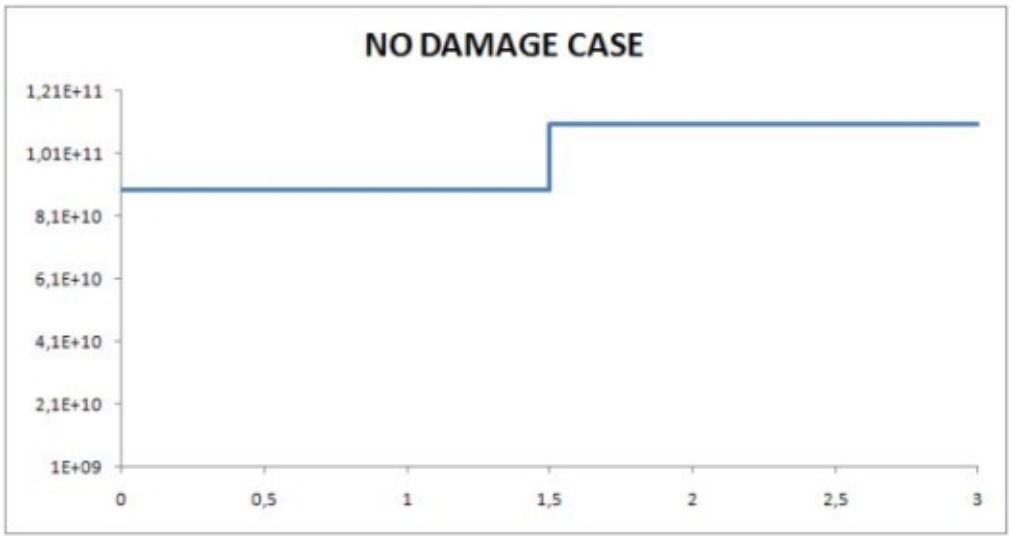

Figure 3.32: EI values for 2 segment solution

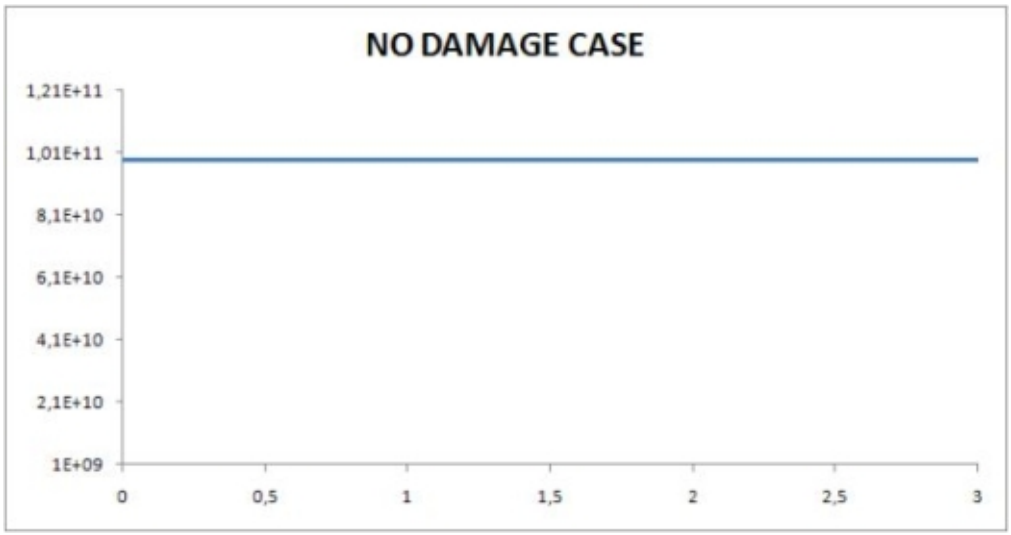

Figure 3.33: EI values for 1 segment solution

found to be little (i.e. both components are behaving nearly independently), the strains in the upper and lower flanges of a steel girder should be close to each other (if the composite action was found to be diminished completely, the strains had to be equal, due to the fact that the I100 section will bend around its own centroid, not the composite section's). This relation could be used to verify this conclusion on composite action level, confirming the validity of the approach used. During this test, these gages were connected to a data acquisition system, and 20 data per second is selected as the reading frequency.For the loading pattern, a man walked on the beam from one end to other in one direction only. This pattern was repeated for several times, and the results obtained from the strain gages are given in Figure 3.34. In the Figure 3.34, it can be clearly identified that the fourth channel is not reading reasonable values, indicating that gage has malfunctioned. The fifth and sixth gages, however, recorded the required data quite well, and include clues on the composite action level of the whole system (Figure 3.35). The two strain measurements, though close, are not equal and there is a certain amount of shift, which indicates that the composite action still exists in the structure.

3.2.4 Damage Scenarios and Tests

Damage conditions on the beam are simulated by cutting the steel girders from one or several locations in different amounts (Figure 3.36). First of all, after experiments on undamaged beam are completed, half of the tension flanges of the both steel girders at 125 cm from one

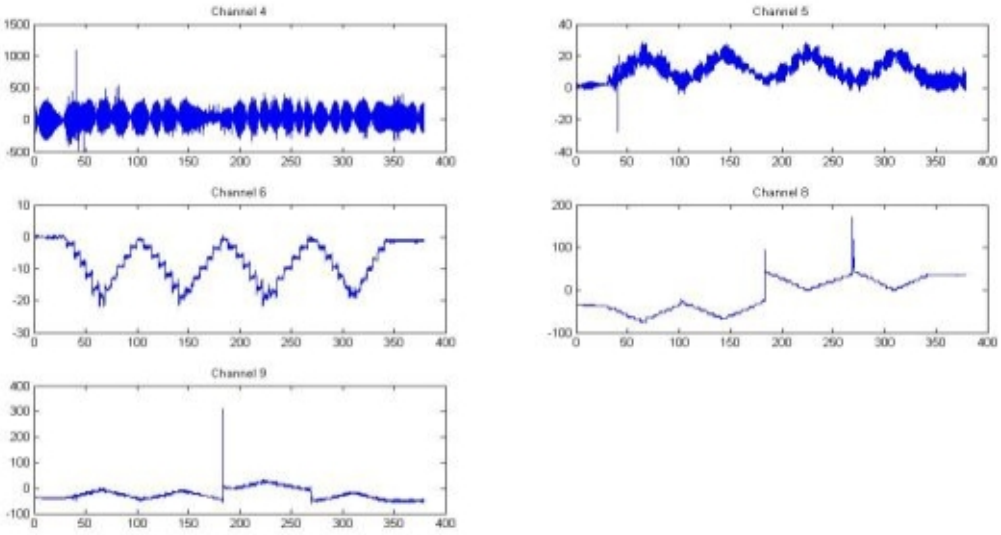

Figure 3.34: Readings of the strain gages during 4 cycles of walking

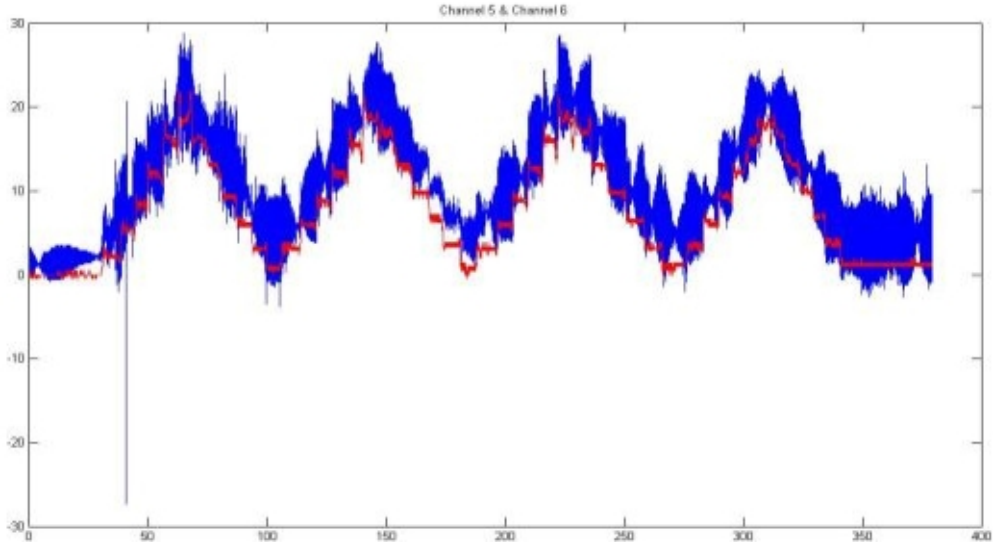

Figure 3.35: Outputs of the strain gages 5 and 6

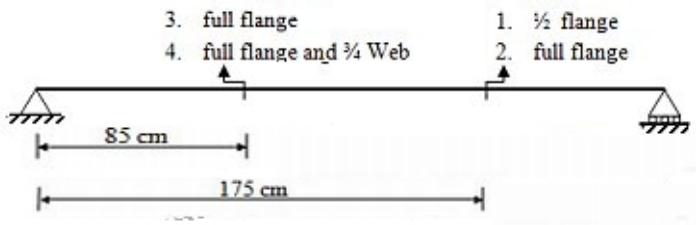

Figure 3.36: Damage Distribution and Sequence

end (opposite of the starting side) was cut (step 1 in Figure 3.36). The reason for selecting this place is, first of all, it is not directly under the measurement locations (LVDTs) and strain gages. Secondly, the location of the point does not coincide with the cross-bars under the beam that are used to increase its transverse stiffness. Third, the cut location is not in the connection points of the subsections created during processing of the data (i.e. the locus of the damage is always inside segment boundaries). Cutting only half of the tension flanges is to make the damage intensity stepwise; intensity of damage is increased only after necessary experiments are done on the previous damage level. As the second damage level, the half-flange cut existing on the beam was extended to full flange; thus further portion of the section is rendered useless under bending actions (step 2 in Figure 3.36). In addition, in order to see if the proposed method works for damage located in scattered places, another full flange cut is done in a different location, at 85 cm from the starting side. The reasons for selecting this point is similar to the reasons of previous location choosing; it does not coincide with any transducer, any cross-bars and segment boundary. (step 3 in Figure 3.36). As the final step, the damage on the starting side is broadened to the two thirds of the web, causing extreme damage. The reason behind is to see how the system and the proposed method will behave in case of an extensive damage (step 4 in Figure 3.36).

3.2.4.1 First Damage Level (One Location Half Flange Cut)

In the first damage level, only half of the tension flanges of both steel girders were cut (step one in Figure 3.36). The test was performed as explained in Section 3.2.3.2 with one exception; instead of three pairs of passes, only two pairs could be executed in the third test due to technical conditions and laboratory limitations. The resultant displacement graphs are given in Figure 3.37, where it can be seen that the left LVDT has an outlier series, which is to be expelled from computations. The displacements measured after damage are almost identical to the reference measurements (Figure 3.38), the maximum effective changes are in the range of 2% to 4%. The minority of the increase in displacements after damage has roots in the facts that; first the test specimen is too rigid, and has a thick concrete deck part (undamaged) that reduces the effects of the cut, and second, the damage is not extensive. As previously stated, the 12 and 6 segment solutions are far too devious and complex to draw conclusions; therefore the results of this test is compared with the four, three, two, and one segment solutions of the reference test. The four segment solution comparison can be seen in Figure

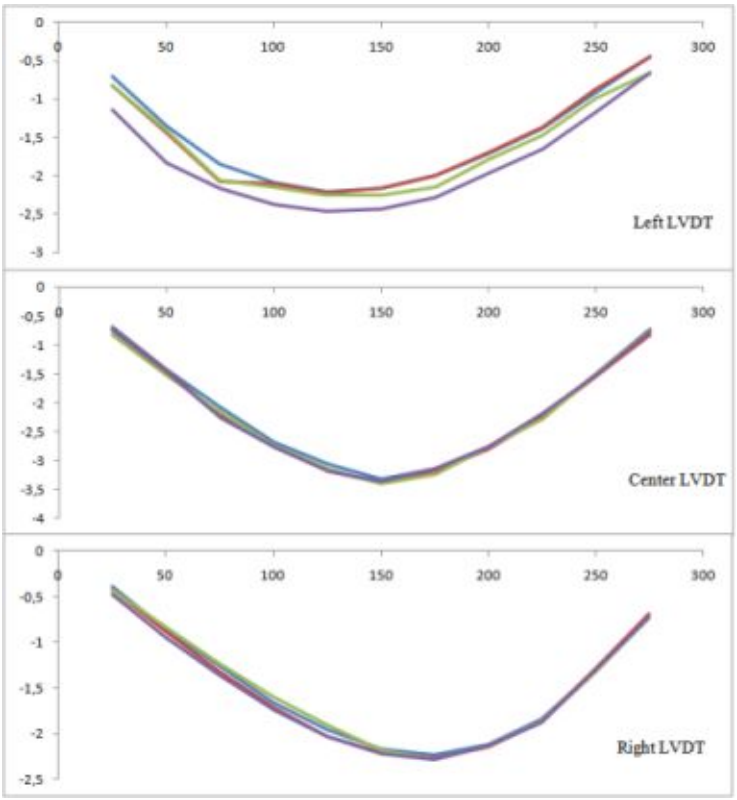

Figure 3.37: Displacement Profiles for the First Damage Level

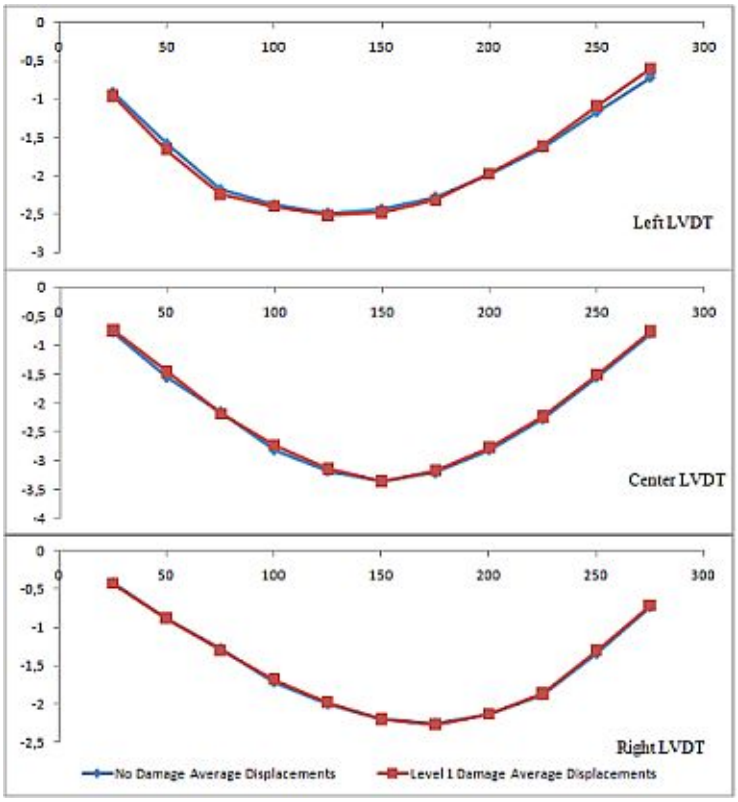

Figure 3.38: Comparing Displacements of Reference and Level 1 Damage Cases

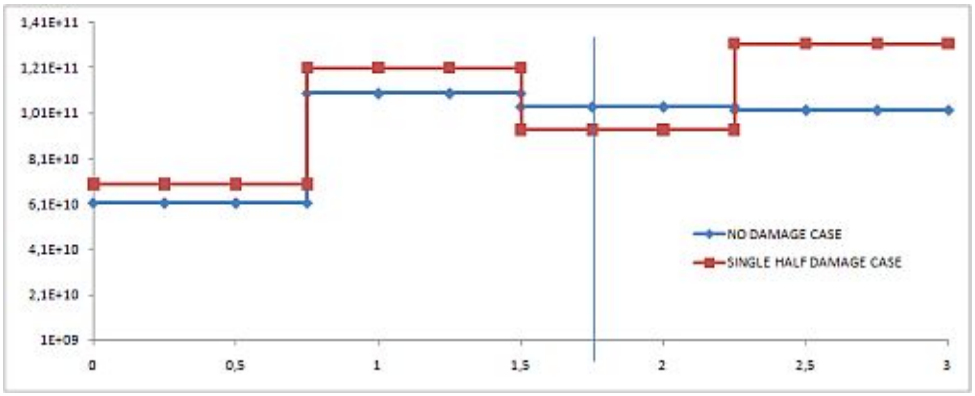

Figure 3.39: 4 Segments Solutions of Reference Test and First Damage Level

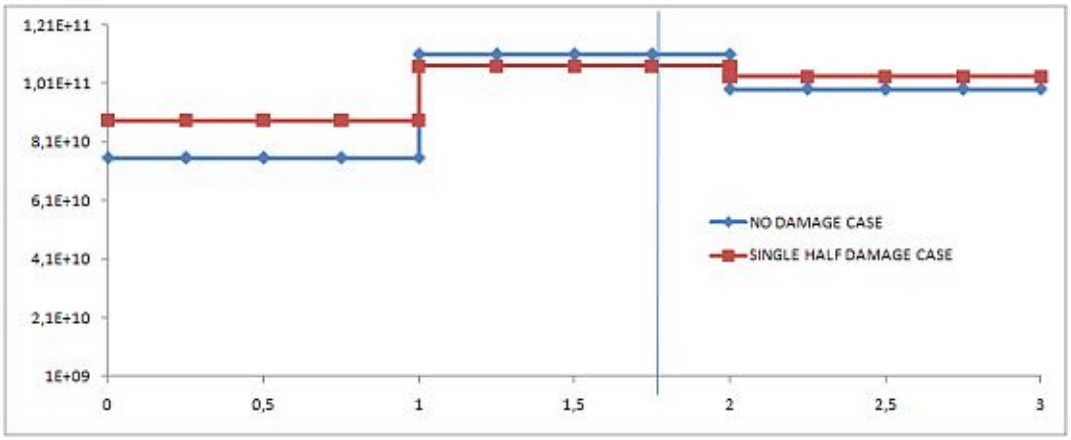

Figure 3.40: 3 Segments Solutions of Reference Test and First Damage Level

3.39. The vertical line in the graph is the location of the damage. A decrease in EI value of the segment containing the damage point can be observed; however there are increases in all other segments present; this illogical result is accepted as the indirect consequence of the high stiffness of the beam. The increase in displacements, as stated, is in the range of 2% to 4%, around the measurement resolution of the transducers, especially when the load was close to supports. Three segment solution also shows the same characteristics (Figure 3.40); the damaged sector has lower EI whereas the other subdivisions has higher. For two and one section solutions, the damage and increase in displacements is so low compared to the overall test beam, the drops in EI values are almost unidentifiable (Figure 3.41and Figure 3.42).

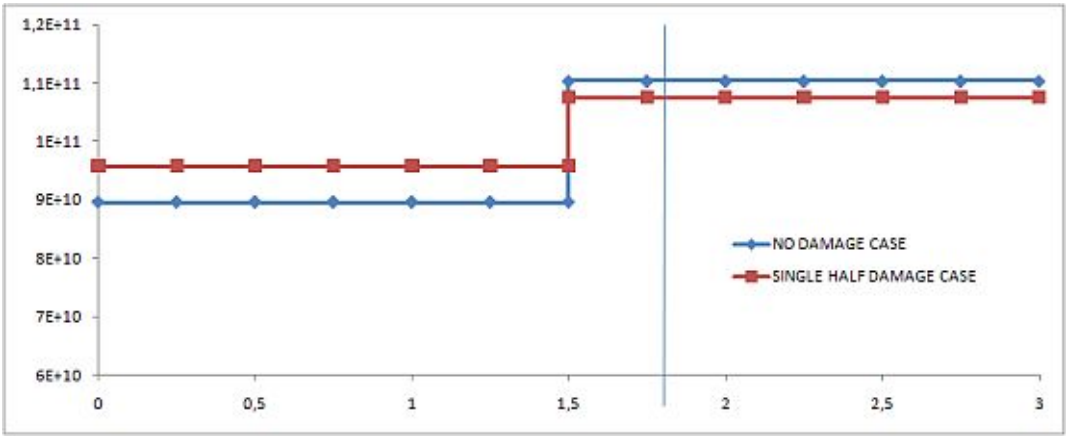

Figure 3.41: 2 Segments Solutions of Reference Test and First Damage Level

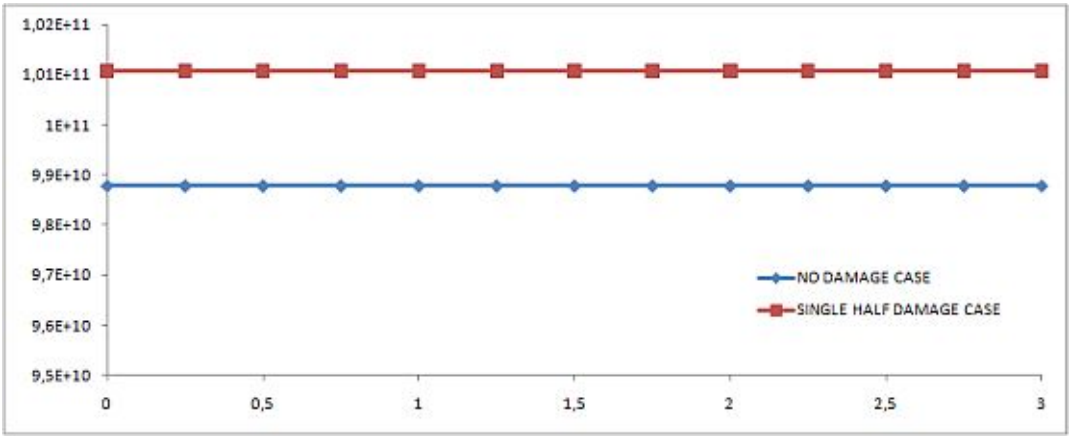

Figure 3.42: 1 Segment Solutions of Reference Test and First Damage Level

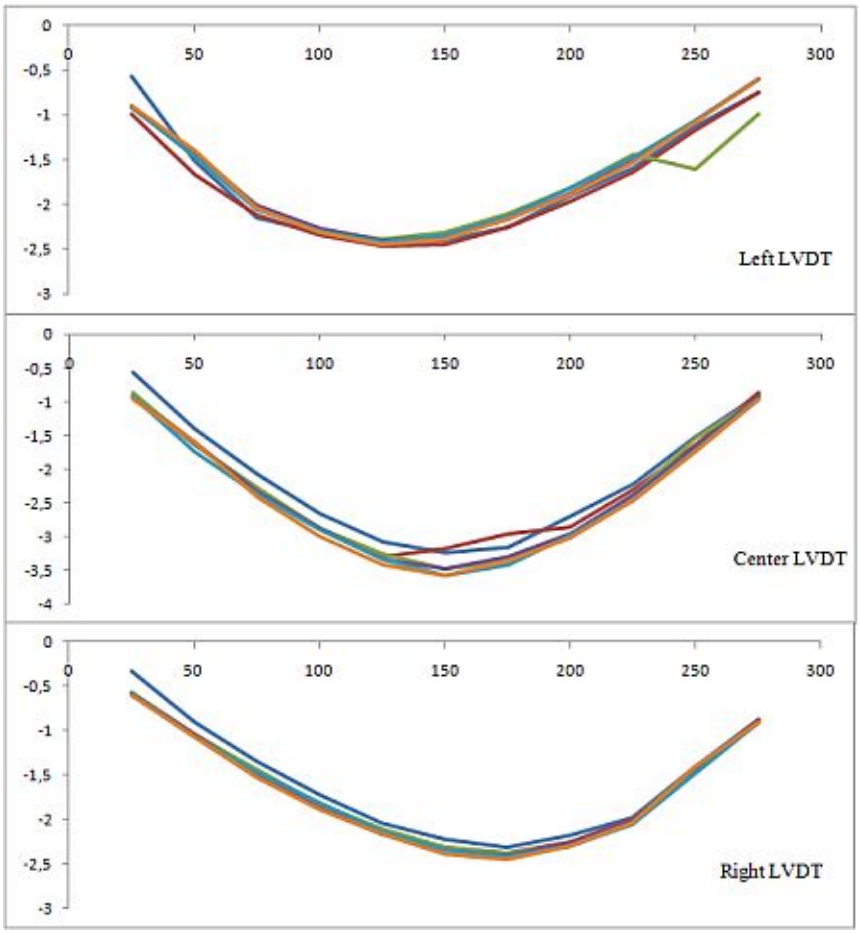

Figure 3.43: Displacement Profiles for the Second Damage Level

3.2.4.2 Second Damage Level (One Location Full Flange Cut)

In the second damage level, half length cut in the tension flanges of steel girders was extended to full flange (step two in 3.36) (Figure B.3). The flow of the test was exactly as explained in Section 3.2.3.2(Figure B.4), and the resultant displacements for all six passes could be seen in Figure 3.43. The increase in the displacements is better than the case in first damage level, but still in the range of 5% to 10%, and close to the limits of the measurements (Figure 3.44). As the damage and deflection intensity increases, the drops in the EI values become more evident, as the four segment solution indicates (Figure 3.45). The decrease in EI, however, manifests itself not on the damaged segment, but on the next one. This is also evident in the three segment solution, as seen in Figure 3.46. Two segment solution, represents the damage level better, showing the lowering in the second portion clearly (Figure 3.47). In single segment solution, the damage is also discernible by the change of EI. (Figure 3.48).

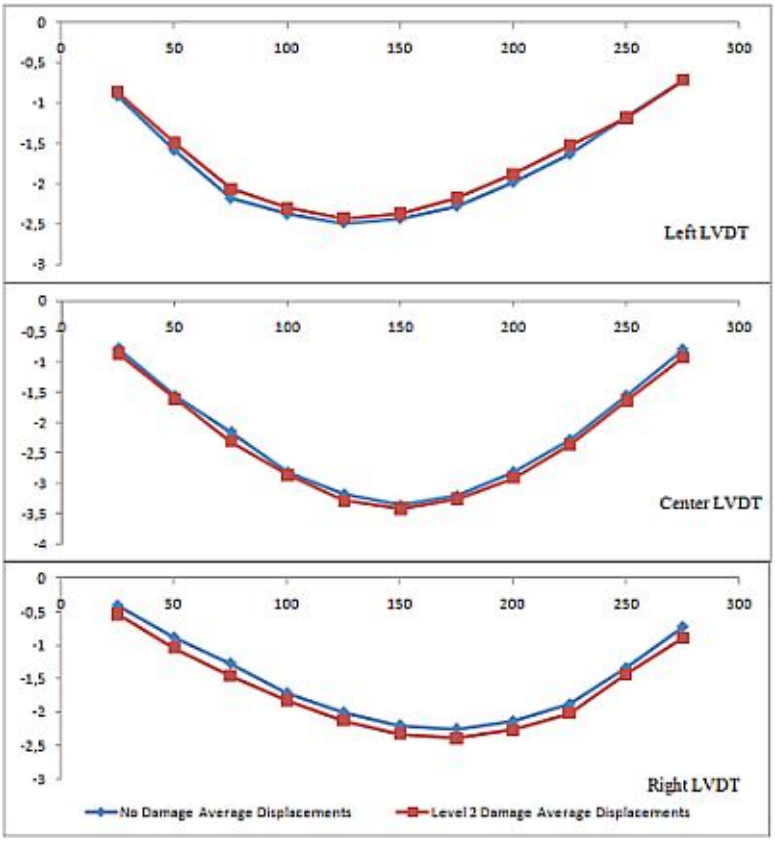

Figure 3.44: Comparing Displacements of Reference and Level 2 Damage Cases

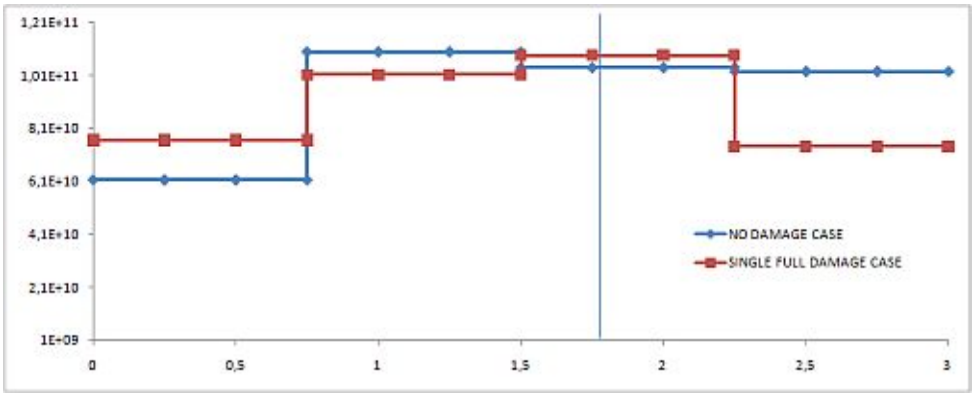

Figure 3.45: 4 Segments Solutions of Reference Test and Second Damage Level

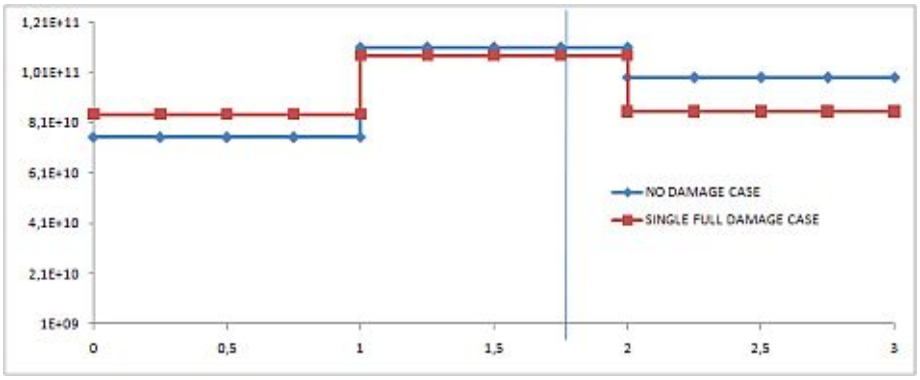

Figure 3.46: 3 Segments Solutions of Reference Test and Second Damage Level

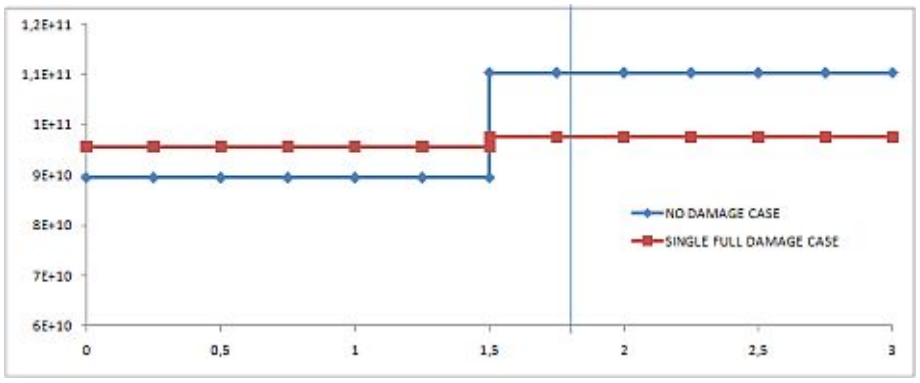

Figure 3.47: 2 Segments Solutions of Reference Test and Second Damage Level

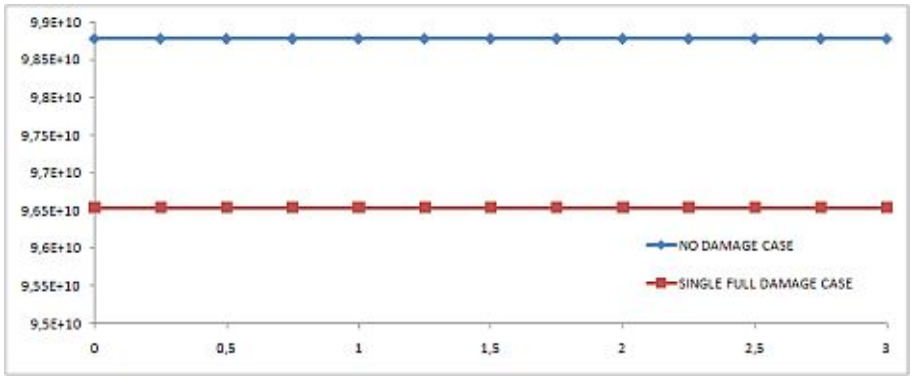

Figure 3.48: 1 Segment Solutions of Reference Test and Second Damage Level

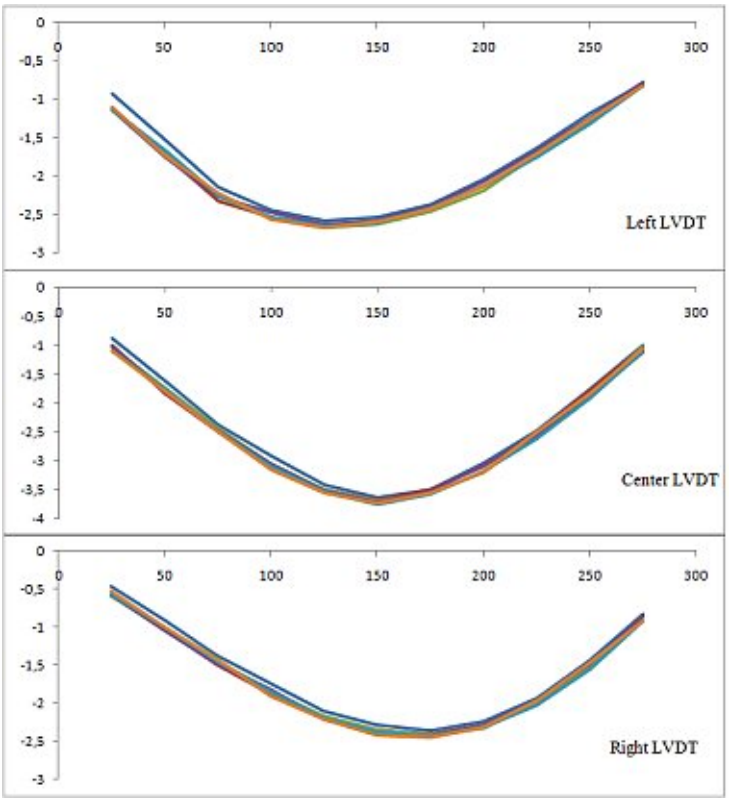

Figure 3.49: Displacement Profiles for the Third Damage Level

3.2.4.3 Third Damage Level (Two Locations Full Flange Cut)

In the third damage level, tension flanges of the both girders were cut totally in another location (step three in 3.36) (Figure B.5). The displacements obtained from three LVDTs in six passes can be seen in Figure 3.49. The increase in displacement fields is more obvious, and in the range of 10% to 20% (Figure 3.50). Both of the damages are identifiable in the four segment solution given in Figure 3.51, which also gives information on damage intensity. The vertical lines show the damage locations and the decrease in both segments are identical, as the damage condition. Therefore, it can be concluded that the change in calculated EI is proportional with the damage. The damages are also visible in three segment case, however due to the segment division pattern, the locations and intensities of damages are harder to estimate (Figure 3.52). The results are similar in two segments also; an existing damage is apparent from the EI graph given in Figure 3.53, however the portion showing the possible location of an existing damage is broader due to the low number of segments. One segment solution shows the large decrease in sectional stiffness in the overall system, as expected (Figure 3.54).

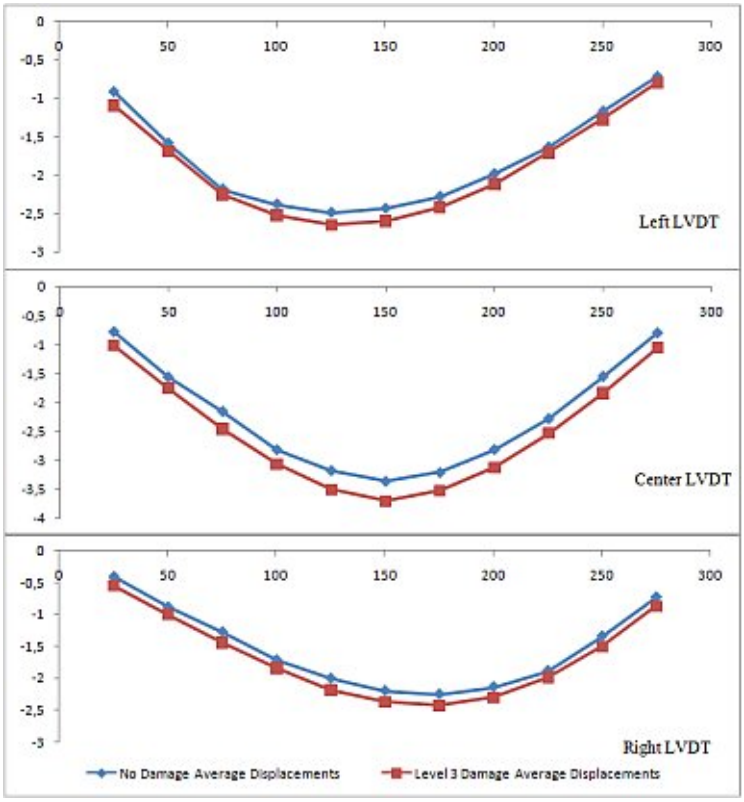

Figure 3.50: Comparing Displacements of Reference and Level 3 Damage Cases

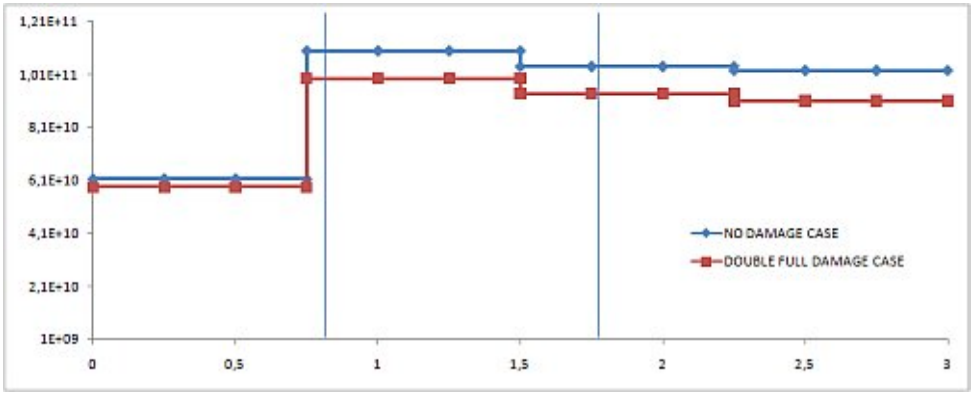

Figure 3.51: 4 Segments Solutions of Reference Test and Third Damage Level

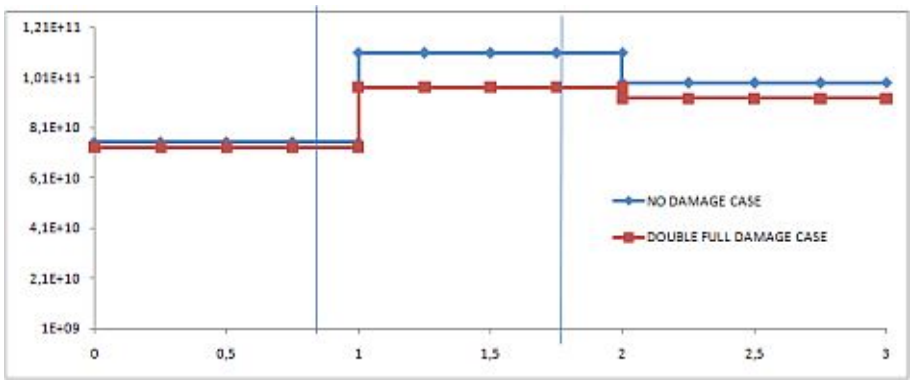

Figure 3.52: 3 Segments Solutions of Reference Test and Third Damage Level

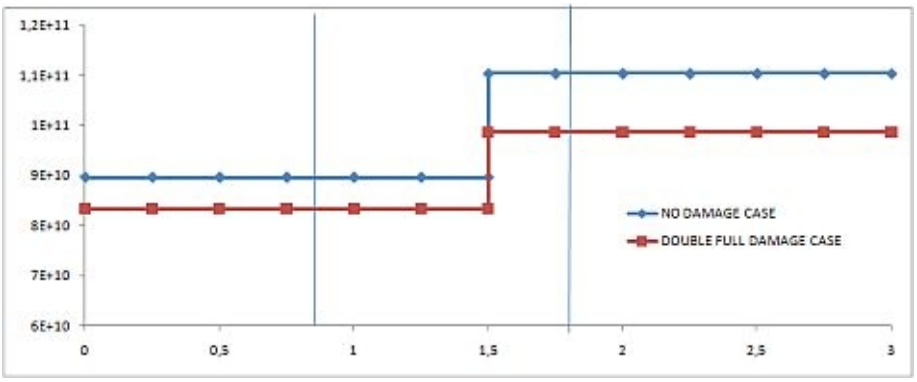

Figure 3.53: 2 Segments Solutions of Reference Test and Third Damage Level

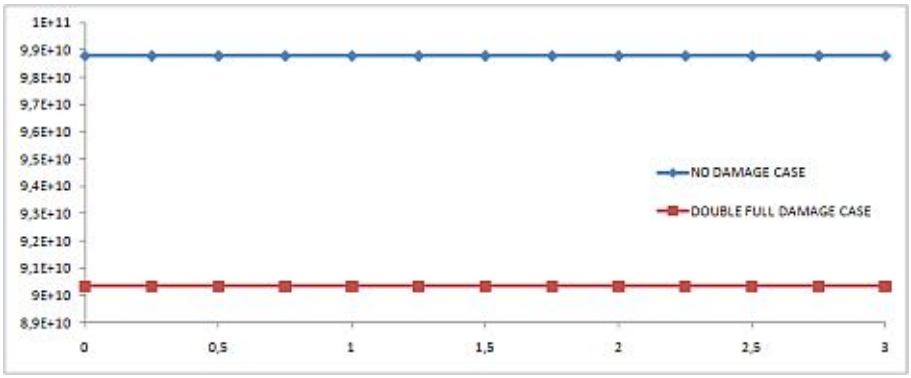

Figure 3.54: 1 Segment Solutions of Reference Test and Third Damage Level

3.2.4.4 Fourth Damage Level (Third Level and 2/3 Web Cut)

The fourth damage level was the maximum damage implied to the system to see how the composite beam and the proposed method behaves under extreme cases. In addition to the previous damage state where tension flanges of steel girders were cut completely in two locations, one of these flange cuts was extended to two thirds of the web (6.6 cm of the total 10 cm), which is the fourth step in Figure 3.36(Figure B.6). The reason for selecting the second flange cut location was its distance to the middle length of the beam where the maximum moment forces and displacements occur; it was not anticipated to have a failure during an experiment, therefore the maximum damage location was picked away from the maximum stress zone. Even though this precaution was taken, the displacements showed a tendency to increase with each pass, which could be an indication of damaging the system (Figure B.7); possibly yielding of the steel or cracking of concrete in one or several points (Figure 3.55). Considering the average displacements, the increase in displacement magnitudes are in the range of 50% to 90% (Figure 3.56), however if individual pass results are inspected, more than 100% increase can be seen, especially in the last passes. The trend of increasing magnitude and the overall scattering of the displacement vectors are expected to result in unwanted deviations in processing, and this outcome could be observed in four segment solution given in Figure 3.57. The results are better in three segment solution where the redundancy is higher and there are more extra data to correct the findings. The great decrease in the web damage location is visible, in addition to the softening at other places, which could be an

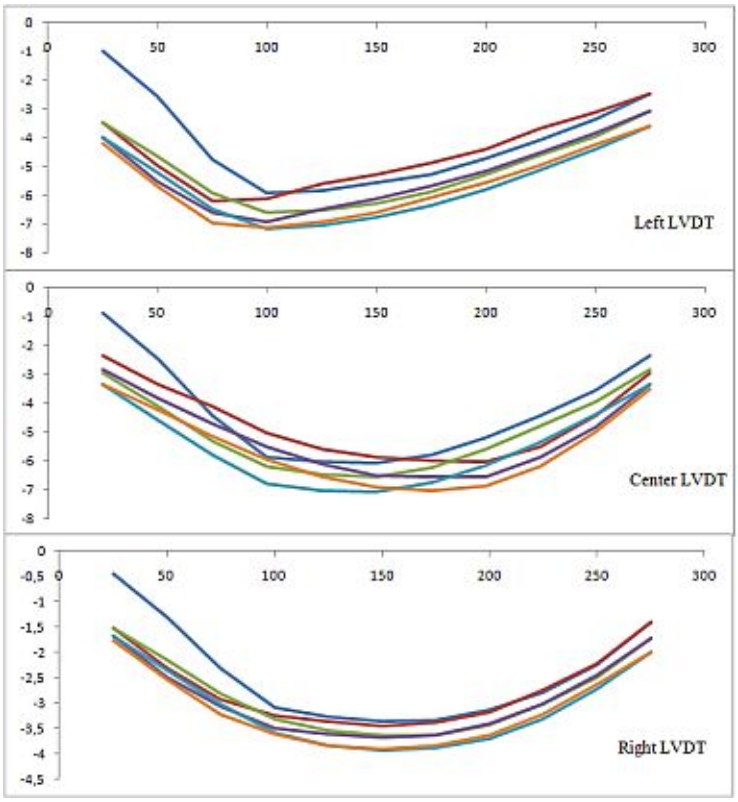

Figure 3.55: Displacement Profiles for the Fourth Damage Level

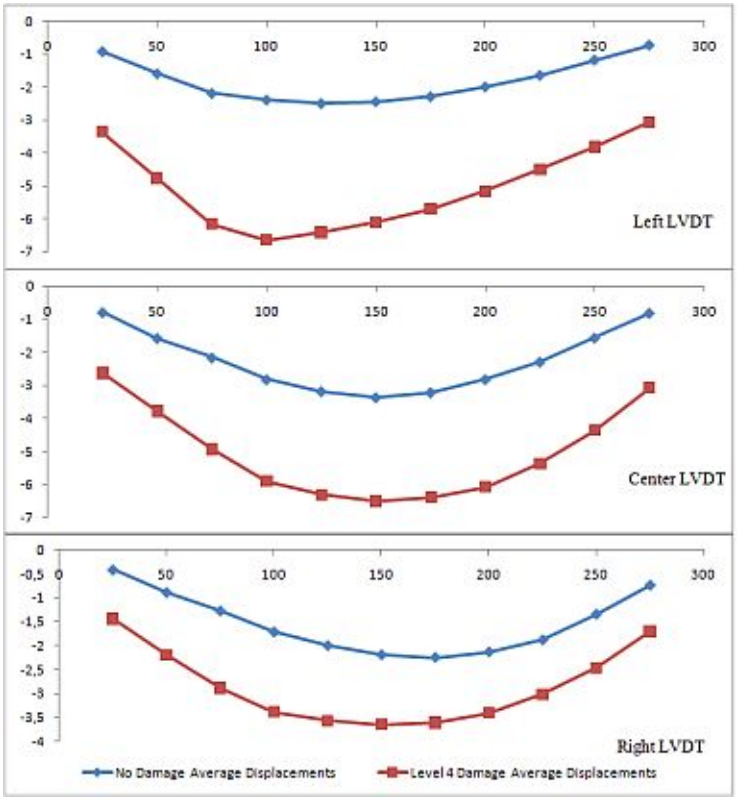

Figure 3.56: Comparing Displacements of Reference and Level 4 Damage Cases

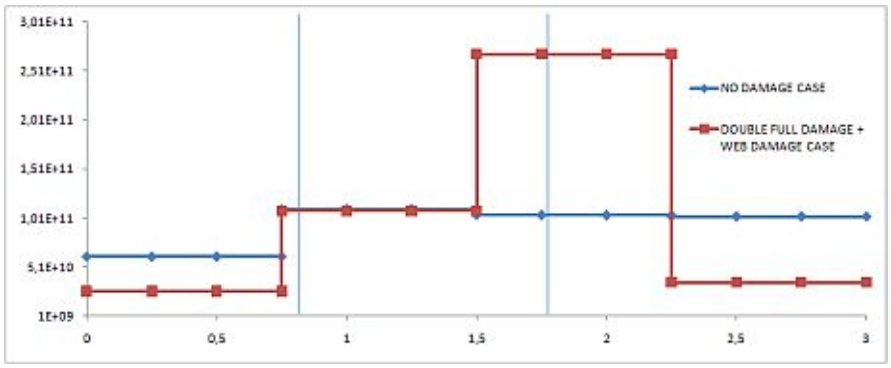

Figure 3.57: 4 Segments Solution of Reference Test and Fourth Damage Level

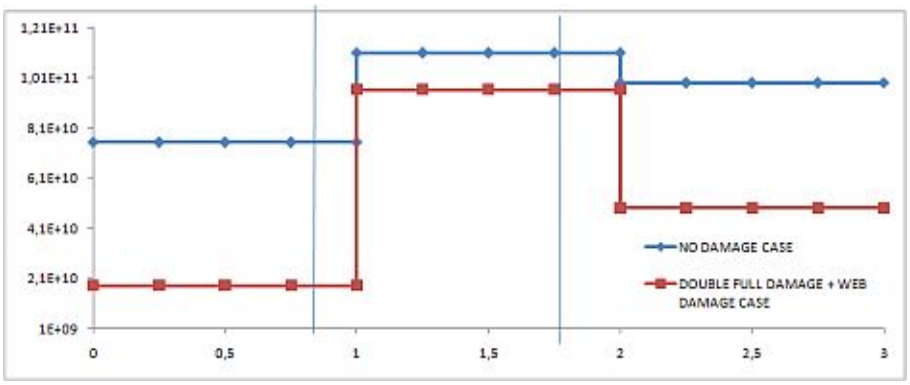

Figure 3.58: 3 Segments Solution of Reference Test and Fourth Damage Level

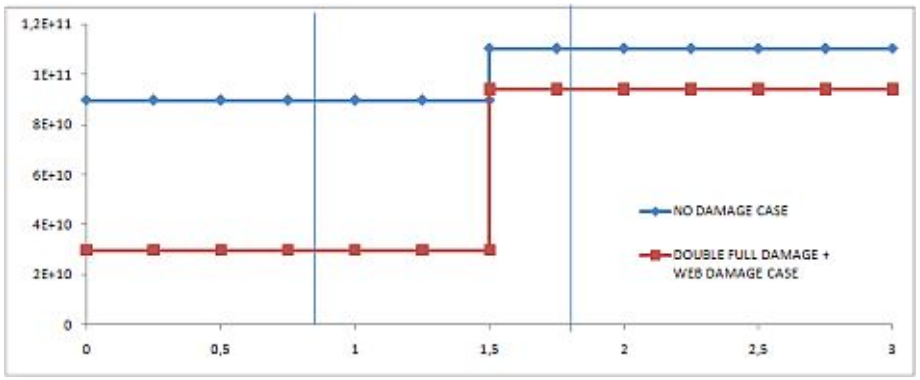

Figure 3.59: 2 Segments Solution of Reference Test and Fourth Damage Level

indication of further damaging the system during testing, or may be the radiating repercussion of the web cutting (Figure 3.58). This overall decrease in stiffness, though weaker, is still present in the two segments solution. However, the target damage is easily identifiable and can be stated that it is in the first segment (Figure 3.59). The large decrease in overall stiffness is also seen in one segment solution (Figure 3.60).

3.2.4.5 Comparing Analysis Results of Finite Element Model for Damage Scenarios

The loading pattern used in the static load tests is simulated in the finite element model with the help of the appropriate load cases, and displacement values are read from the nodes in the models at exactly the same locations where LVDTs were present in tests. Of all the three constructed, model number three, complete shell model is used due to its high versatility in changing the structural parameters (in other words, all the components like web, flanges,

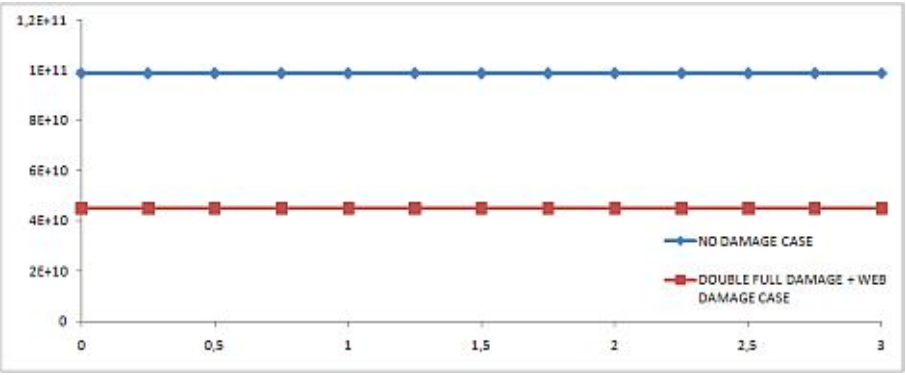

Figure 3.60: 1 Segment Solution of Reference Test and Fourth Damage Level

links, and deck of the specimen can be independently modified). Since the first part of the beam is not weak in the analytical model contrary to the real case, the drops in EI coefficients of the damaged segments are more prominent.

The results of the analysis of FEM for the four segment solution can be seen in Figure 3.61, and the effects of the damage can be identified as decreases in the calculated EI values.

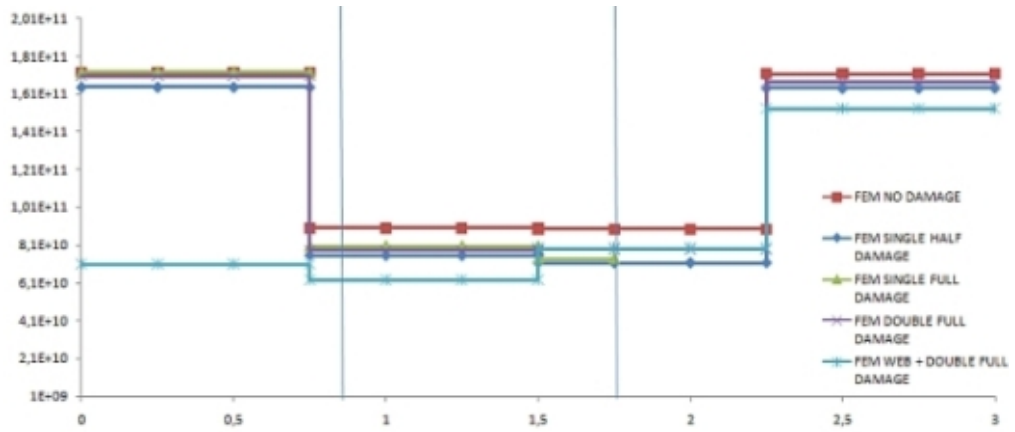

Figure 3.61: EI Coefficients Calculated From FEM Models (4 Segments)

The Figure 3.62 shows the solution done by utilizing three segments for the EI coefficient calculation.

Two segment solution of the FEM analysis results can be seen in Figure 3.63.

If only one segment is considered all along the beam, the EI coefficients calculated for different damage levels can be seen in Figure 3.64.

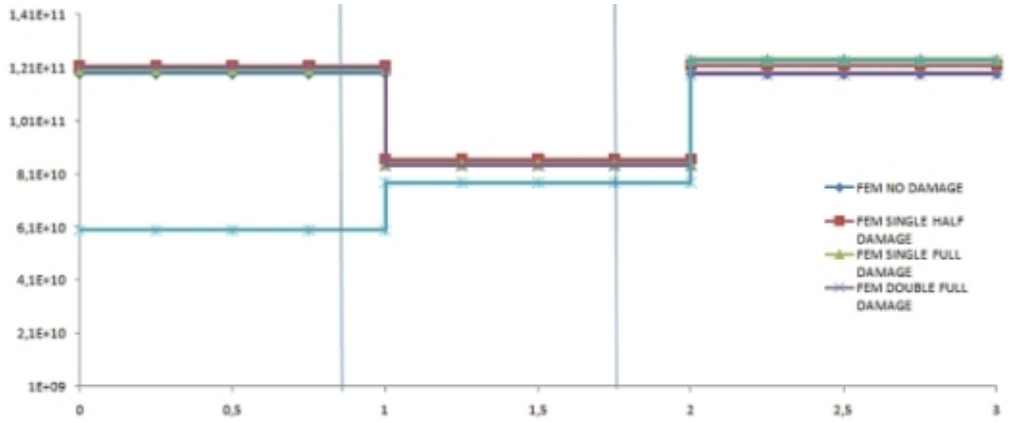

Figure 3.62: EI Coefficients Calculated From FEM Models (3 Segments)

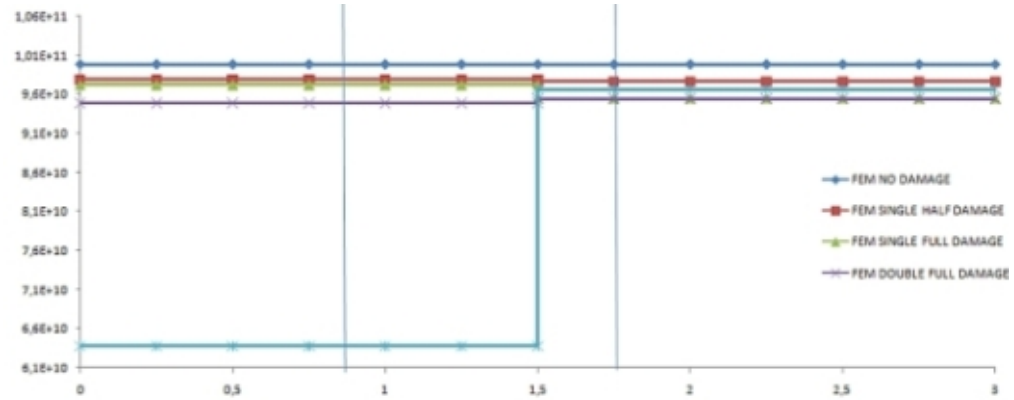

Figure 3.63: EI Coefficients Calculated From FEM Models (2 Segments)

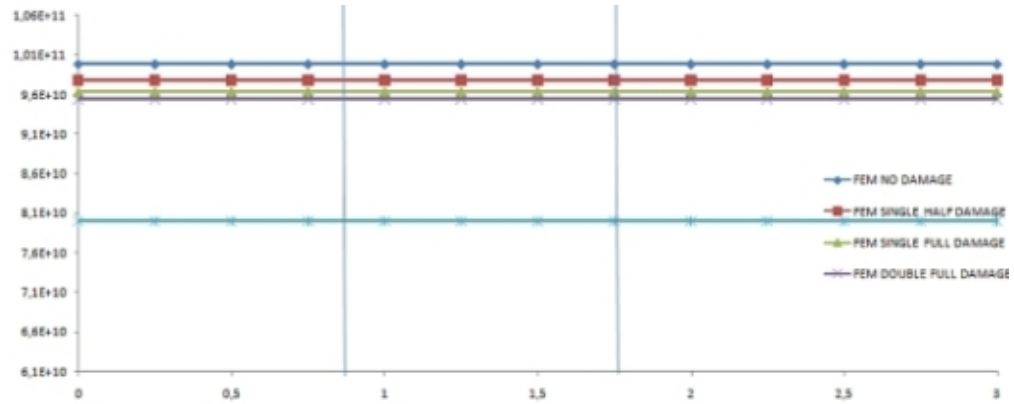

Figure 3.64: EI Coefficients Calculated From FEM Models (1 Segments)

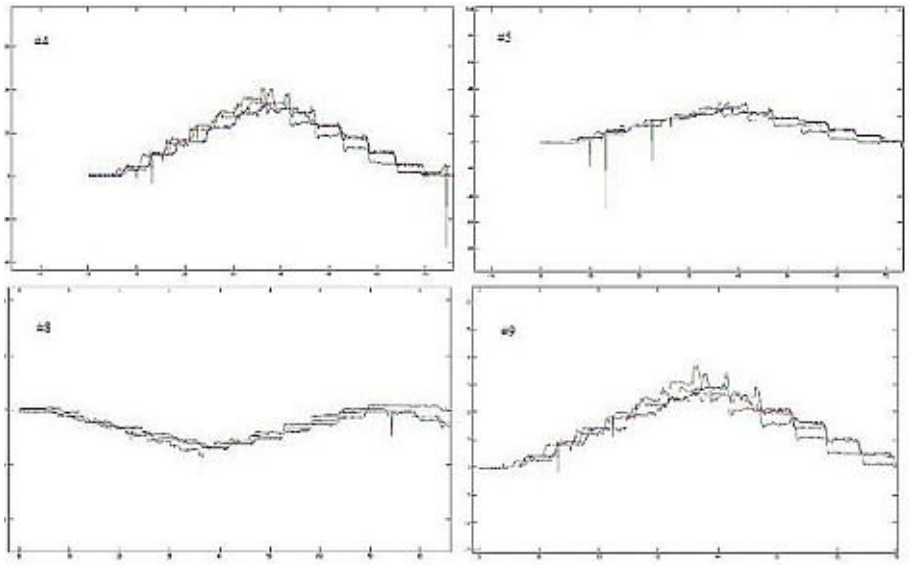

Figure 3.65: Strain Measurements Before Damage Levels 2, 3, 4

3.2.5 Comparing Damage Scenario Test Results

The strain gages, as mentioned in Section 3.2.3.1, are away from the damage locations; therefore the values they read are supposed to stay same in different damage levels. In order to determine whether this statement holds, strain measurements were taken before damage levels two, three, and four under the load of a walking man. Some of the gages malfunctioned during experimenting, but there were several that successfully recorded data on all three experiments. The functioning gages were #4, #5, #8, and #9 and their results can be seen in Figure 3.65. In the graphs, even though a phase shift exists between the data series, the magnitudes are close, indicating that the strains at the measured locations are independent of the damage in a different point. This is as expected, due to the fact that in a stable and statically determinate system, internal forces are independent of the material and sectional properties; i.e. damaging the beam will not change the shape and values of the moment diagram unless any non-linearities occur. As the moment at a point does not change, the only way of stress change is altering the structural properties at that particular section; which is not the case, therefore the strains are constant through damage levels. The reason of the time shift seen in 3.65 is the loading pattern; even though walking on the beam is done in synchronization with a clock, moderately high rate of data acquisition leading to different step times and time lost between steps cause the shifts between three experiments. The walking cycle is done

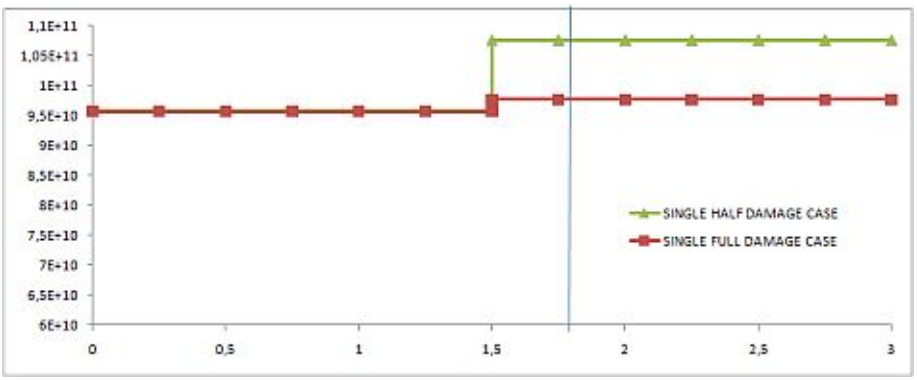

Figure 3.66: 2 Segment Solution of First and Fourth Damage Levels

several times at each stage; however the time shift observed accumulates to a high level in further phases and renders the data almost useless for comparison purposes, therefore only first walking pass is considered.

When the results of the damage levels are compared with each other, the consistency observed in the comparisons with the reference test still exists. If the results of the first and second damage level are compared, the extra damage applied could be seen as a drop in relative segment (Figure 3.66).

CHAPTER 4

CONCLUSIONS AND RECOMMENDATIONS

The conclusions derived from the results obtained in this study and the recommendations based on these conclusions are given in the following sections under separate headings referring to each part of the study.

4.1 Outcomes and Recommendations on Determining Axial Force in Existing Bridge Cables

A custom designed cable tension measurement device was constructed and tested in the laboratory. Tension measurement device was calibrated using a 8.4 m long ø16mm cable between 0.5 kN to 14 kN axial loads. Based on the processed results tabulated in Table 2.1, the instrument can estimate the load with an average error of 4%, if the last two experiment sets are excluded where nonlinear load levels were achieved. Furthermore, the central threaded rod of the measurement device was damaged in the last two sets of experiments (Section 2.3.3.4). Therefore, the last two sets' data was not reliable, having an error of 10%, are excluded from the results. Even if the last two sets of data are included, the overall error margin is obtained as 5.3%. Additional problems with the measurement device which can be improved in the future versions are defined as follows:

1. The curved beam of the instrument was constructed too rigid considering application to larger cable diameters and higher axial load levels. This high rigidity causes little strains on the strain gages. Therefore, even though the output of the sensor were multiplied by 1000, the differences of the read voltages were in the range of 10 to 20 mV. These extremely low values made the system and measurements very susceptible

to ambient noise and environmental effects. In order to overcome this problem, a second device should be manufactured from a section with smaller moment of inertia (i.e. more flexible). By this way, the strains would be naturally higher and external noise and errors induced on the measurement system will be in a smaller range. Furthermore, the weight of the instrument will decrease, leading to ease of use while moving and/or mounting on the cables.b) The threaded tension rod used to apply the transverse direction force on the cable is seen to be too weak and small in diameter. Under higher loads, its threads were easily distorted and caused the device to malfunction, rendering it useless for future experiments. As a remedy, in the second version of the instrument, the central screw rod should be made of high strength steel with a larger diameter so that it will not deform easily.

2. As the tension in the cable gets higher, turning the rod of the device becomes harder, so it may be impossible to use the device on cables having high axial loads (from pedestrian bridges having 60 to 100 kN to highway bridges in the order of 400-500 kN). Therefore another way to pull the cable should be found. A suggestion to this problem is to use hydraulic jacks in the transverse direction.

3. Another improvement is the use of a load cell at the base of central screw. If this is applied, then there will be no need of the strain gages mounted on the beam of the instrument; the force necessary to pull the cable can be read directly, without strain related calibration studies.

4. Using the thread distance of the center screw is not the best way to measure transverse deformation magnitude (Δh); for more precise and automated measurements, a linear variable displacement transducer (LVDT) can be inserted under the arch of the instrument; between the curved girders and the cable.

4.2 Outcomes and Recommendations on Non-Destructive Structural Identification and Damage Detection on Beams

An experimental general method was proposed for determining the bending stiffness changes in an existing beam. The method utilizes measured displacement values obtained under static loads located at several positions on the beam. In order to verify this method, several loading

experiments were conducted on a test specimen and four different finite element models were created for sensitivity analysis. The results obtained from the analytical and experimental studies are itemized below:

1. One of the most important results obtained while comparing the different analytical modes of the lab beam is the difference in analytical results. Although all the material and geometrical properties of models are identical, the dynamic analysis results of the modes were considerably different. This difference is more evident in the case of the line elements; models consisting of area and solid elements better resemble each other in terms of the dynamic properties. Even for such a simple system (a simply supported composite beam), having this much of a difference in the dynamic analysis results emphasizes the importance of the type and pattern of the elements used in the modeling.

2. Comparison of the static deformed shapes of different analytical (nominal) models showed that the displacement is less sensitive to the modeling type. The model constructed using simple frame elements were distinctly different than the other more detailed analytical models. As the system is modeled in simpler ways, the number of approximations increases, leading to greater deviations from the experiment; therefore, oversimplification should be avoided, as well as making the model too complex. A good balance between simplicity and complexity should be found according to the time and resources available.

3. In section 3.2.3, the EI calculation for each segment was performed using pure analytical deformed data of a simple frame model. Extremely small round-off errors in the deformation values obtained from the SAP2000 frame model has caused very large differences in the computed EI values for the 12 and 6 segments approach. In other words, 0,01% (i.e., 1/10000) of a change in the displacement values would cause up to 30 times difference in the obtained EI coefficients (Section 3.2.3). Pure analytical results post-processed using analytical approach causing such large deviations indicates that the experimentally obtained deflection data cannot be used for 6 and 12 segment solution. Therefore, it is necessary to obtain continuous data during testing to improve the large number of segment based solutions; however, due to the nature of the testing process, it was not possible to move load steadily and continuously. For this reason,

only 4 and less number of segments were used for the evaluation of experimentally obtained data.

4. The composite action percentage (i.e. the shear force transfer ratio from the deck to the connected girders) is proven to be linearly related with the overall bending stiffness (i.e., EI value) of the lab beam. This is an important result, due to the fact that it would be possible to determine the shear transfer ratio between the deck and girders directly from the sectional stiffness values calculated by using the proposed method. In addition, any loss in shear transfer (for example loss of composite action) can be identified as a drop in the EI terms.

5. The proposed method is yielding reliable results when displacement data was obtained from a large number of reference points but the EI coefficients were obtained for a smaller number of segments. For example, 12 equally spaced reference points were taken on the beam while the beam was divided into only 4 overall segments to compute the EI values. When 12 segments were used for 12 data locations, the results had noisy variations making it impossible for structural identification, damage localization, and damage quantification. Using smaller number of segments compared to measurement locations can be defined as redundancy in measurements. Due to the inherited properties of the proposed technique, small disturbances in displacement measurements lead to great deviations in EI values, due to the inverse operations performed in the mathematical processing. The best way to overcome these effects is to supply the system with extra data that will be used to obtain best fit results to the measured values.
   The displacement amplitude in the lab experiments were in the order of 2 to 3 millimeters at max. Small errors in the measurement would greatly affect the EI calculations. The displacements for an actual bridge test might give better results when equal number of segments are used for loading location numbers.

6. The variations in displacements before and after a damage scenario can be very low. The composite beam used in this study is extremely rigid, making displacements barely measurable in the tests; deformation is only few millimeters under manageable loads (i.e. load magnitudes that can be handled in an experiment, 600 kg moving load). The maximum displacement obtained when the bottom flanges of both beams were fully cut was in the order of 4 mm, while original beam deflected in the order of 3mm. Small deviations in the measurements due to misalignment of supports, transverse eccentricity

in the moving load's location, additional displacements of the LVDT supports, surface roughness at the contact point of LVDTs, and similar impurities would contaminate the small measurement differences between damage cases.

In low number of segment solutions (one to three segments when 12 references were measured), the method is shown to capture the existence of the damage, gives information about the intensity of it, in addition to clues about the damage location. For example, the reduction in the stiffness coefficient of segments were about the same when the same full-flange-cut damage was induced at either side of the beam. Therefore, if sufficient and accurate data is available, proposed method is a promising technique for system identification, assessment of damage in terms of existence, quantification, and localization.

REFERENCES

[1] Duan Zhongdong, Yan Guirong, Ou Jinping, and B. F. Spencer. Damage localization in ambient vibration by constructing proportional flexibility matrix. *Journal of Sound and Vibration*, 284:455–466, 2004.

[2] L. T. Stutz, D. A. Castello, and F. A. Rochinha. A flexibility-based cantinuum damage identification approach. *Journal of Vibration and Sound*, 279:641–667, 2005.

[3] Ai-Min Yan and Jean-Claude Golinval. Structural damage localization by combining flexibility and stiffness methods. *Engineering Structures*, 27:1752–1761, 2005.

[4] Zhong-Xian Li and Xiao-Ming Yang. Damage identification for beams using ann based on statistical property of structural responses. *Computers & Structures*, 86:64–71, 2008.

[5] Ricardo Perera, Consuelo Huerta, and Juan Manuel Orquin. Identification of damage in rc beams using indexes based on local modal stiffness. *Construction and Building Materials*, 22:1656–1667, 2008.

[6] Abid Ali Shah and Yuri Ribakov. Non-destructive measurements of crack assessment and defect detection in concrete structures. *Materials & Design*, 29:61–69, 2008.

[7] Zhao-Dong Xu and Zhishen Wu. Energy damage detection strategy based on acceleration responses for long span bridge structures. *Engineering Structures*, 29:609–617, 2007.

[8] Ai-Min Yan and Jean-Claude Golinval. Null subspace based damage detection of structures using vibration measurements. *Mechanical Systems and Signal Processing*, 20:611–626, 2006.

[9] P. Capoluongo, C. Ambrosino, S. Compopiano, A Cutolo, M. Giordano, I. Bovio, L. Lecce, and A. Cusano. Modal analysis and damage detection by fiber bragg grating sensors. *Sensors and Actuators A*, 133:415–424, 2007.

[10] V. Pakrashi, B. Basu, and A. O'Connor. Structural damage detection and calibration using wavelet-kurtosis technique. *Engineering Structures*, 29:2097–2108, 2007.

[11] Roman Geier, Guido De Roeck, and Johannes Petz. Cable force determination for the danube channel in vienna. *Structural Engineering International*, 3:181–185, 2001.

[12] Wei-Xin Ren, Hao-Liang Liu, and Gang Chen. Determination of cable tensions based on frequency differences. *International Journal for Computer-Aided Engineering and Software*, 25:172–189, 2008.

[13] Marcelo A. Ceballos and Carlos A. Prato. Determination of the axial force on stay cables accounting for their bending stiffness and rotational end restraints by free vibration tests. *Journal of Sound and Vibration*, 317:127–141, Journal of Sound and Vibration.

[14] A. Cunha, E. Caetano, and R. Delgado. Dynamic tests on large cable-stayed bridge. *Journal of Bridge Engineering*, 6:54–62, 2001.

[15] Çetin Yılmaz and N. Akkas. *Analysis and Design of Steel Structures*. Department of Civil Engineering, METU, 1985.

[16] Building code for steel structures, December 1980.

[17] Requirements for design and construction of reinforced concrete structures, February 2000.

[18] Bathe and Klaus-Jurgen. *Finite Element Procedures*. Prentice Hall, July 1995.

[19] Computers & Structures Inc., Berkeley, California. *CSI Analysis Reference Manual For SAP2000, ETABS and SAFE*, April 2007.

[20] R. J. Allemang. The modal assurance criterion - twenty years of use and abuse. *Journal of Sound and Vibration*, 2:14–21, 2003.

APPENDIX A

EXPERIMENTS ON DETERMINING AXIAL FORCES IN CABLES

A.1 Static Loading Test Results

The x axis is the load applied and y axis is the estimated value.

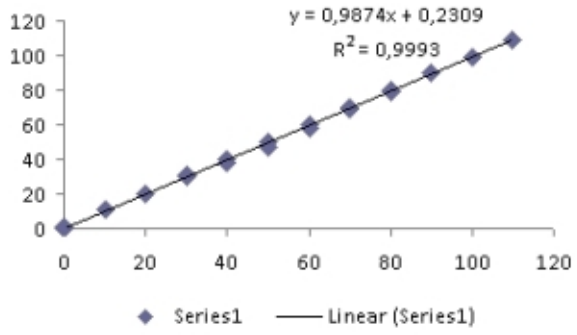

Figure A.1: First cycle result

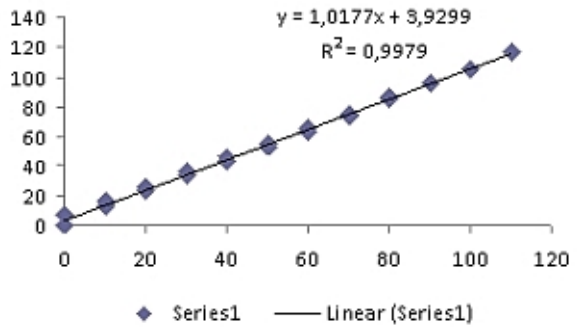

Figure A.2: Second cycle results

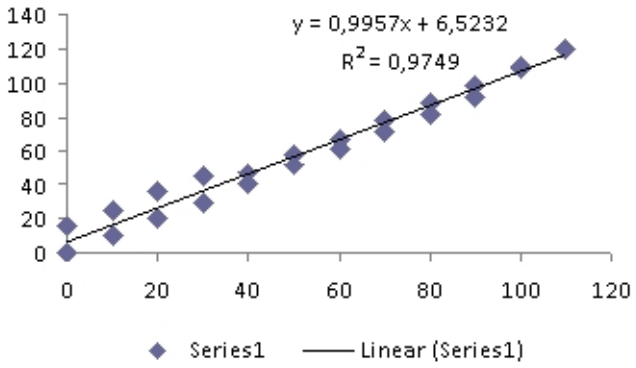

Figure A.3: Third cycle results

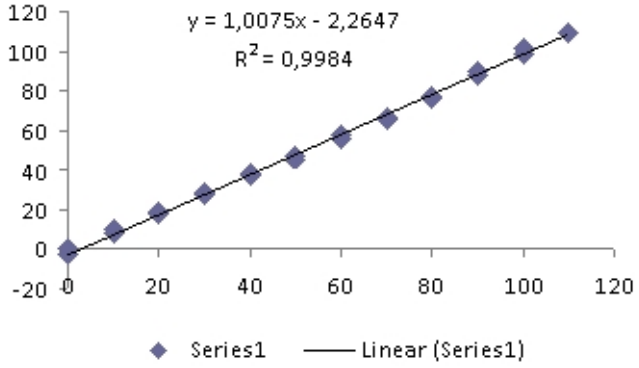

Figure A.4: Fourth cycle results

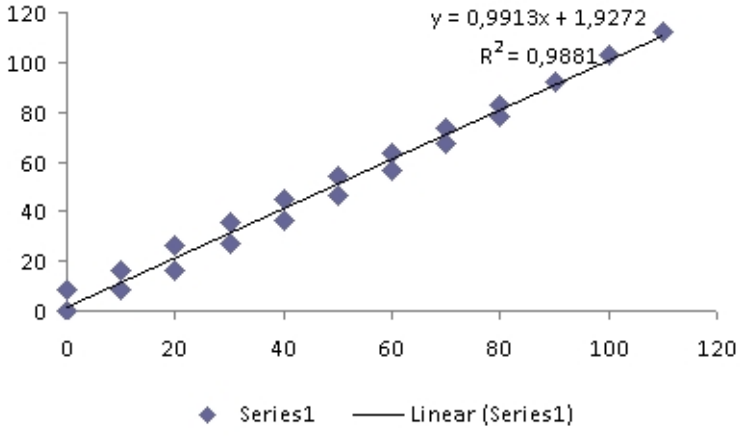

Figure A.5: Fifth cycle results

A.2 Scaled Loading Test Setup

For calibrating the instrument devised, a scaled load test is performed and details of the test setup is given in the figures below.

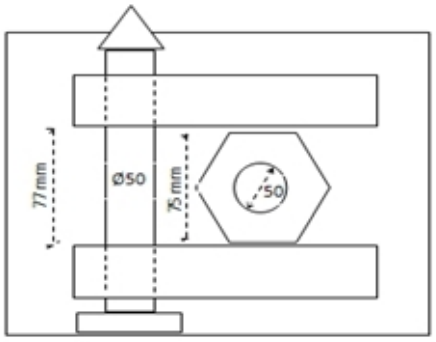

Figure A.6: Top vew of bottom connection with dimensions

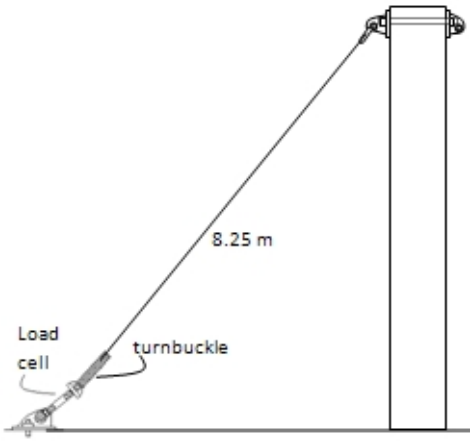

Figure A.7: General overview of test setup

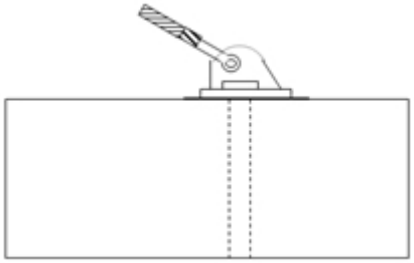

Figure A.8: Bottom connection side view

APPENDIX B

FACTORS AFFECTING SECTION EI AND STATIC LOAD TEST PHOTOS

B.1 Effects of Segment Length, Damage Intensity and Location (within a segment) to Segment EI

In order to determine how selected segment length and presence of point damage within a segment affects the EI coefficient of that segment, several analytical studies are performed. In the calculations, the segments of shell FE model (Section 3.2.2.4) having different lengths from 0.25 meters to 1.5 meters are considered. The beam segment is modeled as having a fixed connection at one side (cantilever) and a pure moment is applied to the segment. The EI value is calculated from the rotation-moment relation and the rotation is calculated from the analysis results of the FE model. Three different damage levels are considered within a segment; half tension flange damage, full tension flange damage, and 3/4 web damage in addition to full tension flange damage. Two different locations are utilized for damage (within the segment) for identifying the effect of damage location on the calculated EI.

From the results, it is concluded that the damage location has little effect on the calculated EI, therefore the variance of EI due to the location of damage relative to the selected segment can be neglected. Increasing the segment length for one damage state decreases the level of EI drop observed, as expected since increasing the segment length causes averaging the EI value of the section over a greater length (Figure B.1). In the Figure B.1, the vertical axis is the drop in calculated EI for a damage level, the horizontal axis is the segment length in meters, and the tendency of decrease in EI change percentage when the segment length is increased could be identified from the three series. Increasing the damage intensity also increases the EI change observed, as anticipated. The three series in Figure B.1 are three different damage

scenarios and they show a trend of increase in calculated EI change percentages as damage level is increased.

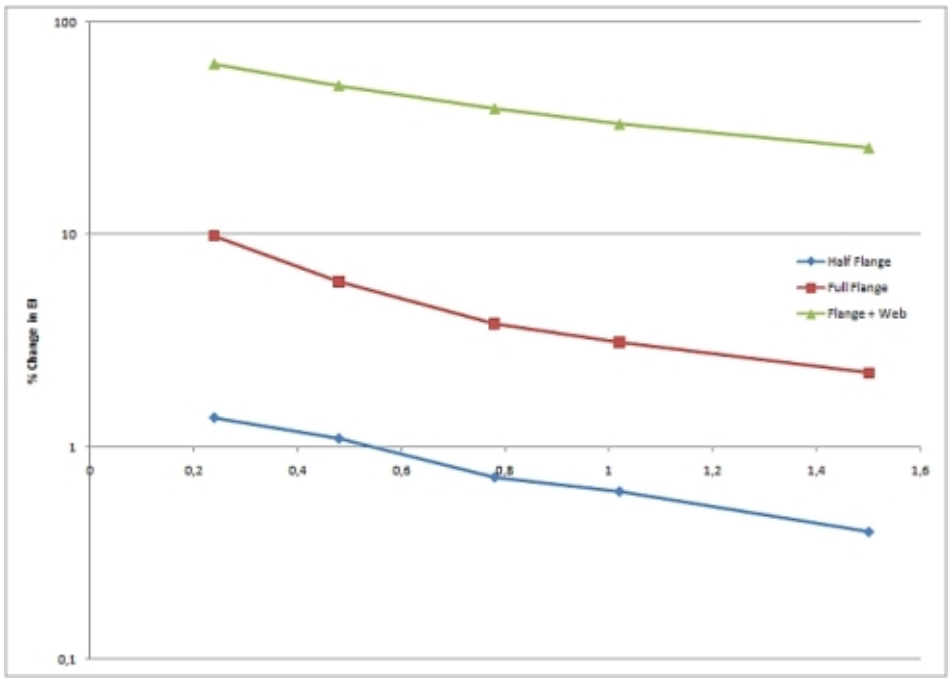

Figure B.1: Effects of Segment Length and Damage Level on Calculated EI

B.2 Static Load Test Photos

In this part, photographs taken during various stages of the experiments conducted on the test beam are displayed.

Figure B.2: Overall View of Experiment

Figure B.3: Double Flange Cut (Damage Level 2)

Figure B.4: Conducting Second Damage Level Experiment

Figure B.5: Conducting Third Damage Level Experiment

Figure B.6: Fourth Damage Level

Figure B.7: Conducting Fourth Damage Level Experiment